RADIATIVE COUPLING BETWEEN QUANTUM DOTS IN PHOTONIC CRYSTAL MOLECULES

JUAN PABLO VASCO CANO

SUPERVISOR
Prof. Dr. Paulo Sergio Soares Guimarães
CO-SUPERVISOR
Prof. Dr. Dario Gerace

Thesis presented to
UNIVERSIDADE FEDERAL DE MINAS GERAIS
as partial requirement for the title of
PHD IN PHYSICS
Instituto de Ciências Exatas
Departamento de Física

Belo Horizonte, Brasil
June 2016

Juan Pablo Vasco Cano: *Radiative coupling between quantum dots in photonic crystal molecules,*

SUPERVISOR:
Prof. Dr. Paulo Sergio Soares Guimarães
Departamento de Física
Instituto de Ciências Exatas
Universidade Federal de Minas Gerais
Belo Horizonte, Brasil

CO-SUPERVISOR:
Prof. Dr. Dario Gerace
Dipartimento di Fisica
Università degli Studi di Pavia
Pavia, Italia

LOCATION:
Belo Horizonte, Brasil

To Fernanda

ABSTRACT

In the present work, we theoretically address the possibility of using strongly coupled photonic crystal molecules to efficiently increase the mutual coupling rate between two quantum dots at large inter-dot distances. The photonic molecules we are interested in are composed of two coupled photonic crystal slab cavities, or photonic crystal dimers. We specifically consider coupled L3 cavities, *i.e.*, three missing holes in a hexagonal lattice. We treat the light-matter coupling with a semiclassical formalism based on Green's tensors and the classical electromagnetic fields are solved within a guided-mode expansion approach. We find that when the quantum dots are in resonance with either of the two lowest energy modes (bonding/anti-bonding) of the photonic dimer, and in the strong cavity-cavity coupling regime, the inter-dot radiative coupling strength is proportional to the quality factors of the dimer modes and it can be of the order of 1 meV, which is at least an order of magnitude larger than typical values achieved in one-dimensional systems. We also address the effects of structural disorder in the photonic crystal lattice on the mutual coupling between the two quantum dots, by assuming disorder parameters that are consistent with the current state-of-art fabrication technology. We find that the effective radiative coupling between the dots is robust against non-perfect quantum dot positioning and, to a smaller extent, to structural disorder in the photonic crystal. Using a fully quantum mechanical model, based on the master equation, we quantify the entanglement between the quantum dots by the Peres-Horodecki negativity criterion. We show that it is possible to achieve negativity values of the order of 0.1 (20% of the maximum value) in the steady sate regime, for interdot distances which are larger than the characteristic wavelength of the system. We also find that this amount of entanglement remains of the same order of magnitude, as long as the distance between the dots is such that the normal mode splitting of the photonic dimer is much greater than the normal mode linewidth. Considering detuned quantum dots, we find that the entanglement is preserved as long as the dot-dot detuning is smaller than the exciton linewidth. Finally, we determine that the most appropriate configuration for long-range entanglement applications is the one for which the line connecting the centers of the L3 cavities is at an angle of 30 degrees with the horizontal axis. Based on this configuration, we propose a simple device for practical applications in the transient dynamics where the amount of entanglement can be of the order of 40% for state-of-art InGaAs quantum dots.

PUBLICATIONS RELATED TO THIS THESIS

1. J.P. Vasco, P.S.S. Guimarães, and D. Gerace, "Long-distance radiative coupling between quantum dots in photonic crystal dimers", *Physical Review B* **90**, 155436 (2014).

2. J.P. Vasco, D. Gerace, and P.S.S. Guimarães, "Effect of disorder on the radiative coupling between distant quantum dots embedded in a photonic crystal dimer", *Superlattices and Microstructures* **89**, 282 (2016).

3. J.P. Vasco, D. Gerace, P.S.S. Guimarães, and M.F. Santos, "Steady state entanglement between distant quantum dots in photonic crystal dimers", *Submitted to Physical Review B*.

ACKNOWLEDGMENTS

I would like to gratefully acknowledge my Doctoral supervisor and friend Prof. Paulo Sergio Soares Guimarães for his unconditional support during the development of this work. It was several years of invaluable scientific discussions, with Colombian coffee and Swiss chocolates, where he always encouraged my ideas and asked me the correct questions to answer. His teachings were and will be fundamentals in my professional career.

I would like to thank Dario Gerace, who became a friend in the last years, by his generous support in the theoretical and very technical aspects of my Doctoral research. His scientific work served as inspiration for many topics of the present thesis.

Special thanks to my dear friend Prof. Herbert Vinck Posada who is supporting me since my first scientific works on photonic crystals and gave me several insights in the first stage of my Doctoral work. Also, I would like to acknowledge the invaluable support of Prof. Marcelo França Santos in the quantum mechanical aspects of the present work.

Thanks to my friend Dr. Carlos Parra for useful discussions during the quantum mechanical calculations which were carried out in the last part of this thesis.

I would like to thank the team of the Laboratory of Semiconductors (UFMG) for their friendship and very nice working atmosphere.

Finally, I would like to acknowledge the financial support for this work, from CAPES, CNPq, FAPEMIG and INCT-DISSE.

CONTENTS

1 INTRODUCTION

In 1987, Eli Yablonovitch proposed in a revolutionary work the possibility of inhibiting the spontaneous emission using a three dimensional periodic dielectric semiconductor structure, by overlapping the electromagnetic band gap with the electron-hole recombination energy of the semiconductor [1]. In the same year, Sajeev John introduced the idea of strong Anderson localization of photons in disordered dielectric systems, by fluctuating a periodic dielectric function in a superlattice with a random dielectric contribution [2]. Due to these important works, nowadays 1987 is known as the birthday of photonic crystals, namely, periodic spatially-modulated dielectrics, with potential capabilities of controlling the flow of light. Photonic crystals, schematically represented in Fig. 1, can be periodic in one, two or three dimensions, allowing the engineering of the electromagnetic density of states throughout the dielectric structure [3]. In particular, two-dimensional photonic crystals embedded in planar semiconductor dielectric waveguides, i.e., two-dimensional photonic crystal slabs, have emerged as the best candidates for on-chip implementations due to the high-nanometric precision of lithography and etching processes achieved nowadays [4, 5]. On the other hand, semiconductor quantum dots have attracted considerable attention in the last two decades, because they are promising candidates to realize solid state quantum bits (qubits) to be employed in quantum information and communication technologies [6, 7]; their characteristic discrete spectra, long coherence times, and large oscillator strengths make them almost ideal *artificial atoms* that can be fixed in position and integrated into semiconductor structures [8, 9]. Interfacing photonic crystals with semiconductor quantum dots have allowed to study a vast variety of cavity quantum electrodynamics phenomena [10, 11, 12], quantum information technologies [13] and quantum photonic applications [14, 15]. Specifically, fully quantum mechanical effects as strong light-matter coupling [16, 17] and control of spontaneous emission [18, 19] have been successfully demonstrated in photonic crystal cavities due to their capabilities of confining the light with modal volumes next to the diffraction limit and very high quality factors [20].

The realization of two coherently interacting quantum dots and the possibility to externally control such interaction are crucial requirements to perform two-qubit operations, which are the building blocks of a quantum information protocol [22]. Nevertheless, the interaction strength between two quantum dots decays rapidly as a function

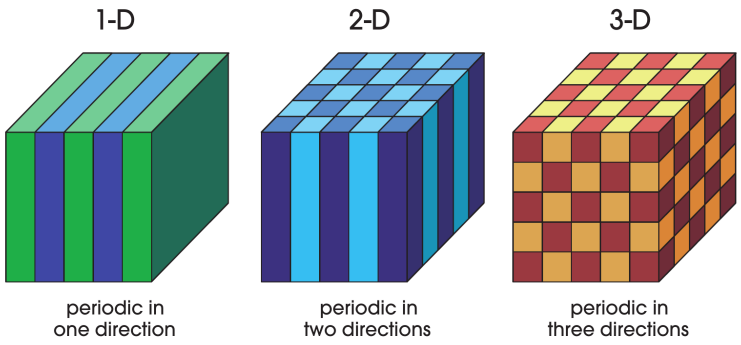

Figure 1: Schematic illustration of one, two and three dimensional periodicity in photonic crystals. Figure taken from Ref. [21].

of the inter-dot distance [23], which makes entanglement challenging when their distances are larger than their characteristic emission wavelength. Thus, there is a growing theoretical and experimental interest to mediate the dot-dot coupling via electromagnetic modes in a semiconductor photonic crystal structure [24, 25, 26], enabling controlled gate operations with such interacting qubits through a *photonic quantum bus*, namely, a photonic degree of freedom which interacts with the localized qubits. Due to the exceptional capabilities to efficiently guide and confine the electromagnetic radiation, and the high degree of precision in fabrication techniques currently achieved, photonic crystal slab structures should allow to overcome the short-range Förster coupling between interacting quantum dots, thus achieving sizable effective radiative coupling at distances quite larger than their emission wavelength. Proposals for increasing the mutual interaction distance between two quantum dots in a photonic crystal platform mainly considered using a waveguide as a bus for photon propagation [26, 27, 28]. The role of structural disorder on light localization was also addressed [29]. Alternatively, preliminary studies considered the mutual coupling between two quantum dots positioned at the field antinodes within the same photonic crystal cavity [26, 30], for which early experimental evidence was shown [24, 31]. The possibility of mediating the inter-dot coupling through the normal modes of a photonic molecule has been considered for coupled micro disks [32], where the distance is limited by evanescent inter-cavity coupling in free space.

In the present thesis we theoretically address the possibility of using strongly coupled photonic crystal molecules, i.e., two or more strongly coupled photonic crystal cavities, to efficiently increase the mutual quantum dot coupling rate even at large distances, which was overlooked in the literature up to our first publication, Ref. [33]. The key parameters leading to a sizable radiative coupling between quantum dots in resonance with a given photonic mode are either

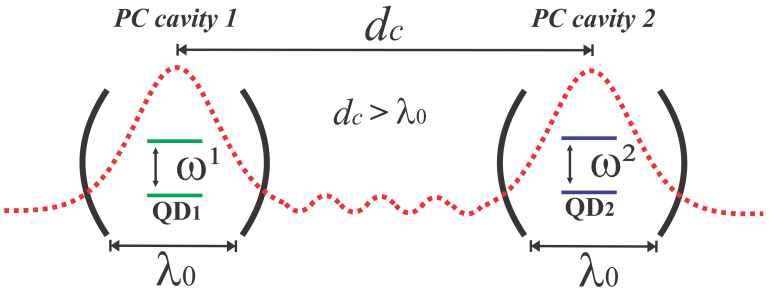

Figure 2: Schematic representation of the system investigated in this work: two strongly coupled photonic crystal (PC) nanocavities, each containing a single quantum dot (QD). The distance between the nanocavities, d_c, can be larger than the characteristic exciton emission wavelength in vacuum, λ_0.

the coupling strengths between each dot and the field, or the total (intrinsic and extrinsic) photonic mode and exciton loss rates. The former quantity increases as the modal volume decreases, for two quantum dots that are spatially positioned at an electric field antinode of the corresponding photonic mode, and the latter should be small as compared to the exciton-field coupling strengths. Photonic crystal molecules naturally fulfill these required conditions. In fact, the normal modes associated to photonic crystal molecules are strongly localized in the photonic cavities, allowing modal volumes next to the diffraction limit, and quality factors can be even larger (i.e., smaller losses) than the quality factors of the decoupled cavities [34]. In addition, it has been recently shown that it is possible to have strongly coupled photonic crystal cavities at inter-cavity distances which are quite larger than the characteristic wavelength of the system in a photonic crystal molecule [35]. A schematic representation of our system is shown in Fig. 2. The photonic molecules we are interested in are composed of two coupled nominally identical photonic crystal slab cavities, i.e., photonic crystal dimers.

This thesis is organized as follows. In Chapter 2, the fundamental theory of photonic crystals and the key aspects of the guided mode expansion method are presented. We also discuss the basic theory of quantum dots within a simple harmonic oscillator model as well as the $1/R^3$ dependence of Förster interaction between two coupled quantum dots spatially separated by R. The semiclassical and quantum formalisms adopted for studying the two-dot photonic-molecule system are also discussed in detail. In Chapter 3, the main results on the long-distance radiative coupling between the quantum dots coupled through the normal modes of a photonic crystal dimer, disorder effects and long-range entanglement between the dots are present. Finally, the conclusions and future developments are given in Chapter 4.

2

FUNDAMENTAL THEORY

This chapter is addressed to review the basic theory of photonic crystals and quantum dots, as well as the classical, semiclassical and fully quantum mechanical methods adopted for solving the system which is the subject of study of the present thesis.

2.1 THEORY OF PHOTONIC CRYSTALS

The electronic transport in atomic or molecular crystals is determined by the geometry of the underlying Bravais lattice and the physical properties of the atomic basis. As it is well known from solid state physics, electrons suffer coherent scattering when the period of the lattice and the size of the atomic basis, determined by the atomic potential, is of the order of their de Broglie wavelength. These scattered waves can interfere, giving rise to allowed (constructive interference) and forbidden (destructive interference) states. The former are known as electronic bands and the latter as electronic band gaps. Similarly, electromagnetic waves suffer coherent scattering in periodic dielectric media when the period of the lattice and the dielectric dimensions are of the order of the electromagnetic wavelength. Here, constructive and destructive interference of the scattered waves determine the photonic bands and photonic band gaps of the system, respectively. Such structures, whose dielectric function is periodically modulated, are known as *photonic crystals*, and they are a subject of study of electromagnetic theory, applying methods and concepts usually employed in quantum mechanics.

2.1.1 *Maxwell's equations in periodic dielectric media*

The starting point of every study on photonic crystals is determined by the formulation of the problem in terms of the fundamental equations of the electromagnetic theory, i.e., Maxwell's equations. Since we are mainly interested in the spectrum of the system instead of its physical response, we assume that free charges and electric currents are absent. Under these assumptions, Maxwell's equations take the following form in Gaussian units:

$$\begin{aligned} \nabla \cdot \mathbf{D}(\mathbf{r}, t) &= 0, & \nabla \times \mathbf{E}(\mathbf{r}, t) &= -\frac{1}{c}\frac{\partial}{\partial t}\mathbf{B}(\mathbf{r}, t), \\ \nabla \cdot \mathbf{B}(\mathbf{r}, t) &= 0, & \nabla \times \mathbf{H}(\mathbf{r}, t) &= \frac{1}{c}\frac{\partial}{\partial t}\mathbf{D}(\mathbf{r}, t), \end{aligned} \tag{1}$$

where **E**, **H**, **D** and **B** are the electric, magnetic, electric displacement and magnetic induction fields, respectively, and c is the speed of light in vacuum. The electromagnetic fields **H** and **B**, as well as **E** and **D** are related by the constitutive relations [36]:

$$\mathbf{B}(\mathbf{r},t) = \hat{\mu}(\mathbf{r})\mathbf{H}(\mathbf{r},t), \qquad \mathbf{D}(\mathbf{r},t) = \hat{\epsilon}(\mathbf{r})\mathbf{E}(\mathbf{r},t), \tag{2}$$

where $\hat{\mu}(\mathbf{r})$ and $\hat{\epsilon}(\mathbf{r})$ are the magnetic and dielectric tensors. In most cases, photonic crystals are fabricated using isotropic and non-magnetic materials, which allow us to safely set $\hat{\mu}(\mathbf{r}) = \mu(\mathbf{r}) = 1$ and $\epsilon(\mathbf{r}) = \hat{\epsilon}(\mathbf{r})$. Furthermore, since **H** and **E** are complicated functions of space and time, we take advantage of the linearity of Maxwell's equations by expanding the fields in a set of harmonic modes. The harmonic solutions are written as:

$$\mathbf{H}(\mathbf{r},t) = \mathbf{H}(\mathbf{r})e^{-i\omega t}, \qquad \mathbf{E}(\mathbf{r},t) = \mathbf{E}(\mathbf{r})e^{-i\omega t}, \tag{3}$$

which automatically separates the time and space dependence. Using the expressions of Eqs. (2) and (3), and decoupling the electric and magnetic fields from Eq. (1), we obtain the wave equations for electric and magnetic fields,

$$\hat{\Theta}\mathbf{H}(\mathbf{r}) = \nabla \times \frac{1}{\epsilon(\mathbf{r})}\nabla \times \mathbf{H}(\mathbf{r}) = \frac{\omega^2}{c^2}\mathbf{H}(\mathbf{r}), \tag{4}$$

$$\hat{\mathcal{L}}_{\mathbf{E}}\mathbf{E}(\mathbf{r}) = \frac{1}{\epsilon(\mathbf{r})}\nabla \times \nabla \times \mathbf{E}(\mathbf{r}) = \frac{\omega^2}{c^2}\mathbf{E}(\mathbf{r}). \tag{5}$$

subject, respectively, to the transversality conditions:

$$\nabla \cdot \mathbf{H}(\mathbf{r}) = 0, \qquad \nabla \cdot [\epsilon(\mathbf{r})\mathbf{E}(\mathbf{r})] = 0, \tag{6}$$

In the literature of photonic crystals $\hat{\Theta}$ is known as the Maxwell operator. The wave equations in Eqs. (4) and (5) determine eigenvalue problems which resemble the stationary Schrödinger equation; in fact, the function $\epsilon(\mathbf{r})$ can be understood as the dielectric potential. The linear operator $\hat{\Theta}$ in Eq. (4) is Hermitian, hence, the following expressions are guaranteed [37]:

$$\frac{\omega^2}{c^2} = \left(\frac{\omega^2}{c^2}\right)^*, \qquad \int \mathbf{H}_i^*(\mathbf{r}) \cdot \mathbf{H}_j(\mathbf{r}) d^3\mathbf{r} = N^2\delta_{ij}, \tag{7}$$

with N a normalization factor. In addition to this, for $\epsilon(\mathbf{r}) > 0$, $\hat{\Theta}$ is positive semidefinite, i.e., $\frac{\omega^2}{c^2} \geqslant 0$, constraining the frequencies ω to be real in lossless media [21]. On the other hand, the linear operator $\hat{\mathcal{L}}_{\mathbf{E}}$ is not Hermitian, and orthogonality relations as in Eq. (7), are not guaranteed [3]. Furthermore, from Eq. (6), the electric field is not transversal, and the zero-divergence equation depends on the specific dielectric function. These mathematical issues turn the solution of Maxwell's equations quite complicated from the electric point of view.

Notice, however, that the magnetic field is fully transversal, and such a condition, as well as the hermiticity of $\hat{\Theta}$, do not depend on the specific dielectric system in lossless media. Therefore, the solution of the electromagnetic problem is less difficult when we start from the magnetic wave equation, and the corresponding electric field solution can be obtained via the curl equation:

$$\mathbf{E}(\mathbf{r}) = i\frac{c}{\omega\epsilon(\mathbf{r})}\nabla \times \mathbf{H}(\mathbf{r}). \tag{8}$$

In this way, we will adopt the solution of Eq. (4) instead of Eq. (5) for computing the eigenmodes of photonic crystals from now on. Any particular condition on the spatial dependence of $\epsilon(\mathbf{r})$ has heretofore not been specified, in fact, Eq. (4) does not necessarily describe a photonic structure. Photonic crystals are represented by a periodic dielectric function:

$$\epsilon(\mathbf{r}) = \epsilon(\mathbf{r} + \mathbf{R}), \tag{9}$$

where $\mathbf{R}$ is the translation vector of the Bravais lattice. Atomic and molecular crystals are the result of a Bravais lattice plus an atomic basis; analogously, photonic crystals are the result of a Bravais lattice plus a *dielectric basis*. Since there are no fundamental differences between the mathematical concepts describing atomic and photonic crystals, and the physics of both systems is totally equivalent, the theoretical framework of solid state physics can be applied to electromagnetic crystals. The magnetic field solutions of Eq. (4) considering Eq. (9) are written, accordingly, in the Bloch-Floquet form:

$$\mathbf{H}_{\mathbf{k}}(\mathbf{r}) = e^{i\mathbf{k}\cdot\mathbf{r}}\mathbf{u}_{\mathbf{k}}(\mathbf{r}), \qquad \mathbf{u}_{\mathbf{k}}(\mathbf{r}) = \mathbf{u}_{\mathbf{k}}(\mathbf{r} + \mathbf{R}). \tag{10}$$

The differential equation for the periodic function of Bloch states, $\mathbf{u}_{\mathbf{k}}(\mathbf{r})$, is found by substituting the first expression of Eq. (10) in the wave equation of Eq. (4). It can be easily shown that:

$$(i\mathbf{k} + \nabla) \times \left[\frac{1}{\epsilon(\mathbf{r})}(i\mathbf{k} + \nabla) \times \mathbf{u}_{\mathbf{k}}(\mathbf{r})\right] = \frac{\omega_{\mathbf{k}}^2}{c^2}\mathbf{u}_{\mathbf{k}}(\mathbf{r}). \tag{11}$$

Due to the periodic boundary condition of $\mathbf{u}_{\mathbf{k}}(\mathbf{r})$, the Hermitian problem in Eq. (11) is restricted to a single primitive cell of the lattice, i.e., finite volume, consequently, we expect the solutions to be discretely spaced with band index n. Moreover, the Maxwell operator depends on $\mathbf{k}$, which can vary continuously over the reciprocal space, and the frequency spectrum, $\omega_{\mathbf{k}} = \omega_n(\mathbf{k})$, defines the photonic band structure of the system. The function $\omega_{\mathbf{k}} = \omega_n(\mathbf{k})$ is represented in the irreducible Brillouin zone, which is determined by the symmetry properties of both, the dielectric basis and the reciprocal Bravais lattice [38]. If there is no real solutions for $\omega_{\mathbf{k}} = \omega_n(\mathbf{k})$, irrespective the value of $\mathbf{k}$, we say that the system has a photonic band gap.

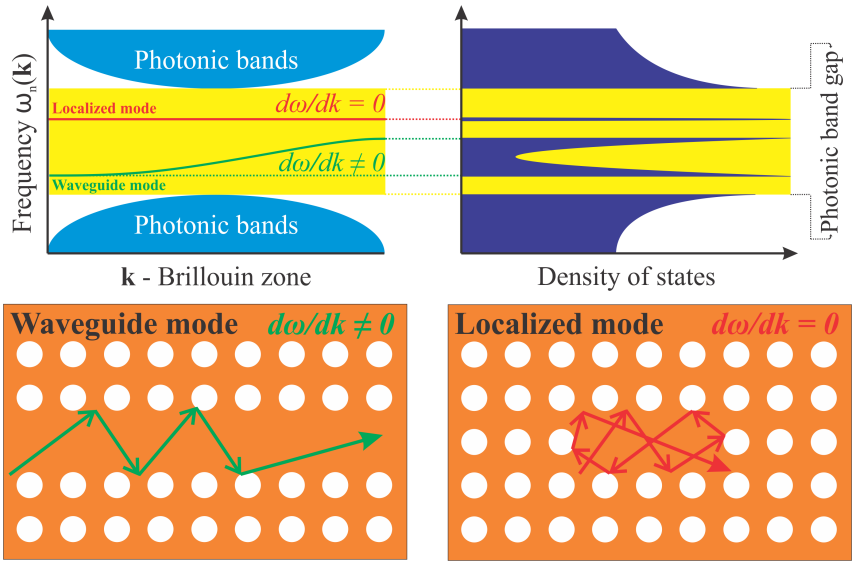

Figure 3: Typical dispersion relations of cavity modes, red band, and waveguide modes, green band. the corresponding density of states is sketched at right. At bottom, waveguide and localized modes are represented in a two dimensional photonic crystal, where orange and white correspond to different refractive indices.

Photonic crystals become very interesting where "impurities", known as defects, are introduced in the dielectric lattice. In the same manner as for solid state crystals, where localized states appear due to the impurities, the electromagnetic field can be localized around dielectric defects, creating allowed states inside the photonic band gap. Defects on photonic crystals can be produced either modifying the geometry or changing the dielectric properties at specific regions of the lattice; in particular, point and linear defects represent the fundamental blocks for the vast majority of systems currently studied. The former is commonly called cavity and the latter waveguide.

Figure 3 shows a schematic representation of the typical bands, in red and green colors, associated to cavity and waveguide modes, respectively; the yellow region corresponds to the photonic gap of the system and lighter-blue regions represent the photonic bands. The group velocity $d\omega/dk$ of cavity modes is zero in all points of the Brillouin zone, while for waveguide modes is in general different from zero. The corresponding photonic density of states is sketched at right in darker-blue; localized modes have the largest density of states, as well as the band edges of waveguide modes and photonic bands edges, where the group velocity is near to zero[1]. At bottom of Fig. 3, waveguide and localized modes are represented in a two dimensional photonic crystal, where orange and white correspond to

1 The band edge regions are specially interesting for slow light phenomena [39].

different refractive indices. Here, the waveguide is created by removing a complete row of circles, and the cavity by removing only three of them. Due to the low losses of dielectrics at optical frequencies and the efficient photonic band gap confinement mechanism[2], waveguide and cavity modes in photonic crystals usually have very high quality factors[3], and the light confinement is next to the diffraction limit. The latter allows to obtain very small modal volumes in photonic crystal cavities[4]. The elevated density of states at cavity resonances, together with their high quality factors and diffraction limited modal volumes, open the possibility of cavity quantum electrodynamics phenomena, as Purcell enhancement [40] and strong coupling, when light emitters are positioned within the photonic crystal nanocavities to interact with the electromagnetic fields [12, 19].

2.1.2 *Photonic crystal molecules*

Two or more coupled photonic crystal cavities form a photonic crystal molecule. In Fig. 4 we schematically represent the weak and strong coupling regime of a photonic crystal molecule formed by two identical cavities, which is known as a photonic crystal dimer. When the distance between the two cavities is much larger than their mode wavelengths, i.e., $d_c >> \lambda_c$, the spectrum of the system is degenerated with the same single cavity frequencies. Over these conditions the system is in the weak coupling regime, and it does not strictly represent a photonic molecule. For intercavity distances smaller than, or of the same order of λ_c, the system is in the strong coupling regime with non-degenerated frequency spectrum determined by the splitted states of the single cavities. In the case of photonic dimers (identical cavities), where the system has a symmetry point, the normal mode frequencies are separated in bonding (subscript $+$) and antibonding (subscript $-$) states, resembling atomic molecules. The bonding and antibonding behavior are determined by the symmetry of the electromagnetic modes; the former is symmetric while the latter is antisymmetric with respect to the symmetry point, as it is shown schematically in Fig. 4, where the symmetry point is at the center of the photonic lattice. The photonic normal mode frequencies of the molecule can be written as the single cavity frequency plus a coupling term δ, which depends on the amount of overlapping and interference conditions between the single cavity modes. In general, the strength of

2 The photonic band gap confinement mechanism for light, based on interference phenomena, is known as distributed Bragg reflection (DBR mechanism).

3 The quality factor of a photonic mode measures the photon lifetime within the cavity and it is defined as the ratio between the resonant frequency and the linewidth: $Q = \frac{\omega}{\delta\omega}$.

4 The modal volume of a dielectric cavity measures the effective space occupied by the photonic mode, and it is defined as: $V = \frac{\int \epsilon(\mathbf{r})|\mathbf{E}(\mathbf{r})|^2 \, d\mathbf{r}}{\epsilon(\mathbf{r}_0)|\mathbf{E}(\mathbf{r}_0)|^2}$, where $\mathbf{r}_0$ is the position of the electric field peak. In photonic crystals $V \sim (\lambda/n)^3$, with n the refractive index.

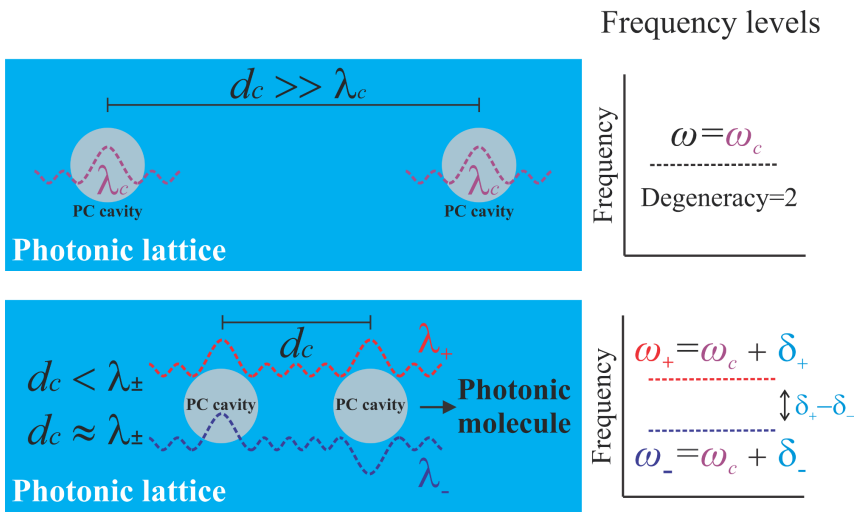

Figure 4: Schematic representation of a photonic crystal molecule formed by two identical cavities, i.e., a photonic crystal dimer, in the weak (above) and strong (below) coupling regimes. The frequency levels for both cases are sketched, correspondingly, at right.

the coupling term δ, which can be positive or negative, is different for bonding and antibonding modes, i.e. $|\delta_+| \neq |\delta_-|$, furthermore, distinct from the atomic case, antibonding ground sates and increasing splitting with increasing d_c are possible in photonic crystal molecules [41].

The delocalized nature of normal modes in photonic crystal molecules will be useful to radiatively couple two semiconductor quantum light emitters in Sec. 3.2, separated by a distance that can be larger than the characteristic wavelength of the system.

2.1.3 *Two-dimensional photonic crystal slabs*

Three-dimensional complete photonic band gap is the ultimate objective of the light confinement paradigm. Theoretical studies on fully three dimensional photonic crystals have been addressed in the literature for solving the photonic band gap problem with satisfactory and promising results [1, 2, 42, 43]. Nevertheless, large-area and defect-free implementations are quite challenging even for state-of-art fabrication techniques [44, 45, 46]. Two-dimensional photonic crystals embedded into planar dielectric waveguides, known as two-dimensional photonic crystal slabs, have emerged in the last decade as the best candidates for efficiently confining and guiding the electromagnetic fields at optical frequencies in three dimensions. Currently, lithography and etching processes at sub-micron scales are in a very mature and advanced stage, allowing the fabrication of large-area photonic

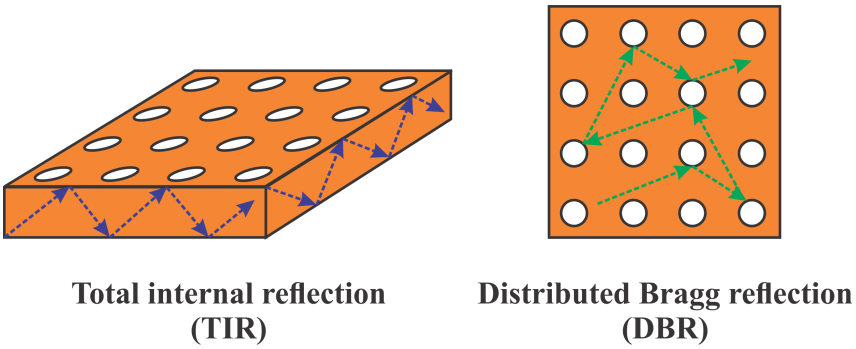

Figure 5: Representation of the total internal reflection and the distributed Bragg reflection mechanisms in two-dimensional photonic crystal slabs.

crystal slabs with high-nanometric precision [4, 5]. Although experimental and theoretical complete photonic band gap has not been achieved in these structures up to now, three-dimensional confinement is possible for specific mode polarizations as it will be discussed below.

Figure 5 shows a typical photonic crystal slab where the two dimensional periodic pattern is defined by a square lattice of circular holes in a dielectric planar waveguide. Vertical confinement of light is controlled by total internal reflection (TIR) [5], and in-plane propagation is controlled by the photonic pattern via distributed Bragg reflection (DBR); photonic band gaps in these systems are thus conditioned by both TIR and DBR mechanisms. The electromagnetic modes of fully two-dimensional photonic crystals, which are periodic in a certain plane and uniform along the axis perpendicular to that plane, are separated in two orthogonal polarizations, namely, transverse-electric (TE) and transverse-magnetic (TM); considering xy as the plane where the photonic pattern is present, the former has the non-vanishing field components (E_x, Ey, Hz) and the latter has the non-vanishing field components (H_x, Hy, Ez). The separation of modes in two different solutions is due to the existence of a symmetry plane parallel to the periodic pattern at any position of the perpendicular axis. Figure 6 schematically shows the two mode polarizations with different symmetry properties for two-dimensional crystals (top). The system is uniform along the z direction, i.e. thickness $d \to \infty$, and any plane perpendicular to the z axis corresponds to a symmetry plane of the system; they are shown three of them in the figure (top), $z = \pm\delta$ and $z = 0$, where delta is any real number. The electric and magnetic fields are confined at these planes for TE and TM modes, respectively. In comparison with quantum mechanics, where the presence of symmetry plane on the quantum potential separates the wavefunction

5 Also know as index guiding for photonic crystal slabs [21].

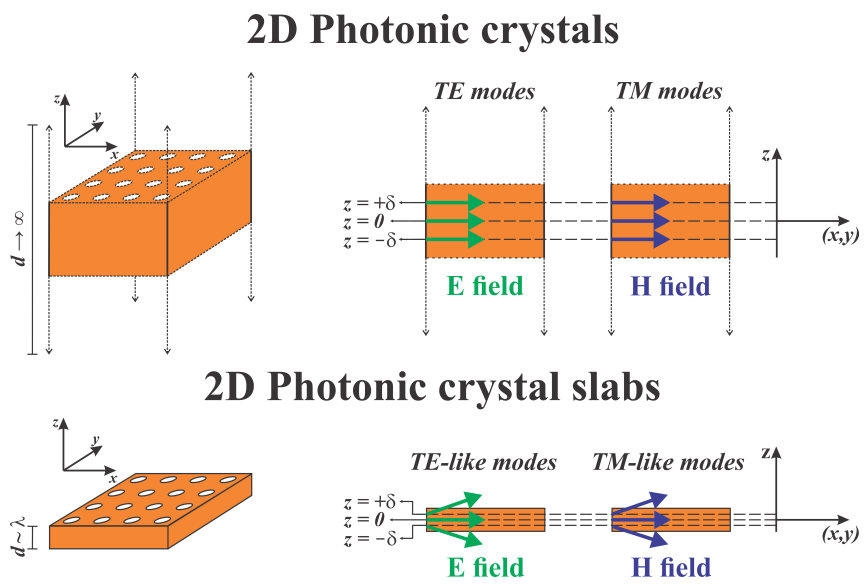

Figure 6: Schematic representation of the electromagnetic modes for fully two-dimensional photonic crystals (top), and two-dimensional photonic crystal slabs (bottom). The former has an infinite set of symmetry planes along the z axis, and the latter has only one symmetry plane at $z = 0$, i.e., center of the slab.

solutions in even and odd sets, the TE and TM solutions are even and odd, respectively, with respect to any plane parallel to the photonic pattern. TE, TM and complete (both TM and TE) band gap have been successfully demonstrated for two-dimensional photonic crystals [21]. At the bottom of Fig. 6 we represent the slab case, where the dielectric thickness is of the order of the medium-wavelength of the system $d \sim \lambda$. There is only one symmetry plane at $z = 0$ (center of the slab), and the solutions can be classified as even and odd with respect to this plane. At $z = 0$, the electric and magnetic fields are confined in the plane for even and odd modes, respectively, as in the fully two-dimensional case. Nevertheless, $z = \pm\delta$ are not symmetry planes of the system and all six the electromagnetic field components are in general non-vanishing, then, we cannot separate anymore the solutions in purely TE and TM modes. Odd and even low-frequency modes in slabs, however, resembles the two-dimensional pure solutions, as it is shown in the figure (bottom); at $z = \pm\delta$, with $\delta < 0.5d$, the electric and magnetic fields have in general in-plane dominant components for even and odd modes, respectively. The former behaves like a TE mode and the latter behaves like a TM mode. Hence, the even eigenmodes of two-dimensional photonic crystal slabs are known in the literature as TE-like modes, while the odd eigenmodes are known as TM-like modes.

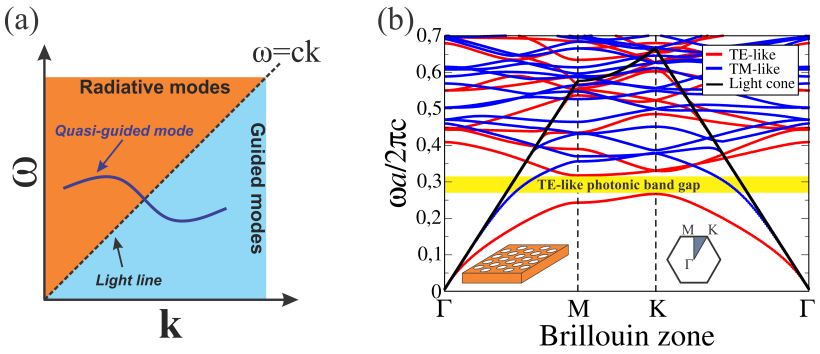

Figure 7: (a) Radiative and guided mode regions on the dispersion relation of a photonic crystal slab; the light line and a quasi-guided mode are illustrated. (b) Band diagram of a typical GaAs two-dimensional photonic crystal slab in the irreducible Brillouin zone.

Photonic band gaps for either TE-like or TM-like modes have been successfully demonstrated through theoretical and experimental studies [47, 48, 49, 50]. The fine-thickness condition along the vertical axis introduces new physical phenomena which are not present in the fully two-dimensional case. Since the space is open outside the photonic crystal slabs, the electromagnetic field is not bounded in this region and it determines a continuous spectrum. On the other hand, the electromagnetic field is bounded inside the slab and the spectrum is discrete. Discrete resonances, i.e., guided modes, can thus interact with the continuous spectrum, i.e., radiative (or leaky) modes, through the vertical boundary, allowing the possibility of energy flux from within to outside the photonic crystal, and vice versa. Figure 7(a) illustrates the radiative and guided mode zones in the band diagram of photonic crystal slabs. These regions are separated by the light line, which is defined as the dispersion relation of light in the outside medium; since we are interested in suspended membranes the frontier is defined by the dispersion relation of light in air [6], i.e., $\omega = ck$. Photonic resonances crossing the light line are called quasi-guided modes, and they are subject to out-of-plane diffraction losses, i.e., diffraction processes out of the waveguide plane for the Bloch waves propagating in the photonic crystal slab. In the radiative region of the band diagram, quasi-guided modes are discrete states within a continuum of states, which gives rise to Fano interference phenomena[7] [51, 52]. Panel (b) of Fig 7 shows a numerical calculation in dimen-

6 For a general asymmetric two-dimensional photonic crystal slab, where there is a substrate of refractive index n_1 and the outside medium has a refractive index n_3, the light lines are $\omega = ck/n_1$ and $\omega = ck/n_3$, and the frontier between the radiative and guided modes is determined by the light line with the largest refractive index.

7 Fano resonances are characterized by asymmetric peaks in the response function of the system, e.g., reflectivity spectrum. The asymmetry occurs in a frequency or energy interval which is smaller than the linewidth of the resonance.

sionless frequency units, using the guided mode expansion method (see following section), of a typical GaAs two-dimensional photonic crystal slab along the edges of the irreducible Brillouin zone. The crystal is formed by a hexagonal lattice of circular holes, with lattice parameter $a = 260$ nm and hole radius $r = 65$ nm, embedded in a slab of thickness $d = 120$ nm and refractive index $n = 3.41$. This photonic crystal has a TE-like bang gap, highlighted in yellow, between 0.267 and 0.318, or between 1.274 eV and 1.517 eV in electron-volt units, however, forbidden odd states are not favored by the system and TM-like band gaps are not present. The bands fully-below, fully-above and crossing the light line, correspond to guided, radiative (or leaky) and quasi-guided modes of the slab, respectively.

2.1.4 *The guided mode expansion method (GME)*

Over the last decade, several numerical methods have been proposed for studying photonic crystal slabs by solving the three-dimensional set of Maxwell's equations, which in general requires a huge numerical and computational effort. Some examples are the plane wave expansion with perfectly matched layers [53], the scattering matrix method [54] and the canonical finite-difference time-domain method (FDTD) [55], the latter has proved to be very flexible for solving the fields in any electromagnetic system, but computationally expensive [56]. Currently, the guided mode expansion method (GME) is the most efficient and reliable approach for solving the photonic dispersion and radiation losses of photonic crystal slabs, providing numerical and computational facilities due, mainly, to the analyticity of the matrix representation of Maxwell operator $\hat{\Theta}$. Since the GME method is the photonic-crystal-solver used in the present work, the key aspects of the method will be discussed in this section. For specific details the reader is referred to the original works cited in Refs. [48, 57].

2.1.4.1 *Photonic dispersion*

Starting from the wave equation of Eq. (4) with the corresponding transversality condition in Eq. (6), the magnetic field can be expanded in a set of basis as

$$\mathbf{H}(\mathbf{r}) = \sum_{\mu} c_{\mu} \mathbf{H}_{\mu}(\mathbf{r}), \tag{12}$$

subject to the orthonormality condition

$$\int \mathbf{H}^{*}_{\mu}(\mathbf{r}) \cdot \mathbf{H}_{\nu}(\mathbf{r}) d\mathbf{r} = \delta_{\mu\nu}. \tag{13}$$

Equation (4) is then transformed into a linear eigenvalue problem

$$\sum_{\nu} \mathcal{H}_{\mu\nu} c_{\nu} = \frac{\omega^2}{c^2} c_{\mu}, \tag{14}$$

where it is easy to show that the matrix elements $\mathcal{H}_{\mu\nu}$ are given by:

$$\mathcal{H}_{\mu\nu} = \int \frac{1}{\epsilon(\mathbf{r})} \left(\nabla \times \mathbf{H}^*_\mu(\mathbf{r})\right) \cdot \left(\nabla \times \mathbf{H}_\nu(\mathbf{r})\right) d\mathbf{r}. \tag{15}$$

An appropriate set $\{\mathbf{H}_\mu(\mathbf{r})\}$ for solving Eq. (14) in photonic crystal slabs is the basis of guided mode solutions of the effective planar waveguide. In Fig. 8(a) we show a schematic picture of the system we are interested in. Labeling $\mathbf{r}_{||} = (x, y)$ the in-plane coordinate vector, the photonic crystal slab, with dielectric function $\epsilon_2(\mathbf{r}_{||})$, is considered between two semi-infinite layers with dielectric functions $\epsilon_1(\mathbf{r}_{||})$ and $\epsilon_3(\mathbf{r}_{||})$, namely, the substrate and external media. The basis for expanding the system is defined by the homogeneous planar waveguide problem, shown in panel (b), with dielectric constants $\bar{\epsilon}_1$ (lower cladding), $\bar{\epsilon}_2$ (core) and $\bar{\epsilon}_3$ (upper cladding) determined by the averages of $\epsilon_i(\mathbf{r}_{||})$

$$\bar{\epsilon}_i = \frac{1}{A} \int_{cell} \epsilon_i(\mathbf{r}_{||}) d\mathbf{r}_{||}, \tag{16}$$

where the integral is over a unit cell of area A. In order to guided modes be supported by the effective slab, the condition $\bar{\epsilon}_2 > \bar{\epsilon}_1, \bar{\epsilon}_3$ must be fulfilled. Denoting by $\mathbf{g} = g\hat{\mathbf{g}}$ the two-dimensional wave vector in the xy plane, and by ω_g the frequency of a guided mode which satisfies $cg/\sqrt{\bar{\epsilon}_2} < \omega_g < cg/\max(\sqrt{\bar{\epsilon}_1}, \sqrt{\bar{\epsilon}_3})$ we define the following quantities:

$$\begin{aligned}
\chi_1 &= \left(g^2 - \bar{\epsilon}_1 \frac{\omega_g^2}{c^2}\right)^{1/2}, \\
q_g &= \left(\bar{\epsilon}_2 \frac{\omega_g^2}{c^2} - g^2\right)^{1/2}, \\
\chi_3 &= \left(g^2 - \bar{\epsilon}_3 \frac{\omega_g^2}{c^2}\right)^{1/2},
\end{aligned} \tag{17}$$

representing the real (imaginary) parts of the wave vector in the core (upper and lower cladding), respectively.

By applying Maxwell's equations to the waveguide problem, transverse-electric (electric field lying in the xy plane) and transverse-magnetic (magnetic field lying in the plane xy) solutions are determined, respectively, by the following implicit equations:

$$q(\chi_1 + \chi_3)\cos(qd) + (\chi_1\chi_3 - q^2)\sin(qd) = 0, \tag{18}$$

$$\frac{q}{\bar{\epsilon}_2}\left(\frac{\chi_1}{\bar{\epsilon}_1} + \frac{\chi_3}{\bar{\epsilon}_3}\right)\cos(qd) + \left(\frac{\chi_1\chi_3}{\bar{\epsilon}_1\bar{\epsilon}_3} - \frac{q^2}{\bar{\epsilon}_2^2}\right)\sin(qd) = 0, \tag{19}$$

where d is the slab thickness. Equations (18) and (19) come from the continuity conditions of the tangential components of the fields at the

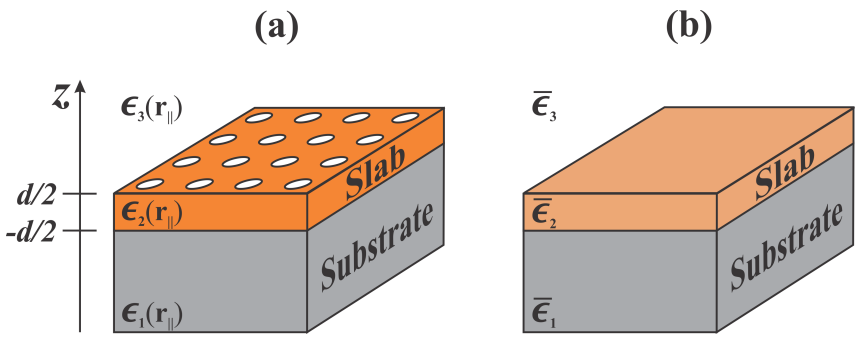

Figure 8: (a) Schematic picture of the photonic crystal slab, where $\mathbf{r}_{||}$ represents the in-plane coordinate vector. (b) Effective homogeneous problem for computing the guided mode basis where $\bar{\epsilon}_1$, $\bar{\epsilon}_2$ and $\bar{\epsilon}_3$ are the dielectric constants of the lower cladding, core and upper cladding, respectively.

waveguide interfaces, and the dispersion relation $\omega(g)$ of the waveguide is computed by solving these equations numerically. When symmetric planar wave guides are considered, i.e. $\bar{\epsilon}_1 = \bar{\epsilon}_3$ and $z = 0$ is a mirror symmetry plane, Eqs. (18) and (19) split into the following equations for odd and even solutions:

$$q \sin\left(\frac{qd}{2}\right) - \chi_1 \cos\left(\frac{qd}{2}\right) = 0, \quad \text{TE,} \quad \text{even,} \tag{20}$$

$$q \cos\left(\frac{qd}{2}\right) + \chi_1 \sin\left(\frac{qd}{2}\right) = 0, \quad \text{TE,} \quad \text{odd,} \tag{21}$$

$$\frac{q}{\bar{\epsilon}_2} \cos\left(\frac{qd}{2}\right) + \frac{\chi_1}{\bar{\epsilon}_1} \sin\left(\frac{qd}{2}\right) = 0, \quad \text{TM,} \quad \text{even,} \tag{22}$$

$$\frac{q}{\bar{\epsilon}_2} \sin\left(\frac{qd}{2}\right) - \frac{\chi_1}{\bar{\epsilon}_1} \cos\left(\frac{qd}{2}\right) = 0, \quad \text{TM.} \quad \text{odd} \tag{23}$$

The even and odd modes can hence be solved separately reducing the computational effort required by solving directly Eqs. (18) and (19). The solutions of the implicit equations Eqs. (20) to (23) are shown in Fig. 9, for the effective homogeneous slab associated to the system of Fig. 7(b), i.e., $\bar{\epsilon}_1 = \bar{\epsilon}_3 = 1$, $\bar{\epsilon}_2 = 9.218$ and $d = 120$ nm. Irrespective of the parity of the solutions, TE and TM bands alternate on the condition that the fundamental mode corresponds to a TE polarization. On the other hand, the parity alternates between even and odd solutions for TE and TM polarizations providing that the TE and TM fundamental modes have even and odd polarizations, respectively. Figure 9 shows that the wave vector $\mathbf{g}$ can take, in principle, any value in the xy plane for guided modes[8]. In the case of two-dimensional photonic crystal slabs, the modes have the Bloch form shown in Eq. (10), and the $\mathbf{k}$ vector is restricted to the first Brillouin zone; larger vectors in

8 Since the problem of the homogeneous waveguide is actually one-dimensional in Fig. 9 is shown the magnitude of $\mathbf{g}$.

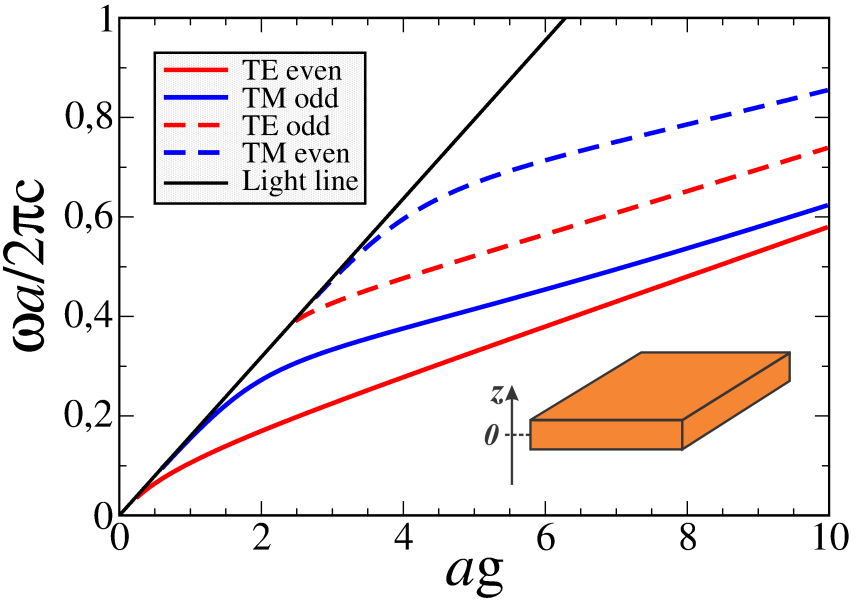

Figure 9: Dispersion relation of a symmetric planar waveguide with $\bar{\epsilon}_1 = \bar{\epsilon}_3 = 1$, $\bar{\epsilon}_2 = 9.218$ and $d = 120$ nm.

the reciprocal space are generated by adding to $\mathbf{k}$ the appropriate reciprocal lattice vector $\mathbf{G}$. Thus, when the photonic crystal is taken into account, the wave vector $\mathbf{g}$ can be written in terms of two contributions, the Bloch vector $\mathbf{k}$ and the reciprocal lattice vector $\mathbf{G}$, i.e., $\mathbf{g} = \mathbf{k} + \mathbf{G}$. The main effect of the periodic dielectric modulation on the guided bands of the homogeneous waveguide is to fold them to the first Brillouin zone, giving rise to photonic allowed and forbidden states. Denoting with α the α-th guided mode, the expansion of Eq. (12) is written for the guided mode basis as

$$\mathbf{H}(\mathbf{r}) = \sum_{\mathbf{G},\alpha} c(\mathbf{k}+\mathbf{G})\mathbf{H}^{guided}_{\mathbf{k}+\mathbf{G}}(\mathbf{r}), \tag{24}$$

where the sum is over the guided modes and reciprocal lattice vectors. The basis set must be truncated in order to obtain a finite number of linear equations determined by Eq. (14). The set of guided modes is truncated up to the α-th element, while the set of reciprocal vectors is truncated providing the cutoff condition $|\mathbf{G}| <= G_{max}$, where G_{max} is the maximum vector magnitude considered in the expansion [9]. To calculate the matrix elements in Eq. (15), the inverses of the dielectric functions are then expanded in a set of plane waves over the reciprocal lattice vectors

$$\epsilon_i(\mathbf{r}_{||})^{-1} = \sum_{\mathbf{G}} \eta_i(\mathbf{G}) e^{-i\mathbf{G}\cdot\mathbf{r}_{||}}, \tag{25}$$

9 This cutoff condition defines a circle centered at the origin of the reciprocal space with radius G_{max}, where only reciprocal lattice points inside the circle, with vector position $\mathbf{G}$, are considered in the expansion.

with Fourier coefficients

$$\eta_i(\mathbf{G}) = \frac{1}{A}\int_{cell} \epsilon_i(\mathbf{r}_{||})^{-1} e^{i\mathbf{G}\cdot\mathbf{r}_{||}} d\mathbf{r}_{||}, \tag{26}$$

where the integral extends over a unit cell of area A. The GME matrix elements $\mathcal{H}_{\mu\nu}$ are analytical and depend on the matrix elements of $\hat{\eta}_i$, defined as $\eta_i(\mathbf{G},\mathbf{G}') = \eta_i(\mathbf{G}'-\mathbf{G})$ [48]. A convenient approach for calculating the elements $\eta_i(\mathbf{G},\mathbf{G}')$ is based on the Fourier inverse rule or Ho-Chan-Soukoulis (HCS) method [42], where $\eta_i(\mathbf{G},\mathbf{G}')$ are computed by numerical inversion of the dielectric matrix $\hat{\epsilon}_i$, i.e., $\hat{\eta}_i = \hat{\epsilon}_i^{-1}$, with Fourier elements

$$\epsilon_i(\mathbf{G},\mathbf{G}') = \frac{1}{A}\int_{cell} \epsilon_i(\mathbf{r}_{||}) e^{i(\mathbf{G}'-\mathbf{G})\cdot\mathbf{r}_{||}} d\mathbf{r}_{||}, \tag{27}$$

This rule has shown to improve the convergence of numerical Fourier-based methods for truncated Fourier representation of discontinuous functions [58].

When the photonic structure has a center of inversion (symmetry point), the matrix elements $\eta_i(\mathbf{G},\mathbf{G}')$ and $\mathcal{H}_{\mu\nu}$ are real, then, Eq. (14) becomes a symmetric eigenvalue problem. In the most general case, where the photonic structures do not have a symmetry point, these matrix elements are complex and Eq. (14) determines a Hermitian eigenvalue problem. This is an important consideration because the computational effort for solving real eigenvalue problems is much lower than for solving the Hermitian ones. The construction of the matrix $\mathcal{H}_{\mu\nu}$ is illustrated in Fig. 10 for a one-dimensional slab photonic crystal with lattice parameter a. We consider $N_\alpha = 2$ guided modes and $N_G = 3$ plane waves. For each element of the basis μ, given a vector $\mathbf{k}$, we associate a guided mode index α and a reciprocal lattice vector $\mathbf{G}$ (plane wave element); the index μ is therefore univocally represented by $\mathbf{k}$, α and $\mathbf{G}$, i.e., $\mu = (\mathbf{k}+\mathbf{G},\alpha)$. As it is shown in the figure, three plane waves and two guided modes determine six orthonormal basis elements $\mathbf{H}_\mu$ for constructing the matrix $\mathcal{H}_{\mu\nu}$. Hence, the dimension of the eigenvalue problem for computing the photonic dispersion is $N_\alpha \times N_G$.

Although we have considered all the set of guided modes for calculating the photonic dispersion, this set is not complete since the leaky modes of the planar waveguide are not taken into account. The coupling of quasi-guided modes to all radiative spectrum produces a second-order shift which is not considered in the present formulation of the method; usually, this shift is of the order of a few per cent and increases for small dielectric contrast (weakly guided modes). Nevertheless, the first-order coupling to leaky modes above the light line at the same frequency is the dominant effect, leading to a radiative decay, i.e., imaginary part of frequency, which can be calculated using time-dependent perturbation theory.

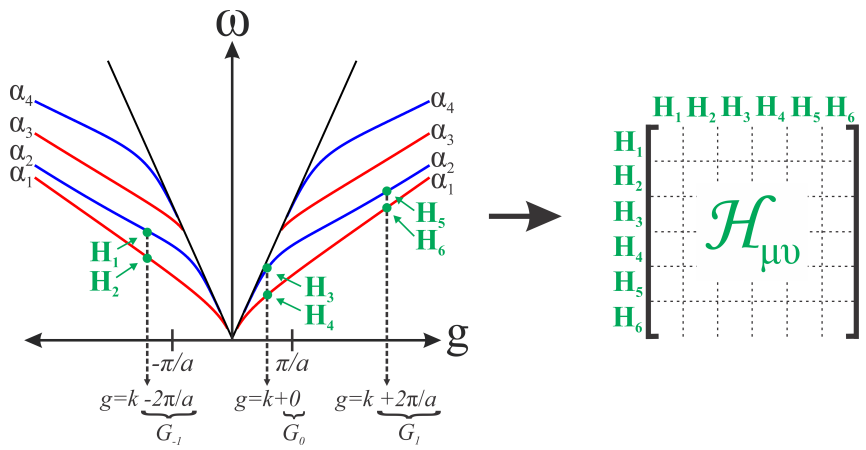

Figure 10: Schematic representation of the construction of the guided mode basis for calculating the matrix elements $\mathcal{H}_{\mu\nu}$ in a one-dimensional photonic crystal slab of lattice parameter a. For the sake of simplicity we consider only two guided modes and three plane waves.

2.1.4.2 *Radiation losses*

The periodic dielectric modulation of the photonic crystal slab folds the guided modes of the effective homogeneous waveguide, lying below the light line, to the first Brillouin zone of the photonic lattice. Therefore, photonic crystal resonances can fall above the light line allowing the coupling to radiative modes, i.e., they are subject to intrinsic losses due to scattering out of the plane. These radiation losses can be estimated through time-dependent perturbation theory using a formulation totally analogous to the Fermi's golden rule in quantum mechanics. The decay rate of a photonic crystal mode $|\mathbf{H}_{ph}\rangle$ to a continuum set of radiative modes $|\mathbf{H}_{rad}\rangle$, at a given frequency ω, can be represented by

$$\Gamma_{ph\to rad} \propto \sum_{rad} \left|\langle \mathbf{H}_{ph}|\hat{\mathbf{O}}_p|\mathbf{H}_{rad}\rangle\right|^2 \rho(\omega), \tag{28}$$

where $\rho(\omega)$ is the photonic density of radiative modes. Since the radiation losses are caused by the in-plane periodicity and the vertical boundary condition of the dielectric function, the perturbation operator is represent by $\hat{\mathbf{O}}_p \to \epsilon(\mathbf{r})^{-1}$. From Eq. (28), the following expression is obtained for the imaginary part of ω_k^2/c^2 at a given k in the first Brillouin zone [48, 59]:

$$\mathrm{Im}\left(\frac{\omega_k^2}{c^2}\right) = -\pi \sum_{\mathbf{G}'} \sum_{\lambda=TE,TM} \sum_{j=1,3} |\mathcal{H}_{\mathbf{k},rad}|^2 \, \rho_j\left(\mathbf{k}+\mathbf{G}', \frac{\omega_k^2}{c^2}\right), \tag{29}$$

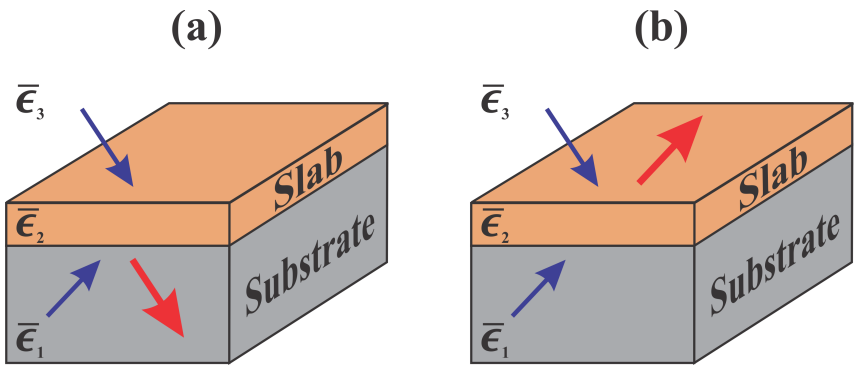

Figure 11: Representation of the scattering processes with outgoing components in lower (a) and upper (b) claddings.

where the matrix element between a photonic crystal mode and a leaky mode is

$$\mathcal{H}_{\mathbf{k},rad} = \int \frac{1}{\epsilon(\mathbf{r})} \left(\nabla \times \mathbf{H}^*_{\mathbf{k}}(\mathbf{r})\right) \cdot \left(\nabla \times \mathbf{H}^{rad}_{\mathbf{k}+\mathbf{G}',\lambda,j}(\mathbf{r})\right) d\mathbf{r}. \tag{30}$$

Equation (29) is known as the *photonic golden rule*. Since the field profile of a scattering state tends to a plane wave form in the far field, irrespective of the field profile of the photonic crystal slab modes, the mean approximation of the method is introduced by considering the radiative modes of the effective waveguide in the matrix elements of Eq. (30), and the following one-dimensional photonic density of states at a fixed in-plane wave vector $\mathbf{g}$

$$\begin{aligned}\rho_j\left(\mathbf{g}', \frac{\omega^2}{c^2}\right) &= \int_0^\infty \frac{dk_z}{2\pi} \delta\left(\frac{\omega^2}{c^2} - \frac{g^2 + k_z^2}{\bar{\epsilon}_j}\right) \\ &= \frac{\bar{\epsilon}_j^{1/2} c}{4\pi} \frac{\theta\left(\omega^2 - \frac{c^2 g^2}{\bar{\epsilon}_j}\right)^{1/2}}{\left(\omega^2 - \frac{c^2 g^2}{\bar{\epsilon}_j}\right)^{1/2}},\end{aligned} \tag{31}$$

which is valid for homogeneous planar waveguides. In Eq. (31) δ and θ are the Dirac delta and Heaviside functions, respectively. All lattice vectors $\mathbf{G}'$, polarizations λ and scattering processes $j = 1$ and $j = 3$ contribute to radiation losses. Such scattering processes, to be considered in the sum of Eq. 29, are illustrated in Fig. 11. The outgoing (radiative) components in the lower and upper claddings, which contribute to the diffraction losses, are represented by the red arrows in panels (a) and (b), respectively.

Using the expansion of $\mathbf{H}_{\mathbf{k}}$ shown in Eq. (24) over the set of guided modes, the matrix elements of Eq. (30) can be written as

$$\mathcal{H}_{\mathbf{k},rad} = \sum_{\mathbf{G},\alpha} c(\mathbf{k}+\mathbf{G},\alpha)^* \mathcal{H}_{guided,rad}, \tag{32}$$

where

$$\mathcal{H}_{guided,rad} = \int \frac{1}{\epsilon(\mathbf{r})} \left(\nabla \times \mathbf{H}^{guided}_{\mathbf{k}+\mathbf{G},\alpha}(\mathbf{r})^* \right) \cdot \left(\nabla \times \mathbf{H}^{rad}_{\mathbf{k}+\mathbf{G}',\lambda,j}(\mathbf{r}) \right) d\mathbf{r}. \quad (33)$$

The matrix elements $\mathcal{H}_{guided,rad}$ are analytical and the reader is referred to the works cited in Refs. [48, 57] for more details on their calculation. Finally, after computing $\mathrm{Im}(\omega_k^2)$ through Eq. (29), for a photonic mode with frequency ω_k, the quality factor can be calculated using the expression

$$Q_k = \frac{\omega_k}{2\mathrm{Im}\,(\omega_k)}, \quad (34)$$

where $\mathrm{Im}(\omega_k) = \mathrm{Im}(\omega_k^2)/[2\mathrm{Re}(\omega_k)]$.

2.2 SEMICONDUCTOR QUANTUM DOTS

The confinement of electrons in one, two and three dimensions in nano-structured semiconductors has been the focus of intense research during the last decades for applications on opto-electronic devices [60]. In particular, semiconductor quantum dots, in which electrons are subject to a three dimensional confinement, are characterized by their discrete spectra, long coherence time and large oscillator strengths [9]. These characteristics make them almost ideal artificial atoms that can be fixed in position and integrated into other semiconductor structures as photonic crystals, enabling new opportunities for on-chip quantum optics. In fact, quantum dots are promising candidates to realize solid state quantum bits (qubits) to be employed in quantum information and communication technologies [6, 7, 22].

InAs/GaAs/AlAs III-V semiconductor quantum dots, relevant for the present work, are fabricated by epitaxial methods such as molecular beam epitaxy, where the semiconductor heterostructure is grown layer by layer under high-vacuum conditions. The most common approach for generating InGaAs quantum dots is the Stranski-Krastanov method, where a thin wetting layer of InAs is deposited on GaAs; the difference between the InAs and GaAs lattice parameters (7%) generates a strain which is relaxed by the nucleation of randomly positioned islands, i.e., self-assembled quantum dots. They are subsequently covered by a GaAs layer with the aim of protecting them from surface states and oxidation [8]. Since the InGaAs gap is smaller than the GaAs one, the quantum dot determines three-dimensional confinement potentials in the valence and conduction bands, for holes and electrons, respectively. Figure 12 illustrates schematically such phenomena, where a InGaAs region is surrounded by GaAs.

In this section, a simple model for a quantum dot is presented and the R^{-3} dependence of the Förster mechanism in coupled quantum

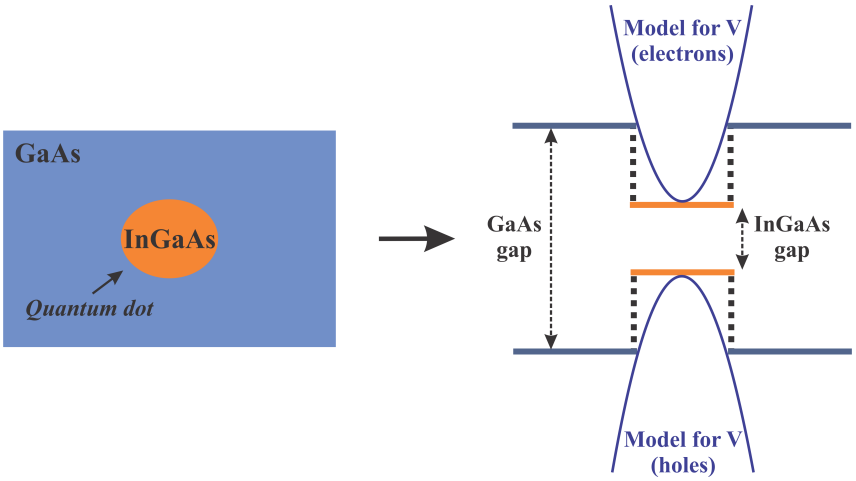

Figure 12: Schematic representation of a InGaAs quantum dot. The confinement potential is created by the different GaAs/InGaAs semiconductor band gaps.

dots is obtained. The results shown in the following were taken from the work cited in Ref. [23].

2.2.1 *Single-particle and exciton states*

The starting point for studying semiconductor quantum dots is the stationary single-particle Schrödinger equation, which can be written in the effective mass and envelope function approximations as

$$H_i(\mathbf{r})\phi_i(\mathbf{r}) = \left(-\frac{\hbar^2}{2}\nabla\frac{1}{m_i^*}\nabla + V_i(\mathbf{r})\right)\phi_i(\mathbf{r}) = E_i\phi_i(\mathbf{r}), \tag{35}$$

where $i = e, h$ denotes electrons or holes, m_i^* is the effective mass of the particle i and $V_i(\mathbf{r})$ is the three dimensional dot confinement potential due to the difference between the semiconductor gaps in the heterostructure, see Fig. 12. In Eq. (35) $\phi_i(\mathbf{r})$ is the envelope part of the total wavefunction

$$\psi_i(\mathbf{r}) = \phi_i(\mathbf{r})U_i(\mathbf{r}), \tag{36}$$

which describes the slowly varying contribution to the wavefunction over the dot region, and $U_i(\mathbf{r})$ is a rapidly varying periodic function with the period of the crystal lattice [61]. One of the most basic models for $V_i(\mathbf{r})$, providing analytical expressions for $\phi_i(\mathbf{r})$ and E_i, is the harmonic oscillator potential

$$V(x,y,z) = \frac{1}{2}m^*\omega_x^2x^2 + \frac{1}{2}m^*\omega_y^2y^2 + \frac{1}{2}m^*\omega_z^2z^2. \tag{37}$$

By considering the potential of Eq. (37) the Schrödinger equations in Eq. (35) becomes separable and the envelope function for electrons and holes can be written as a product of single-coordinate functions

$$\phi_i(\mathbf{r}) = \xi_{i,x}(x)\xi_{i,y}(y)\xi_{i,z}(z), \tag{38}$$

where ξ is the solution of the one-dimensional quantum harmonic oscillator:

$$\xi^n(x) = \left(\frac{1}{n!2^n d_x\sqrt{\pi}}\right)^{1/2} \mathcal{H}_n\left(\frac{x}{d_x}\right) e^{-\frac{x^2}{2d_x^2}}. \tag{39}$$

Here, n labels the quantum state with energy $E_n = (n+1/2)\hbar\omega_x$, $\mathcal{H}_n's$ are the Hermite polynomials and $d_x = [\hbar/(m^*\omega_x)]^{1/2}$. The ground-sate solution for electrons and holes is then given by the envelope function

$$\phi_i(x,y,z) = \left(\frac{1}{d_x d_y d_z \pi^{3/2}}\right)^{1/2} e^{-\frac{x^2}{2d_x^2}} e^{-\frac{y^2}{2d_y^2}} e^{-\frac{z^2}{2d_z^2}}, \tag{40}$$

with energy $E_0 = \frac{1}{2}\hbar(\omega_x + \omega_y + \omega_z)$.

When an electron is excited with enough energy to be promoted from the valence to the conduction bands, the total charge in the valence band is unbalanced diminishing in one unit the amount of negative charge, which determines an effective positive charge, i.e., a hole. Holes and electrons may form bound states through Coulomb interaction, in the same manner as protons and electrons in atoms. The bound states of electron-hole pairs in these artificial atoms, namely, quantum dots, are known as *excitons*, and they are considered in the electron-hole pair Hamiltonian

$$H = H_e + H_h - \frac{e^2}{4\pi\epsilon|\mathbf{r}_e - \mathbf{r}_h|} + E^{gap}, \tag{41}$$

where H_e and H_h are given by Eq. (35), ϵ is the background dielectric constant of the semiconductor and E^{gap} is the quantum dot band gap energy. The Coulomb term $H_{eh} = e^2/4\pi\epsilon|\mathbf{r}_e - \mathbf{r}_h|$ produces a small shift in the energy states for quantum dots whose sizes are smaller than the corresponding bulk exciton radius ($\sim$ 35 nm for InAs and $\sim$ 13 nm for GaAs); at this regime the Coulomb interaction can be considered as a perturbation and the energy spectrum is mainly determined by the confinement potentials. Then, the Hamiltonian of Eq. (41) can be rewritten as

$$H = H_0 + H_{eh}, \tag{42}$$

and the solutions of H_0, which are the antisymmetric excitonic wavefunctions, can be written in the following form:

$$\Psi = A\left[\psi'_n(\mathbf{r}_e, \sigma_e), \psi_m(\mathbf{r}_h, \sigma_h)\right], \tag{43}$$

where $\mathbf{r}$ and σ are position (with respect to the center of the dot) and spin variables, respectively, n and m labels the quantum states, and A represents overall antisymmetry. The wavefunction of Eq. (43) represents an electron $\psi'_n(\mathbf{r}_e, \sigma_e)$ which has been promoted from the valence band into a conduction band, while $\psi_m(\mathbf{r}_h, \sigma_h)$ represents the hole state created in the valence band. By considering the same potential in all three directions, i.e., $d_x = d_y = d_z = d = [\hbar/(m^*\omega)]^{1/2}$, the first order correction to the ground state energy due to the Coulomb interaction is given by [23]

$$E_{0,eh} = \langle \Psi_0 | H_{eh} | \Psi_0 \rangle = \frac{1}{2} \frac{e^2}{\pi^{3/2}\hbar^{1/2}\epsilon} \sqrt{\frac{m_e^* m_h^* \omega_e \omega_h}{m_e^* \omega_e + m_h^* \omega_h}}, \tag{44}$$

where the exchange interaction term, which is much smaller than the direct one[10], is not considered in this calculation.

2.2.2 *Förster coupling between two quantum dots*

Excitons from different quantum dots can be coupled via Coulomb interaction if the interdot distances are of the order of the dot sizes. In particular, the Förster coupling, which can be under certain conditions of dipole-dipole type, is responsible for resonant exciton exchange, or resonant energy transfer, between the quantum dots. The Förster interaction V_F can be estimated within first order perturbation theory by

$$V_F = \langle \Psi_i | H_F | \Psi_f \rangle, \tag{45}$$

considering the Coulomb Hamiltonian

$$H_F = \frac{1}{4\pi\epsilon} \frac{e^2}{|\mathbf{R} + \mathbf{r}_1 - \mathbf{r}_2|}, \tag{46}$$

where $\mathbf{R}$, $\mathbf{r}_1$ and $\mathbf{r}_2$ correspond to the interdot separation vector, and the position vectors defined from the centers of the dot 1 and dot 2, respectively. These vectors are schematically shown in Fig. 13 for two interacting quantum dots. For calculating the matrix element of Eq. (45), the following initial and final states can be considered:

$$\begin{aligned} \Psi_i &= A\left[\psi'_n(\mathbf{r}_1, \sigma_1), \psi_m(\mathbf{r}_2, \sigma_2)\right], \\ \Psi_f &= A\left[\psi_n(\mathbf{r}_1, \sigma_1), \psi'_m(\mathbf{r}_2, \sigma_2)\right]. \end{aligned} \tag{47}$$

Here, Ψ_i represents a conduction band state in dot 1 and a valence band state in dot 2, and Ψ_f represents a valence band state in dot 1 and a conduction band state in dot 2, i.e, a resonant exciton transfer

10 The exchange interaction term comes from the integrals with arguments of the form $\psi'^*_n(\mathbf{r}_1)\psi_m(\mathbf{r}_1)\psi'_n(\mathbf{r}_2)\psi^*_m(\mathbf{r}_2)$, while the direct interaction term comes from the integrals with arguments of the form $\psi'^*_n(\mathbf{r}_1)\psi'_n(\mathbf{r}_1)\psi^*_m(\mathbf{r}_2)\psi_m(\mathbf{r}_2)$.

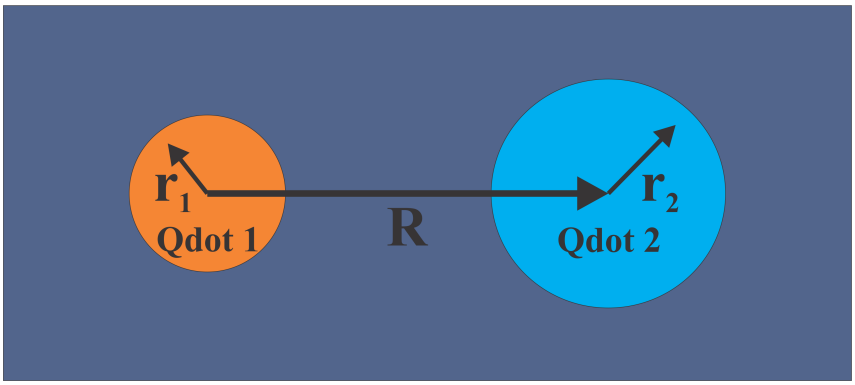

Figure 13: Schematic illustration of two interacting quantum dots.

from dot 1 to dot 2 mediated by the Coulomb interaction. The direct matrix element of Eq. (45) is then given by

$$V_F = -\frac{e^2}{4\pi\epsilon}\int\int \psi'^{*}_n(\mathbf{r}_1)\psi_n(\mathbf{r}_1)\frac{1}{|\mathbf{R}+\mathbf{r}_1-\mathbf{r}_2|}\psi^{*}_m(\mathbf{r}_2)\psi'_m(\mathbf{r}_2)d\mathbf{r}_1\,d\mathbf{r}_2. \quad (48)$$

The Coulomb term in Eq. (48) can be expanded in Taylor series about the vector $\mathbf{R}$ up to second order for $|\mathbf{R}| \gg |\mathbf{r}_1 - \mathbf{r}_2|$, leading to the following expression for the Förster interaction energy:

$$V_F = -\frac{e^2}{4\pi\epsilon R^3}\left[\langle\mathbf{r}_I\rangle\cdot\langle\mathbf{r}_{II}\rangle - \frac{3}{R^2}\left(\langle\mathbf{r}_I\rangle\cdot\mathbf{R}\right)\left(\langle\mathbf{r}_{II}\rangle\cdot\mathbf{R}\right)\right], \quad (49)$$

where the integrals

$$\langle\mathbf{r}_I\rangle = \int \psi'^{*}_n(\mathbf{r}_1)\mathbf{r}_1\psi_n(\mathbf{r}_1)d\mathbf{r}_1, \quad (50)$$
$$\langle\mathbf{r}_{II}\rangle = \int \psi^{*}_m(\mathbf{r}_2)\mathbf{r}_2\psi'_m(\mathbf{r}_2)d\mathbf{r}_2,$$

are calculated on dot 1 and 2, respectively, between an electron (ψ') and a hole (ψ) states. The behavior of the Förster coupling as a function of R is clearly seen From Eq. (49); for $|\mathbf{R}| \gg |\mathbf{r}_1 - \mathbf{r}_2|$ the Förster energy transfer mechanism displays a R^{-3} dependence. This short-range interaction is a great limitation for independent manipulation of the quantum dots when they are strongly coupled, which is crucial for quantum information applications. In view of solving such limitation, the present work explores the possibility of using photonic modes for long-range dot-dot interaction beyond the Förster regime.

2.3 SEMICONDUCTOR QUANTUM DOTS IN PHOTONIC CRYSTALS

The possibility of quantum information processing lies on realizing controlled gate operations with two interacting qubits using a *quantum bus*, namely, a physical degree of freedom which interacts with

all localized qubits. For solid state qubits, i.e., quantum dots, the photons are the best candidates to achieve such a quantum bus platform, due to their long coherence time and high velocity. In view of this, there is a growing theoretical and experimental interest to control the photon-mediated interaction (radiative coupling) between two quantum dots through the electromagnetic modes in a semiconductor photonic crystal structure [24, 25, 62]. Due to their exceptional capabilities to efficiently guide and confine the electromagnetic radiation, and the high degree of precision in fabrication techniques currently achieved, photonic crystals should allow to overcome the short-range Förster coupling between interacting quantum dots, thus achieving sizable effective radiative interaction at distances quite larger than their emission wavelength [29].

The radiative coupling between quantum dots is discussed in this section within a semiclassical formalism. Furthermore, a fully quantum mechanical formulation of the problem is presented for quantifying the amount of entanglement between quantum dots, which are coupled via photon-mediated interactions.

2.3.1 *Semiclassical formalism*

A useful semiclassical formalism was described by Minkov and Savona in Reference [26] to study N quantum dots coupled to M electromagnetic photonic modes in an arbitrary dielectric structure. Following this work, our starting point is the inhomogeneous wave equation for the electric field [see Eq. (5)] with a polarization vector source, which can be written in Gaussian units as follows:

$$\nabla \times \nabla \times \mathbf{E}(\mathbf{r},\omega) - \frac{\omega^2}{c^2}\left[\epsilon(\mathbf{r})\mathbf{E}(\mathbf{r},\omega) + 4\pi\mathbf{P}(\mathbf{r},\omega)\right] = 0. \tag{51}$$

The underlying photonic structure is considered through the spatial dependence of the dielectric function $\epsilon(\mathbf{r})$, while the linear optical response of the quantum dots is included through a nonlocal susceptibility tensor in the polarization vector

$$\mathbf{P}(\mathbf{r},\omega) = \int \hat{\chi}(\mathbf{r},\mathbf{r}',\omega)\mathbf{E}(\mathbf{r},\omega)\,d\mathbf{r}'. \tag{52}$$

We will consider the specific case of excitons originating from the heavy-hole band of a semiconductor with cubic symmetry (e.g. InAs). In this case the $\mathbf{x}$ and $\mathbf{y}$ components of the polarization couple to the electromagnetic field according to the following susceptibility tensor[63, 64]:

$$\hat{\chi}(\mathbf{r},\mathbf{r}',\omega) = \frac{\mu_{cv}^2}{\hbar}\sum_{\alpha=1}^{N}\frac{\Psi_\alpha^*(\mathbf{r})\Psi_\alpha(\mathbf{r}')}{\omega^{(\alpha)}-\omega}\begin{pmatrix}1&0&0\\0&1&0\\0&0&0\end{pmatrix}, \tag{53}$$

where α runs over all dots, μ_{cv} is the dipole matrix element of the inter-band optical transition, $\Psi_\alpha(\mathbf{r}) = \Psi_\alpha(\mathbf{r}_e = \mathbf{r}, \mathbf{r}_h = \mathbf{r})$, and $\Psi_\alpha(\mathbf{r}_e, \mathbf{r}_h)$ is the quantum dot excitonic wavefunction normalized as

$$\int\int |\Psi_\alpha(\mathbf{r}_e, \mathbf{r}_h)|^2 \, d\mathbf{r}_e d\mathbf{r}_h = 1. \tag{54}$$

The frequencies of the bare excitons are denoted by bracketed superscripts in order to distinguish them from the frequencies of photonic resonances, which will be denoted by subscripts, i.e., as ω_m. In this treatment all the frequencies are assumed to be complex quantities, i.e., $\omega^{(\alpha)} = \mathrm{Re}\{\omega^{(\alpha)}\} - i\gamma^{(\alpha)}/2$ and $\omega_m = \mathrm{Re}\{\omega_m\} - i\gamma_m/2$, where $\gamma^{(\alpha)}$ represents the overall decay rate of the exciton state associated to the quantum dot α, and γ_m represents intrinsic and extrinsic losses of the photonic mode m.

Introducing the quantities $\mathbf{Q}(\mathbf{r}, \omega) = \sqrt{\epsilon(\mathbf{r})}\mathbf{E}(\mathbf{r}, \omega)$, the wave equation Eq. (51) is turned into a self-adjoint inhomogeneous differential equation [3]:

$$\Upsilon\mathbf{Q}(\mathbf{r}, \omega) - \frac{\omega^2}{c^2}\mathbf{Q}(\mathbf{r}, \omega) = \frac{4\pi}{\sqrt{\epsilon(\mathbf{r})}}\frac{\omega^2}{c^2}\int \hat{\chi}(\mathbf{r}, \mathbf{r}', \omega)\frac{\mathbf{Q}(\mathbf{r}', \omega)}{\sqrt{\epsilon(\mathbf{r}')}}d\mathbf{r}', \tag{55}$$

with associated self-adjoint differential operator

$$\Upsilon = \frac{1}{\sqrt{\epsilon(\mathbf{r})}}\nabla \times \nabla \times \frac{1}{\sqrt{\epsilon(\mathbf{r})}}. \tag{56}$$

Since the susceptibility tensor in Eq. (53) decouples the $\mathbf{z}$-polarized fields, we define the two-dimensional field $\mathbf{Q} = (Q_x, Q_y)$, and we can express the formal solution of the inhomogeneous problem of Eq. (55) using the Green's function approach:

$$\begin{aligned}\mathbf{Q}(\mathbf{r}, \omega) =& \mathbf{Q}_0(\mathbf{r}, \omega) + \\ & \frac{4\pi}{\sqrt{\epsilon(\mathbf{r})}}\frac{\omega^2}{c^2}\int d\mathbf{r}' \int d\mathbf{r}'' \hat{G}(\mathbf{r}, \mathbf{r}', \omega)\frac{\hat{\chi}(\mathbf{r}', \mathbf{r}'', \omega)}{\sqrt{\epsilon(\mathbf{r}'')}}\mathbf{Q}(\mathbf{r}'', \omega).\end{aligned} \tag{57}$$

The Green's tensor can be expanded onto the set of the orthonormal eigenfunctions of the self-adjoint operator of Eq. (56):

$$\hat{G}(\mathbf{r}, \mathbf{r}', \omega) = \sum_m \frac{\mathbf{Q}_m(\mathbf{r}) \otimes \mathbf{Q}_m^*(\mathbf{r}')}{\frac{\omega_m^2}{c^2} - \frac{\omega^2}{c^2}}, \tag{58}$$

where the outer product is defined as

$$\mathbf{A} \otimes \mathbf{B} = \begin{pmatrix} A_x B_x & A_x B_y \\ A_y B_x & A_y B_y \end{pmatrix}. \tag{59}$$

In the vast majority of structures, the quantum dots are embedded within a semiconductor dielectric medium of dielectric constant ϵ_∞, i.e., the wave functions are non-negligible only in the region where $\epsilon(\mathbf{r}) = \epsilon_\infty$. Thus, we can safely substitute $\sqrt{\epsilon(\mathbf{r}')} = \sqrt{\epsilon(\mathbf{r}'')} = \epsilon_\infty$ in Eq. (57), since the $\mathbf{r}$ dependence of all quantities will be considered into the overlap integrals with the quantum dot wavefunctions. Furthermore, a very good approximation consists in replacing the ω on the right side of Eq. (57), as well as $(\omega_m + \omega)/2$, obtained from the factorization of the denominator in Eq. (58), with an average exciton transition frequency, ω_0. The resonances of the coupled system are computed considering the homogeneous problem associated to Eq. (57) (without $\mathbf{Q}_0(\mathbf{r}, \omega)$), which determines the particular solution of Eq. (55). Then, defining

$$\mathbf{Q}^\alpha(\omega) = \int \Psi_\alpha \mathbf{Q}(\mathbf{r}, \omega) d\mathbf{r}, \tag{60}$$

we obtain

$$\mathbf{Q}(\mathbf{r}, \omega) = \frac{2\pi\omega_0}{\epsilon_\infty} \frac{\mu_{cv}^2}{\hbar} \sum_{\alpha=1}^{N} \sum_{m=1}^{M} \frac{\mathbf{Q}_m(\mathbf{r}) \otimes \mathbf{Q}_m^{\alpha*}}{(\omega_m - \omega)(\omega^{(\alpha)} - \omega)} \mathbf{Q}^\alpha(\omega). \tag{61}$$

Integrating Eq. (61) with $\int d\mathbf{r} \Psi_\beta(\mathbf{r})$ and defining $\widetilde{\mathbf{Q}}(\omega) = \mathbf{Q}^\alpha(\omega)/(\omega^{(\alpha)} - \omega)$, the following set of equations are obtained for the complex frequency poles:

$$(\omega^{(\beta)} - \omega)\widetilde{\mathbf{Q}}^\beta(\omega) = \frac{2\pi\omega_0}{\epsilon_\infty} \frac{\mu_{cv}^2}{\hbar} \sum_{\alpha=1}^{N} \sum_{m=1}^{M} \frac{\mathbf{Q}_m^\beta \otimes \mathbf{Q}_m^{\alpha*}}{(\omega_m - \omega)} \widetilde{\mathbf{Q}}^\alpha(\omega). \tag{62}$$

It is easy to show that the nonlinear system of Eq. (62) is mathematically equivalent to diagonalize the matrix [26]

$$\Lambda = \begin{pmatrix} \omega_x^{(1)} & 0 & \cdots & 0 & g_{1,x}^1 & \cdots & g_{M,x}^1 \\ 0 & \omega_y^{(1)} & \cdots & 0 & g_{1,y}^1 & \cdots & g_{M,y}^1 \\ \vdots & \cdots & \ddots & \vdots & \vdots & \cdots & \vdots \\ 0 & 0 & \cdots & \omega_y^{(N)} & g_{1,y}^N & \cdots & g_{M,y}^N \\ g_{1,x}^{1*} & g_{1,y}^{1*} & \cdots & g_{1,y}^{N*} & \omega_1 & \cdots & 0 \\ \vdots & \cdots & \ddots & \vdots & \vdots & \cdots & \vdots \\ g_{M,x}^{1*} & g_{M,y}^{1*} & \cdots & g_{M,y}^{N*} & 0 & \cdots & \omega_M \end{pmatrix}, \tag{63}$$

where possible deviations from the perfectly symmetrical quantum dots can be introduced in the model through different transition frequencies in the x and y directions, respectively. The $\mathbf{g}_m^\alpha$ elements are interpreted as the coupling strengths between the m-th mode of the photonic crystal and the α-th quantum dot, and they are defined as

$$\mathbf{g}_m^\alpha = \left(g_{m,x}^\alpha, g_{m,y}^\alpha\right) = \left(\frac{2\pi\omega_0}{\epsilon_\infty}\frac{\mu_{cv}^2}{\hbar}\right)^{1/2}\mathbf{Q}_m^\alpha. \tag{64}$$

The $2N + M$ complex eigenvalues of Λ define the frequencies (real part) and loss rates ($-2\times$ imaginary part) of the mixed excitations of the system, known as *polaritons*, and their corresponding eigenvectors

$$\boldsymbol{\lambda} = \left(\lambda_x^1, \lambda_y^1, \ldots, \lambda_x^N, \lambda_y^N, \lambda_1, \ldots, \lambda_M\right), \tag{65}$$

define the Hopfield coefficients, whose square moduli are interpreted as the bare-exciton (or bare-photon) fractions of the polariton state [65, 66].

For typical self-organized InGaAs quantum dots, whose size lies in the 10-20 nm range and the exciton recombination energy is ~ 1.3 eV ($\lambda \approx 950$ nm), a point dipole assumption, $\Psi_\alpha(\mathbf{r}) = C\delta(\mathbf{r} - \mathbf{r}_\alpha)$, is a very good approximation because the electric field varies weakly in a region where $\Psi_\alpha(\mathbf{r})$ is non-negligible. Since the wave function is not properly normalized at equal electron and hole positions, the constant C, which depends on the oscillator strength, can be estimated through experimental measurements of the quantum dot radiative decay rate. Following Minkov and Savona [26], and Parascandolo and Savona [67], with a radiative lifetime of 1 ns and excitation energy $\hbar\omega_0 \approx 1.3$ eV, the square dipole moment is found to be $d^2 \approx 0.51$ eV nm^3, which is related to C through the expression:

$$d^2 = \mu_{cv}^2 C^2. \tag{66}$$

Within the point dipole approximation, the coupling constants of Eq. (64) are turned into the simple following form:

$$\mathbf{g}_m^\alpha = \left(g_{m,x}^\alpha, g_{m,y}^\alpha\right) = \left(\frac{2\pi\omega_0}{\epsilon_\infty\hbar}\right)^{1/2} d\,\mathbf{Q}_m(\mathbf{r}_\alpha). \tag{67}$$

From Eq. (62) we define the following tensor [33]:

$$\hat{G}^{\alpha\beta}(\omega) = \sum_{m=1}^{M}\frac{\mathbf{g}_m^\beta \otimes \mathbf{g}_m^{\alpha *}}{(\omega_m - \omega)} = d^2\frac{2\pi}{\epsilon_\infty\hbar}\frac{\omega^2}{c^2}\hat{G}(\mathbf{r}_\alpha, \mathbf{r}_\beta, \omega), \tag{68}$$

where $\hat{G}(\mathbf{r}_\alpha, \mathbf{r}_\beta, \omega)$ is the Green's tensor evaluated at the quantum dot positions $\mathbf{r}_\alpha$ and $\mathbf{r}_\beta$. The components $G_{xx}^{\alpha\beta}$, $G_{xy}^{\alpha\beta}$, $G_{yx}^{\alpha\beta}$ and $G_{yy}^{\alpha\beta}$ are interpreted as the effective radiative coupling strengths between the

dot α and dot β at the excitonic transition frequency ω.

Finally, the last requirement of the model are the values of the normalized photonic eigenmodes $\mathbf{Q}_m$ at the quantum dot positions, and their corresponding eigenfrequencies and loss rates, which are computed using standard methods to solve photonic crystal structures. Since we are interested in studying the radiative interaction between quantum dots in photonic crystal slabs molecules, we employ the guided mode expansion approach for this task, which is the best compromise between computational effort and reliable results for extended and strong localized modes in high dielectric regions.

2.3.2 *Quantum formalism*

The quantum theory of electromagnetic fields commonly adopted in quantum optics books, and their corresponding interaction with localized quantum emitters, does not consider the spatial dependence of the dielectric permittivity [68, 69]. Some of these approaches are even restricted to vacuum only. The rigorous formulation of the fully quantum radiation-matter interaction problem in spatially dependent dielectric materials is lengthy and not trivial, and it has been addressed in Refs. [70, 71], where the so called *multipolar Hamiltonian*[11] is formally deduced. The details of this field quantization are not presented here and the reader is referred to the original works.

We start from the second-quantized multipolar Hamiltonian for the case of neutral, stationary radiative quantum emitters in a neutral, nonconducting, dielectric medium in the dipole and rotating wave approximations[12]:

$$\hat{H}_0 = \sum_n \hbar\omega_n \hat{a}_n^\dagger \hat{a}_n + \sum_\alpha \hbar\omega^{(\alpha)} \hat{b}_\alpha^\dagger \hat{b}_\alpha + \hbar \sum_{n\alpha} \left(g_n^{*\alpha} \hat{a}_n^\dagger \hat{b}_\alpha + g_n^\alpha \hat{a}_n \hat{b}_\alpha^\dagger \right), \tag{69}$$

where ω_n and $\omega^{(\alpha)}$ denote the frequency of the photonic mode n and the excitonic transition frequency of the quantum dot α, respectively;

11 All the multipolar contributions are considered in the field-matter coupling.

12 When the wavefunction of the quantum emitters varies vary rapidly in relation to the electric field, a very good approximation is to consider a dipole radiation-matter coupling, i.e., the quantum emitter does not feel electric field variations and the value of the field amplitude is approximately constant in the region where the wavefunction is non-negligible. This is the so called *dipole approximation*. Moreover, when we are interested in the resonant regime of the system, terms with very high frequency in the radiation-matter coupling can be safely neglected. These rapidly rotating terms usually have the forms $\hat{a}_n^\dagger \hat{b}_\alpha^\dagger$ and $\hat{a}_n \hat{b}_\alpha$. This is the so called *rotating wave approximation*.

$\hat{a}_n^\dagger$ ($\hat{a}_n$) denotes the creation (destruction) operator of photons in the photonic mode n, satisfying bosonic commutation relations

$$\left[\hat{a}_n, \hat{a}_m^\dagger\right] = \delta_{nm}, \tag{70}$$

and all other commutators vanish, while $\hat{b}_n^\dagger$ ($\hat{b}_n$) denotes the creation (destruction) operator of electron-hole pairs in the quantum dot n, satisfying fermionic anticommutation relations

$$\left\{\hat{b}_\alpha, \hat{b}_\mu^\dagger\right\} = \delta_{\alpha\mu}, \tag{71}$$

and all other anticommutators vanish. In the present theory, the light-matter coupling strength between the mode n and the quantum dot α is given in Gaussian units as [25]

$$g_n^\alpha = \sqrt{\frac{2\pi\omega^{(\alpha)}}{\hbar}}\mathbf{d}_\alpha \cdot \mathbf{E}_n(\mathbf{r}_\alpha), \tag{72}$$

where $\mathbf{d}_\alpha = d_\alpha \mathbf{e}_\alpha$ denotes the dipole moment of the quantum dot α with magnitude d_α and orientation $\mathbf{e}_\alpha$, and $\mathbf{E}_n$ are the eigenmodes of Eq. (5) subject to the normalization condition

$$\int \epsilon(\mathbf{r})\mathbf{E}_n^*(\mathbf{r}) \cdot \mathbf{E}_m(\mathbf{r})d\mathbf{r} = \delta_{nm}. \tag{73}$$

Equation (72) is totally equivalent to Eq. (67) obtained by semiclassical means. In the present approach, mutual coupling between semiconductor quantum dots is not considered because we are interested in dot separations which are beyond the Förster and exchange (tunneling) regimes. However, all photonic modes interact with all quantum dots, giving rise to an indirect photon-mediated interaction between them, i.e., to a radiative coupling.

We now consider an exciton coherent pumping in the Hamiltonian of Eq. (69) through the driven term

$$\hat{H}_p(t) = \hbar \sum_\alpha \left[\Lambda_\alpha(t)e^{-i\omega_p t}\hat{b}_\alpha^\dagger + \Lambda_\alpha^*(t)e^{i\omega_p t}\hat{b}_\alpha\right], \tag{74}$$

where $\Lambda_\alpha(t)$ is the pumping rate at which are coherently created electron-hole pairs in the quantum dot α by a pump laser or electric potential with frequency ω_p. Here, we focus on the continuous wave excitation regime, in which the pumping rates $\Lambda_\alpha(t)$ are time independent and can be written in the form $\Lambda_\alpha(t) = \Omega_\alpha e^{i\phi_\alpha}$, where Ω_α is a real amplitude and ϕ_α is a real phase. The total Hamiltonian of the system is then written as

$$\hat{H}(t) = \hat{H}_0 + \hbar \sum_\alpha \left[\Omega_\alpha e^{-i(\omega_p t - \phi_\alpha)}\hat{b}_\alpha^\dagger + \Omega_\alpha^* e^{i(\omega_p t - \phi_\alpha)}\hat{b}_\alpha\right]. \tag{75}$$

With the purpose of eliminating the explicit temporal dependence of the Hamiltonian in Eq. (75), the system dynamics can be described in a rotating frame of reference with frequency ω_p by applying the operator

$$\hat{R}(t) = \exp\left[i\omega_p t\left(\sum_n \hat{a}_n^\dagger \hat{a}_n + \sum_\alpha \hat{b}_\alpha^\dagger \hat{b}_\alpha\right)\right], \tag{76}$$

determining an effective Hamiltonian $\hat{H}_{eff} = \hat{R}\hat{H}\hat{R}^\dagger - i\hbar\hat{R}\left(d\hat{R}^\dagger/dt\right)$, i.e.,

$$\begin{aligned}\hat{H}_{eff} = \sum_n \hbar\bar{\omega}_n \hat{a}_n^\dagger \hat{a}_n + \sum_\alpha \hbar\bar{\omega}^{(\alpha)} \hat{b}_\alpha^\dagger \hat{b}_\alpha \\ + \hbar\sum_{n\alpha}\left(g_n^{*\alpha}\hat{a}_n^\dagger \hat{b}_\alpha + g_n^\alpha \hat{a}_n \hat{b}_\alpha^\dagger\right) \\ + \hbar\sum_\alpha\left(\Omega_\alpha e^{i\phi_\alpha}\hat{b}_\alpha^\dagger + \Omega_\alpha^* e^{-i\phi_\alpha}\hat{b}_\alpha\right),\end{aligned} \tag{77}$$

where $\bar{\omega}_n = \omega_n - \omega_p$ and $\bar{\omega}^{(\alpha)} = \omega^{(\alpha)} - \omega_p$.

We adopt the master equation formalism for describing the dissipative dynamics of the system, which is written in Markov approximation for the rotated density matrix, $\tilde{\rho} = \hat{R}\rho\hat{R}^\dagger$, as:

$$\frac{d\tilde{\rho}}{dt} = \frac{i}{\hbar}\left[\tilde{\rho}, \hat{H}_{eff}\right] + \sum_m \hat{\mathcal{L}}(\gamma_m) + \sum_\alpha \hat{\mathcal{L}}(\gamma^{(\alpha)}), \tag{78}$$

where

$$\hat{\mathcal{L}}(\gamma_m) = \gamma_m\left(\hat{a}_m\tilde{\rho}\hat{a}_m^\dagger - \hat{a}_m^\dagger\hat{a}_m\tilde{\rho}/2 - \tilde{\rho}\hat{a}_m^\dagger\hat{a}_m/2\right), \tag{79}$$

and

$$\hat{\mathcal{L}}(\gamma^{(\alpha)}) = \gamma^{(\alpha)}\left(\hat{b}_\alpha\tilde{\rho}\hat{b}_\alpha^\dagger - \hat{b}_\alpha^\dagger\hat{b}_\alpha\tilde{\rho}/2 - \tilde{\rho}\hat{b}_\alpha^\dagger\hat{b}_\alpha/2\right), \tag{80}$$

are the Lindblad operators corresponding to the radiative losses of the photonic mode m at a rate γ_m (intrinsic and extrinsic losses[13]) and the losses by spontaneous emission in the quantum dot α at exciton decay rate $\gamma^{(\alpha)}$. The master equation of Eq. (78) is obtained by considering that the system is coupled to a broadband spectrum and very large (immense number of degrees of freedom) ensemble of harmonic oscillators at thermal equilibrium, known as bath or reservoir, leading to a irreversible damping and quantum decoherence. The system-reservoir dynamics, $\rho_{sr}(t)$, is solved using time-dependent perturbation theory up to second order (the system is assumed to be weakly coupled to the reservoir), and the total density operator is traced over

13 The extrinsic losses is attributed to intentionally-induced or fabrication disorder on the photonic crystal structure.

the reservoir to obtain the reduced density operator of the system, $\rho_s(t)$. The characteristic times of $\rho_s(t)$ are subsequently assumed to be long compared to the inverse bandwidth τ_r of the reservoir, obtaining an equation for $\rho_s(t)$, namely, the master equation, valid in this time regime [69]. The latter assumption is the so called *Markov approximation*. Pure dephasing of the quantum dot transitions can be taken into account by an additional Lindblad term

$$\hat{\mathcal{L}}_d(\gamma_d^{(\alpha)}) = \gamma_d^{(\alpha)} \left[\hat{b}_\alpha^\dagger \hat{b}_\alpha \tilde{\rho} \hat{b}_\alpha^\dagger \hat{b}_\alpha - (\hat{b}_\alpha^\dagger \hat{b}_\alpha)^2 \tilde{\rho}/2 - \tilde{\rho} (\hat{b}_\alpha^\dagger \hat{b}_\alpha)^2/2 \right], \quad (81)$$

where $\gamma_d^{(m)}$ represents a pure dephasing rate. Lindblad dissipation terms associated to incoherent pumping could also be considered in the master equation [24], however, since we are interested in low excitation, low temperature and resonant excitation regimes, they are safely neglected. Finally, the steady state of the system, $\tilde{\rho}_{ss}$ is found by solving the equation

$$\frac{d\tilde{\rho}}{dt} = 0, \quad (82)$$

which determines a linear system of algebraic equations that must be inverted to obtain $\tilde{\rho}_{ss}$. Such an approach is however computationally expensive and very inefficient for large Hilbert spaces. In order to avoid numerical inversions, the system of Eq. (82) can be turned into an eigenvalue problem by following the next steps. First, we take advantage of the linearity of master equation and write Eq. (78) in the form

$$\frac{d\tilde{\rho}}{dt} = \hat{\mathcal{T}}\tilde{\rho}, \quad (83)$$

by constructing the right operators $\hat{\mathcal{O}}_R$ which satisfy the relation

$$\tilde{\rho}\hat{\mathcal{O}} = \hat{\mathcal{O}}_R \tilde{\rho} \quad (84)$$

where $\hat{\mathcal{O}}$ represents any operator of Eq. (78) on the right side of $\tilde{\rho}$. Second, considering that Eq. (83) has dimension N, we define the column vector $[\tilde{\rho}]$ with dimension N^2 and the matrix $[\![\hat{\mathcal{T}}]\!]$ with dimension $N^2 \times N^2$ such that

$$[\![\hat{\mathcal{T}}]\!][\tilde{\rho}] = [\hat{\mathcal{T}}\tilde{\rho}]. \quad (85)$$

Third, we define the eigenvalue problem

$$[\![\hat{\mathcal{T}}]\!][\tilde{\rho}] = \lambda[\tilde{\rho}], \quad (86)$$

where the steady state solution correspond to the eigenstate with corresponding eigenvalue $\lambda = 0$. Finally, the steady state density matrix $\tilde{\rho}_{ss}$ is constructed from the eigenvector $[\tilde{\rho}]_{ss}$ following the rule of Eq. (85). Because $[\![\hat{\mathcal{T}}]\!]$ usually is a very sparse matrix, the computational effort required to solve the zero-eigenvalue of Eq. (86) is smaller than the effort required to numerically invert the system of equations given by Eq. (82).

2.3.2.1 *Two-qubit entanglement*

Two quantum mechanical systems ρ_1 and ρ_2 whose total density operator cannot be written in the factorized form

$$\rho_T = \rho_1 \otimes \rho_2, \tag{87}$$

are said to be entangled. Entanglement, which is a fully quantum mechanical phenomenon, describes situations where the systems exhibit quantum correlations such that we cannot describe one of them without referring to the others. In particular, photon-mediated interactions between semiconductor quantum dots allow the possibility of exciton entanglement, and we can take advantage of the non-separability of the whole system state for quantum information transferring between single spatially separated quantum dots. The quantification of entanglement is hence fundamental for applications in quantum technologies, but this is a very hard task for many-body systems and it is focus of intense research up to now [72, 73, 74]. We are nonetheless interested in a two-qubit system using two-level quantum dots, for which quantum entanglement has been widely studied [75, 76, 77, 78]. Here, we adopt the Peres-Horodecki negativity criterion, which leads to a sufficient condition for non-separability of composite systems in composite Hilbert spaces of dimension $2 \otimes 2$ and $2 \otimes 3$ [79, 80, 81]. Since our two-quantum-dot system is interacting with a photonic environment, the two-qubit reduced density operator ρ_{QD1QD2} of dimension $2 \otimes 2$, is calculated by tracing the whole density operator, ρ, over all photonic degrees of freedom of the system

$$\rho_{QD1QD2} = \mathrm{Tr}\,(\rho)_{ph}\,. \tag{88}$$

The negativity is defined as the absolute value of the sum of the negative eigenvalues of $\rho^{T_1}_{QD1QD2}$, where T_1 represents the partial transpose of ρ_{QD1QD2} with respect to the system 1, i.e., quantum dot 1. For example, consider a system of two quantum dots and one photonic mode, the matrix elements of the density operator in a Fock basis can be written as $\rho_{\alpha\mu m,\alpha'\mu'm'}$ where α and μ denote the excitation number, 0 or 1, in the two-level quantum dot 1 and 2, respectively, and m denotes the photon number, which is a positive integer, in the photonic mode of the system. Following Eq. (88), the matrix elements of the quantum dot reduced density operator, which will be denoted by σ, are given by

$$\sigma_{\alpha\mu,\alpha'\mu'} = \sum_m \rho_{\alpha\mu m,\alpha'\mu' m}, \tag{89}$$

and the matrix elements of the partial transpose of σ with respect to the quantum dot 1 read

$$\sigma^{T_1}_{\alpha\mu,\alpha'\mu'} = \sigma_{\alpha'\mu,\alpha\mu'}. \tag{90}$$

The negativity is therefore the absolute value of the sum of the negative eigenvalues of σ^{T_1}. Since the negativity is an entanglement monotone function for Hilbert spaces of dimension $2 \otimes 2$ and $2 \otimes 3$, it is a good measure of the entanglement degree in these composite spaces. For such a two-qubit system the negativity ranges from zero for a separable state up to the maximum value 0.5 for the maximally entangled Bell states. This can be easily shown by considering the Bell states written in the two-qubit basis as follows:

$$|\phi^{\pm}\rangle = \frac{1}{\sqrt{2}}(|00\rangle \pm |11\rangle) \tag{91}$$

$$|\psi^{\pm}\rangle = \frac{1}{\sqrt{2}}(|01\rangle \pm |10\rangle), \tag{92}$$

where the corresponding density operators are given by

$$\hat{\rho}_{\phi^{\pm}} = |\phi^{\pm}\rangle\langle\phi^{\pm}|, \qquad \hat{\rho}_{\psi^{\pm}} = |\psi^{\pm}\rangle\langle\phi^{\pm}|. \tag{93}$$

Considering the ordering of the basis $\{|00\rangle, |01\rangle, |10\rangle, |11\rangle\}$, the matrix representations of the density operators in Eq. (93) read

$$\rho_{\phi^{\pm}} = \frac{1}{2}\begin{pmatrix} 1 & 0 & 0 & \pm 1 \\ 0 & 0 & 0 & 0 \\ 0 & 0 & 0 & 0 \\ \pm 1 & 0 & 0 & 1 \end{pmatrix}, \quad \rho_{\psi^{\pm}} = \frac{1}{2}\begin{pmatrix} 0 & 0 & 0 & 0 \\ 0 & 1 & \pm 1 & 0 \\ 0 & \pm 1 & 1 & 0 \\ 0 & 0 & 0 & 0 \end{pmatrix}. \tag{94}$$

The matrix elements of ρ^{T_1}, namely, the partial transpose of ρ with respect to qubit 1, i.e., the first entry of $|\alpha_1\alpha_2\rangle$, are obtained from the matrix elements of ρ following the rule of Eq. (90)

$$\langle\alpha_1\alpha_2|\rho^{T_1}|\alpha_1'\alpha_2'\rangle = \langle\alpha_1'\alpha_2|\rho|\alpha_1\alpha_2'\rangle. \tag{95}$$

The matrix representations of $\rho^{T_1}_{\phi^{\pm}}$ and $\rho^{T_1}_{\psi^{\pm}}$ are then

$$\rho^{T_1}_{\phi^{\pm}} = \frac{1}{2}\begin{pmatrix} 1 & 0 & 0 & 0 \\ 0 & 0 & \pm 1 & 0 \\ 0 & \pm 1 & 0 & 0 \\ 0 & 0 & 0 & 1 \end{pmatrix}, \quad \rho^{T_1}_{\psi^{\pm}} = \frac{1}{2}\begin{pmatrix} 0 & 0 & 0 & \pm 1 \\ 0 & 1 & 0 & 0 \\ 0 & 0 & 1 & 0 \\ \pm 1 & 0 & 0 & 0 \end{pmatrix}. \tag{96}$$

Finally, it is easy to show that the characteristic equation to find the eigenvalues λ of the four matrices in Eq. (96) is

$$(0.5 - \lambda)^3 (0.5 + \lambda) = 0, \tag{97}$$

and their solutions are $\{0.5, 0.5, 0.5, -0.5\}$. The absolute value of the sum of the negative eigenvalues in Eq. (97), i.e, the negativity, is therefore 0.5. Thus, a negativity value of 0.5 determines an upper bound for the amount of entanglement in a two-qubit system.

3

RESULTS

The mutual interaction between two quantum dots decays rapidly when their distance is larger than the emission wavelength [67]. Proposals for increasing the mutual interaction distance between two quantum dots in a photonic crystal platform mainly considered using a waveguide as a bus for photon propagation [26, 27, 28]. The role of disorder on light localization was also addressed [29]. Alternatively, preliminary studies considered the mutual coupling between two quantum dots positioned at the field antinodes within the same photonic crystal cavity [26, 30], for which early experimental evidence was shown [24, 62, 31]. The possibility of mediating the inter-dot coupling through the normal modes of a photonic molecule has been considered for coupled micro disks [82]; nevertheless, the dot-dot distance is limited by evanescent inter-cavity coupling in free space. In this thesis, we theoretically address the possibility of using strongly coupled photonic molecules to efficiently increase the mutual dot-dot coupling rate even at large distances. A schematic representation of our system is shown in Fig. 14. We present original results on the inter-dot radiative coupling, disorder effects and steady state entanglement between the quantum dots.

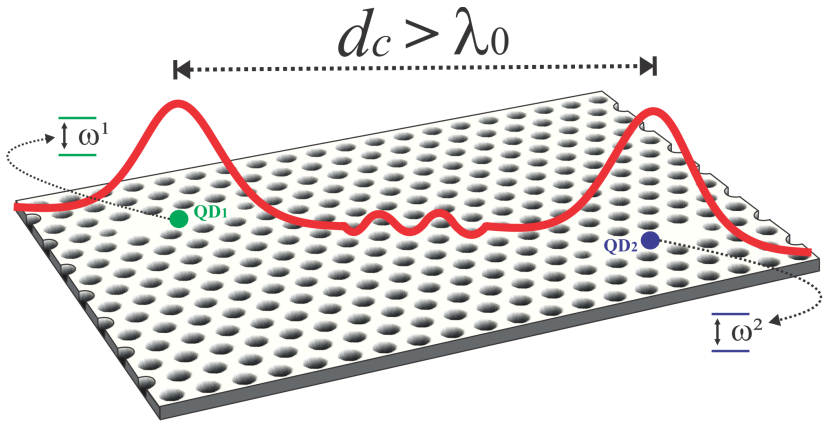

Figure 14: Schematic representation of the system investigated in this thesis: two strongly coupled photonic crystal nanocavities, each containing a single quantum dot. The distance between the nanocavities, d_c, can be larger than the characteristic quantum-dot-emission wavelength in vacuum, λ_0.

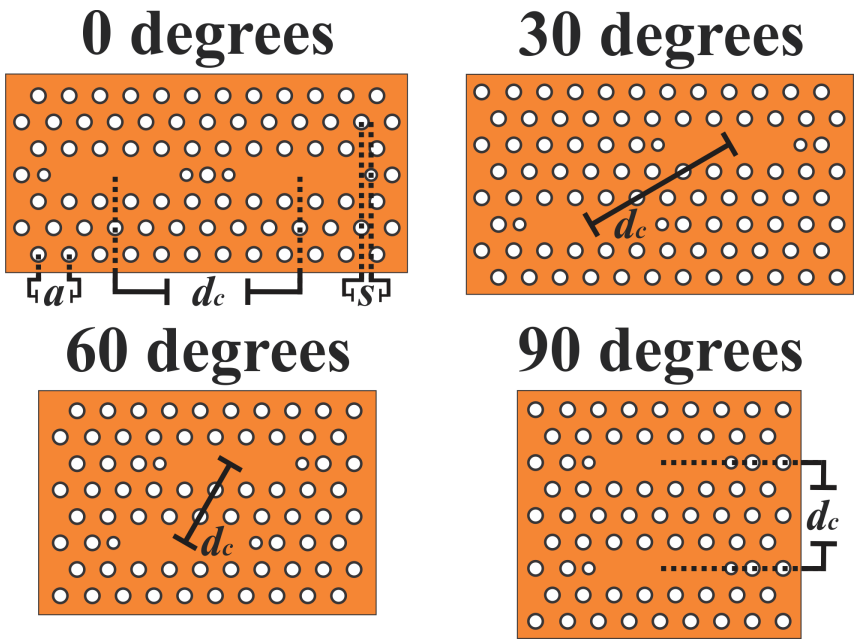

Figure 15: Schematic representation of the photonic crystal molecule considered in our work. Two L3 PC slab cavities in a hexagonal lattice of air holes are coupled along four different directions. We define a as the lattice parameter of the surrounding photonic crystal lattice, while s is the outward displacement of the end lateral holes of the cavities, and d_c is the center-to-center inter-cavity distance.

3.1 PHOTONIC CRYSTAL MOLECULE

The photonic crystal molecule that we study here is formed by two coupled nominally identical L3 cavities, i.e., photonic crystal dimer, in a two-dimensional photonic crystal slab of a hexagonal lattice of air holes in GaAs. In the photonic crystal community, the L3 cavity is commonly defined by three missing holes in a horizontal line of the photonic lattice [83, 84]; we choose the optimized design where the radius of the two end lateral holes are diminished to 80% of their original value, and the centers are outward displaced by $0.15a$, where a is the lattice parameter [85]. We focus on the four dimers where the line connecting the centers of the cavities determines an angle of 0°, 30°, 60° or 90° with respect to the horizontal axis, as it is schematically illustrated in Fig. 15. Typical values for GaAs photonic crystal structures coupled to InGaAs quantum dots in the 900 nm wavelength range are considered [30]: lattice parameter $a = 260$ nm, hole radius of 65 nm, slab thickness of 120 nm and refractive index of 3.41.

The photonic modes for the 0°, 30°, 60°, and 90° photonic crystal dimer are computed using the GME method of Sec. 2.1.4. We use a

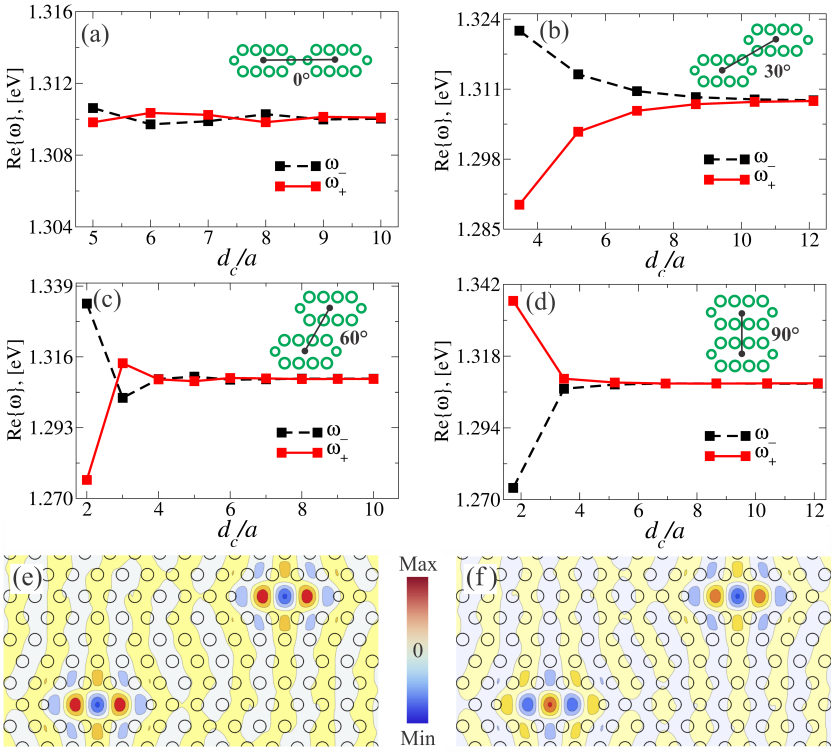

Figure 16: Photonic dispersion of the bonding (solid lines) and antibonding (dashed lines) modes for the (a) 0°, (b) 30°, (c) 60°, and (d) 90° cases, respectively. The lines only connect the individual points and serve as a guide for the eye. Electric field components E_y associated to the (e) bonding and (f) antibonding states for the 30° photonic crystal dimer at $d_c = 5\sqrt{3}a$.

hexagonal supercell[1] of superlattice parameter 24a, and up to 11025 total plane waves tested for convergence in the 30° and 60° cases; we use rectangular supercells of dimensions $27a \times 8\sqrt{3}a$ and $18a \times 25\sqrt{3}a$, and up to 11915 and 24829 total plane waves tested for convergence, in the 0° and 90° cases, respectively. Since the photonic structure has symmetry point, then Eq. (14) determines a real symmetric eigenvalue problem. Only one guided mode is used in the basis expansion, because the contribution of high order guided modes is negligible for the thickness considered here. Finally, the real part of the frequencies are averaged in the first Brillouin zone of the superlattice in order to smooth out finite supercell effects (see Appendix A).

Figure 16 shows the results of the GME computations for the first two photonic normal modes, associated to the split states arising from the fundamental L3 cavity mode. The bonding states are labeled with the subscript $+$, while the subscript $-$ is used for the antibonding

1 The supercell method is explained in Appendix A.

states. Panels (a), (b), (c), and (d) correspond to the 0°, 30°, 60° and 90° dimers, respectively. For the 0° case we see a very small splitting between the normal modes, which does not change appreciably with the inter-cavity distance d_c (defined from center-to-center of the two photonic crystal slab cavities). The behavior of the normal mode frequencies is quantitatively different for the other cases, in which a large splitting at small inter-cavity distances can be noticed. Such splitting decreases smoothly for the 30° dimer, and much more rapidly for the 60° and 90° dimers, on increasing d_c. Nevertheless, between $d_c = 4a$ and $d_c = 5a$ for the 60° case, and between $d_c = 7a$ and $d_c = 8a$ for the 0° case the splitting increases, which is a rather counterintuitive behavior and it typically occurs in photonic crystal molecules, as already evidenced [34, 41]. In addition, the bonding (+) and antibonding (−) behavior of the modes changes as a function of distance, which is another interesting phenomenon already seen in experimental measurements on such systems [41]. As it is expected, the resonance frequencies of these dimers tend to the values of the isolated L3 cavity for large distances. In Figs. 16(e) and 16(f) we show the E_y patterns for the bonding and antibonding states, respectively, for the case of 30° at the inter-cavity distance $d_c = 5\sqrt{3}a$. The symmetry point of the present photonic crystal molecule is located at the center of the structure. The bonding (antibonding) mode has an even (odd) symmetry with respect to this point, as it can be seen in the figure.

The imaginary parts of photonic eigenfrequencies are calculated using the photonic Fermi's golden rule of Eq. (29), and averaging in the first Brillouin zone of the superlattice, in the same way as it was done for the real parts; the corresponding quality factor is computed with these averaged quantities through Eq. (34), i.e., $Q = \langle \mathrm{Re}\{\omega\}\rangle / 2\langle \mathrm{Im}\{\omega\}\rangle$. Figures 17(a), 17(b), 17(c) and 17(d) show the quality factors of the split modes for the 0°, 30°, 60° and 90° cases, respectively. As a general trend, the quality factors are relatively small with respect to the quality factor of the fundamental L3 cavity mode for large splitting (dimers 30°, 60° and 90°), and increase quickly when d_c increases; they remain relatively constant for large inter-cavity distances and oscillate around this value. The 0° case is quantitatively different from the other dimers since the normal mode quality factors associated to this molecule evidence an enhancement with respect to the Q value of the fundamental L3 cavity mode, which is an interesting phenomenon already seen in photonic molecules [86]. The calculations shown in Figs. 16 and 17 agree with previous work on similar systems [34].

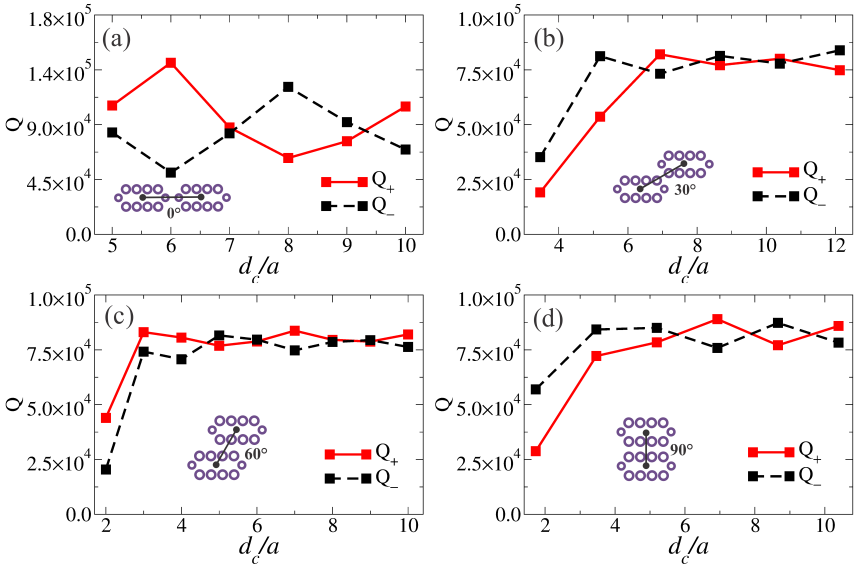

Figure 17: Quality factors Q for the (a) 0°, (b) 30°, (c) 60° and (d) 90° cases as a function of the inter-cavity distance, d_c. The lines only connect the individual points and serve as a guide for the eye.

3.2 LONG-DISTANCE RADIATIVE COUPLING BETWEEN QUANTUM DOTS

After characterizing the photonic eigenmodes of the photonic crystal dimer, we have all the parameters required to study the coupled quantum-dot photonic-dimer system. We consider each dot positioned at the center of each L3 cavity, which simplifies considerably the problem since the quantum dots only couple with the y component of the electric field. This is due to the fact that the x field component is negligible for small inter-cavity distances d_c at the center of each L3 cavity, and eventually tends to zero for large d_c values (the E_x is exactly zero at the center of the isolated L3 cavity). We also consider that the loss rates through the photonic normal modes, $\gamma_m = 2\mathrm{Im}\{\omega_m\}$, are significantly larger than the quantum dot loss rates $\gamma^{(\alpha)}$ through other channels, therefore, we set $\gamma^{(\alpha)} = 0$. With these conditions the Λ matrix of Eq. (63) takes the following simplified form:

$$\Lambda_y = \begin{pmatrix} \omega^{(1)} & 0 & g^1_{1,y} & g^1_{2,y} \\ 0 & \omega^{(2)} & g^2_{1,y} & g^2_{2,y} \\ g^{1*}_{1,y} & g^{2*}_{1,y} & \omega_1 - i\frac{\gamma_1}{2} & 0 \\ g^{1*}_{2,y} & g^{2*}_{2,y} & 0 & \omega_2 - i\frac{\gamma_2}{2} \end{pmatrix}, \tag{98}$$

where $\omega^{(1)} = \omega^{(1)}_y$, $\omega^{(2)} = \omega^{(2)}_y$, $\omega_1 = \min(\omega_+, \omega_-)$ and $\omega_2 = \max(\omega_+, \omega_-)$. In Fig. 18(a) we show the real part of the eigenfrequencies from diagonalization of the matrix in Eq. (98), for the same

dimer configuration shown in Figs. 16(e) and 16(f), as a function of the frequencies of the two quantum dots at zero dot-dot detuning. We see that vacuum Rabi splitting occurs in the frequency regions associated to the coupled modes resonances (the vertical dashed lines), which is the signature of the strong coupling between the excitonic states and the photonic crystal modes. Due to the opposite symmetry of the two photonic modes, i.e. symmetric (bonding) and antisymmetric (antibonding), the relevant excitonic states are the ones with the symmetry of the dimer mode. In this way, the first anti-crossing, which is associated to the bonding normal mode, corresponds to an excitonic symmetric state and the antisymmetric remains dark, while the second anti-crossing, which is associated to the antibonding normal mode, corresponds to an excitonic antisymmetric state with the symmetric one remaining dark. When the first photonic mode is antibonding, as in the case of some configurations of the 0°, 60° and 90° dimers, the first anti-crossing corresponds to an antisymmetric excitonic state, and the second one to a symmetric excitonic state, as verified in our calculations. The Hopfield coefficients are shown in Fig. 18(b), where an interesting collective behavior is seen. In the region of the first strong coupling the polaritons 1 and 3 have comparably significant values of the coefficients λ_y^1 (quantum dot 1), λ_y^2 (quantum dot 2), and λ_1 (mode 1), and we see the same behavior for polaritons 2 and 4 in the region of the second strong coupling, but now with the mode coefficient λ_2 (mode 2), which corresponds to the antisymmetric mode. Usually, it is very likely that two quantum dots are detuned due to their inhomogeneous distribution of sizes. Therefore, we show in Figs. 18(c) and 18(d) the same analysis made in panels (a) and (b) but now introducing a finite and sizable detuning between the two dots $\Delta = \hbar\omega^{(1)} - \hbar\omega^{(2)} = 300$ μeV. We see that under such conditions, symmetric and antisymmetric excitonic states are possible and the dark mode is not present. All the Hopfield coefficients associated to the coupling of the dots with each photonic mode are non-negligible, and consequently radiative coupling between the quantum dots remains present.

We now try to give an answer to the question of how the radiative coupling depends on the inter-cavity distance in a photonic crystal dimer. The radiative coupling between the quantum dots is quantified by the tensor components of Eq. (68), which are proportional to the Green's function evaluated at the dot positions. The dominant component of the Green's tensor in our case is the yy due to the dominant polarization of the normal modes in the y direction, and to the small value of the x electric field component at the center of the $L3$ cavities, which is identically zero for the fundamental isolated-$L3$ cavity mode. Therefore, considering the two dimer modes with y electric field components, $E_{1,y}$ and $E_{2,y}$, frequencies ω_1 and ω_2, and associ-

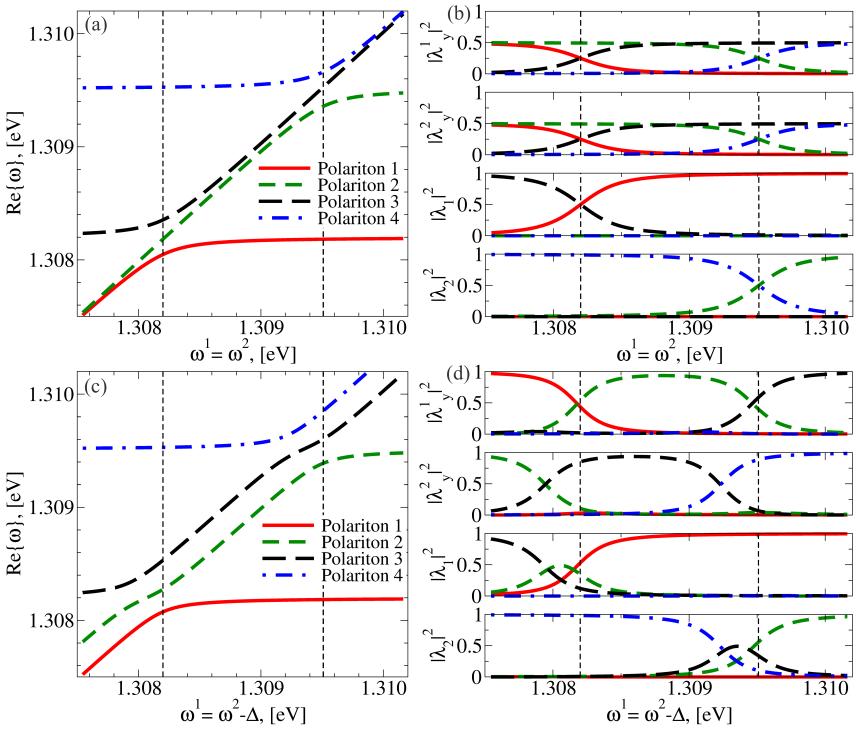

Figure 18: (a) Real part of the eigenfrequencies of the quantum-dot photonic-dimer system for the 30° case at $d_c = 5\sqrt{3}a$, for zero dot-dot detuning. (b) The square modulus of the Hopfield coefficients associated to (a). (c) and (d) correspond to the same case as in (a) and (b), respectively, but with a finite dot-dot detuning of $\Delta = 300$ μeV. In panels (b) and (d), λ_y^1 and λ_y^2 are associated to the quantum dots 1 and 2, respectively, and λ_1 and λ_2 are associated to the photonic crystal modes with frequencies ω_1 and ω_2, respectively.

ated loss rates $\gamma_1 = \omega_1/Q_1$ and $\gamma_2 = \omega_2/Q_2$, the effective radiative coupling between the two quantum dots positioned at the centers of the cavities, i.e., $\mathbf{r}_1$ and $\mathbf{r}_2$, at the excitonic transition frequency ω, can be reduced to the following formal expression [33]:

$$G_{yy}^{12}(\omega) = \frac{2\pi\omega d^2}{\hbar}\left(\frac{E_{1,y}(\mathbf{r}_1)E_{1,y}^*(\mathbf{r}_2)}{\omega_1 - i\frac{\gamma_1}{2} - \omega} + \frac{E_{2,y}(\mathbf{r}_1)E_{2,y}^*(\mathbf{r}_2)}{\omega_2 - i\frac{\gamma_2}{2} - \omega}\right), \quad (99)$$

We plot the absolute value of this function, evaluated at the two dimer eigenfrequencies, in Fig. 19 as a function of the inter-cavity distance, where panels (a), (b), (c) and (d) correspond to the 0°, 30°, 60° and 90° cases, respectively. These results evidence that the radiative coupling is highly enhanced at resonance with the dimer modes and the effective energy transfer between the quantum dots can achieve values of the order of 2.5 meV for the 0° case, and 1.5 meV for the 30°, 60° and 90° cases, which are at least an order of magnitude larger than typical values achieved in one-dimensional systems [26, 87]. However, for the 30°, 60° and 90° dimers the dot-dot coupling strength at resonance is surprisingly minimal at small inter-cavity distance, which

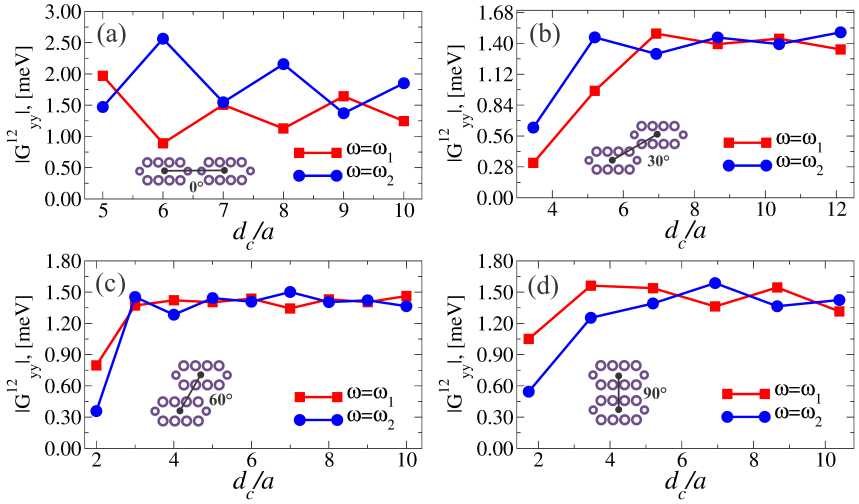

Figure 19: Absolute value of the component $G^{12}_{yy}(\omega)$ evaluated at $\omega = \omega_1$ and $\omega = \omega_2$ as a function of the inter-dot distance, for the (a) 0°, (b) 30°, (c) 60° and (d) 90° dimers. The lines only connect the individual points and serve as a guide for the eye.

are the cases where the coupling between the cavity modes is largest. As a counterintuitive consequence, the coupling strength between the dots increases with the interdot distance after the smallest values of d_c, and remains relatively constant (small oscillations) at larger values of d_c. It is important to remind that these results, which allow the possibility of sizable long-distance interaction between quantum dots, are valid as long as the normal mode splitting exceeds the photonic radiative linewidth, i.e., where the mode splitting can be spectrally resolved (strong cavity-cavity coupling condition).

These interesting behaviors can be interpreted by analyzing the expression for the coupling constant $G^{12}_{yy}(\omega)$ in Eq. (99). Since the fields are strongly localized in both cavity regions for all inter-cavity distances in the strong cavity-cavity coupling regime, the functions $E_y(\mathbf{r}_\alpha)$ depend very weakly on the d_c parameter; furthermore, the functions $E_{1,y}(\mathbf{r}_1)E^*_{1,y}(\mathbf{r}_2)$ and $E_{2,y}(\mathbf{r}_1)E^*_{2,y}(\mathbf{r}_2)$ are real due to the point symmetry of the structure with respect to the origin of coordinates, and have approximately the same value with opposite signs due to the opposite symmetries of the two modes [see Figs. 16(e) and 16(f)]. In this way, we can approximate the $|G^{12}_{yy}(\omega)|$ function as:

$$|G^{12}_{yy}(\omega)| \approx \frac{2\pi d^2 |g^{12}|}{\hbar}\omega \left| \frac{\Delta_m - i\frac{\gamma_2-\gamma_1}{2}}{(\omega_1 - i\frac{\gamma_1}{2} - \omega)(\omega_2 - i\frac{\gamma_2}{2} - \omega)} \right|, \quad (100)$$

where $|g^{12}| = |E_{1,y}(\mathbf{r}_1)E^*_{1,y}(\mathbf{r}_2)| \approx |E_{2,y}(\mathbf{r}_1)E^*_{2,y}(\mathbf{r}_2)|$, and $\Delta_m = \omega_2 - \omega_1$. Neglecting the γ terms when they do not contribute significantly

to the sums, as well as their second order terms, we obtain the following trends for the effective coupling constant:

$$|G^{12}_{yy}(\omega_i)| \propto Q_i\,, \qquad \text{for} \quad i = 1, 2, \tag{101}$$

which qualitatively explains the results of Fig. 19. The key assumption in Eq. (101) lies in the fact that the normal modes of a photonic molecule are strongly localized in the cavity regions, and such field distributions are weakly dependent on the inter-cavity distance. This leads to a dependence of the radiative coupling on the inverse of the loss rates only [see Eq. (99)], which are inversely proportional to the quality factors.

3.3 DISORDER EFFECTS ON THE RADIATIVE COUPLING BETWEEN QUANTUM DOTS

Usually, quantum dots are not perfectly positioned at the center of the cavities due to the precision limitation in modern sample fabrication techniques. In this way, we studied how the results shown in Fig. 19 are affected by considering disorder in the dot positioning. To accomplish this, the position of one quantum dot is generated by a random distribution with Gaussian probability of given variance σ; since the inter-dot distance is kept fixed, the position of the other quantum dot is automatically determined, which models in a realistic way possible misalignments between the photonic pattern and the dots. Fig. 20 shows the results of this analysis for the 0°, 30°, 60° and 90° cases in panels (a), (b), (c) and (d), respectively, where the dimers are assumed in resonance with the lowest frequency normal mode ω_1. The radiative coupling was averaged over 1000 realizations for each of the variances considered, and the statistical standard error is shown in the error bars of the curves[2]. Our numerical calculations show that when the variance is of the order of the precision achieved in modern fabrication techniques, which is around 20 nm [88], the effective radiative coupling between the quantum dots at resonance with the photonic normal mode remains quite sizable, i.e., on the order of 1.5 meV for the 0° dimer and 1.2 meV for the 30°, 60° and 90° dimers. We verified that the results in which the dots are in resonance with the second normal mode of frequency ω_2 are equivalent, and the effective coupling strengths remain of the same order of magnitude for each dimer.

We have also studied the question of how the radiative coupling between the two distant quantum dots is modified by considering structural disorder in the photonic crystal dimer. Usually the predicted losses of perfectly arranged photonic structures (intrinsic losses) are

2 The standard error is defined as the corrected standard deviation over the square root of the number of realizations.

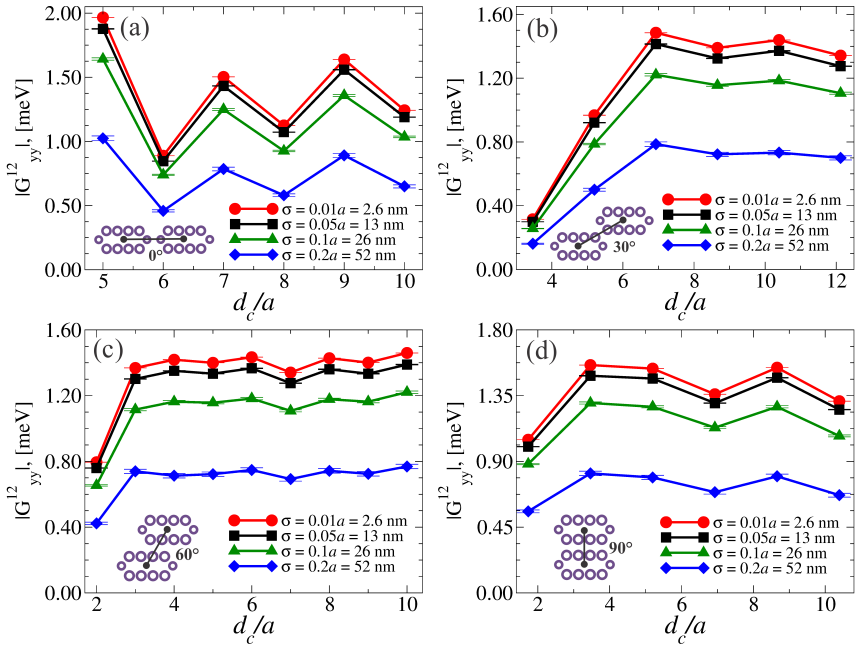

Figure 20: Radiative effective coupling between the quantum dots at $\omega = \omega_1$ for the statistical analysis of their non ideal position. Panels (a), (b), (c) and (d) correspond to the 0°, 30°, 60° and 90° dimers. The coupling strength is averaged over 1000 realizations and the standard error is shown in the error bars. The lines only connect the individual points and serve as a guide for the eye.

much smaller than the value measured in the fabricated sample; this is mainly due to small errors in the fabrication process, which deviates the holes of the structure (in an photonic crystal slab of circular holes) from their ideal position, shape and size, producing extra channels of losses in the photonic structure (extrinsic diffraction losses). Here, we consider the fluctuations of the hole radii as the principal disorder contribution to the extrinsic diffraction losses. In our model of disorder we generate the hole radii randomly in the supercell with Gaussian probability, centered at 65 nm with standard deviation σ_S. As a natural consequence of Eq. (101), we expect the decreasing of G^{12}_{yy} as long as σ_S increases (losses are larger and consequently the quality factors are smaller). Nevertheless, the effect of disorder in photonic molecules does not only increase the losses of the system; since the random fluctuations of the radii have the effect of modifying independently the resonant frequencies of the cavities, the normal modes of the system (dressed states) are turned into the cavity modes (bared cavity states) if the magnitude of the structural disorder, which can be quantified by σ_S, is much larger than the cavity-cavity coupling constant $J_\lambda = \Delta\lambda/2$, where $\Delta\lambda$ is the wavelength normal mode splitting at zero disorder if J_λ is not strongly modified by the random fluctuations [89]. The consequence of this

"normal mode breaking" is the decreasing of the field products in each of the two terms of G^{12}_{yy} [see Eq. (99)], since the field is more localized in only one of the two cavities for large values of σ_S. Therefore, the effective energy transfer between the two quantum dots is reduced by two independent contributions when structural disorder is considered: disorder-induced losses and normal mode breaking of the photonic dimer. Figure 21 shows the results of the absolute value of G^{12}_{yy} in resonance with the fundamental and first excited normal mode, at $d_c = 7a$, $d_c = 5\sqrt{3}a$, $d_c = 5a$ and $d_c = 3\sqrt{3}a$ for the 0°, 30°, 60° and 90° dimers, respectively, in the corresponding (a), (b), (c) and (d) panels. The G^{12}_{yy} component has been averaged over 30 disorder realizations and the standard error is shown in the error bars. The values of σ_S considered here are of the same order of the J_λ constants in the associated configurations, which are equal to 0.119 nm, 0.450 nm, 0.475 nm and 0.263 nm for the 0°, 30°, 60° and 90° cases, respectively. As it is expected, the effective coupling strength between the quantum dots decreases when the disorder parameter σ_S increases. From Figs. 20 and 21, we can see also that the effect of the structural disorder on decreasing the energy transfer between the dots is much stronger than the effect of their non-ideal positioning; the $|G^{12}_{yy}|$ component decreases by ~ 0.5 meV in a very narrow range of σ_S (~ 1 nm, as seen in Fig. 21), while the same ~ 0.5 meV decreasing is seen over a quite larger range when calculated as a function of σ (~ 30 nm, as seen in Fig. 20). Nevertheless, our results show that values of σ_S which are of the order of J_λ not affect strongly the effective dot-dot coupling and $|G^{12}_{yy}|$ remains of the same order of magnitude, i.e., disorder magnitudes which are of the order of 0.5 nm (0.0019a), 1.5 nm (0.0058a), 1.6 nm (0.0061a) and 0.9 nm (0.0035a) for the 0°, 30°, 60° and 90° dimers, respectively, do not affect appreciably the radiative coupling. Larger values of the structural disorder magnitude are shown in the corresponding insets of Fig. 21, where we have considered σ_S up to 5 nm. The radiative coupling is strongly reduced when very disordered systems are taken into account, and the effective coupling strength between the quantum dots can be reduced up to an order of magnitude. However, values around 4 nm (0.015a), relevant for the state of the art fabrication tolerances in GaAs or InGaAs structures, determine an effective energy transfer of ~ 250 μeV between the dots, which is still an order or magnitude larger than the effective strengths obtained in previous disordered systems [29], and two times larger than our dot-field coupling strengths (~ 110 μeV). We have obtained equivalent results for the other inter-dot distances in all dimer's configurations.

Finally, in the present semiclassical study we have considered resonant coupling between the dots and the photonic normal modes of the photonic molecule. Nevertheless, the excitonic frequencies of typ-

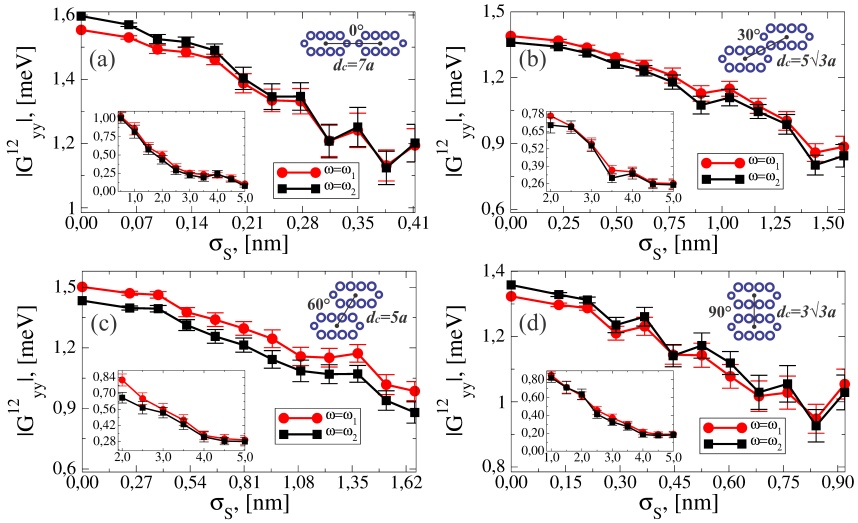

Figure 21: Radiative effective coupling between the quantum dots as a function of the standard deviation σ_S, which quantifies the structural disorder in the photonic crystal dimer. Panel (a) corresponds to the 0° dimer at $d_c = 7a$, panel (b) to the 30° dimer at $d_c = 5\sqrt{3}a$, panel (c) to the 60° dimer at $d_c = 5a$ and panel (b) to the 90° dimer at $d_c = 3\sqrt{3}a$. Insets show the results for larger values of σ_S. The coupling strength is averaged over 30 disorder realizations and the standard error is shown in the error bars. The lines only connect the individual points and serve as a guide for the eye.

ical semiconductor quantum dots are inhomogeneously distributed with a width of several meV. This effect can be modeled as another disorder contribution on the excitonic transition frequencies of the dots; such a study will be carried out in a future work. Nevertheless, we expect a strong reduction of the radiative coupling strengths if the non-resonant condition determines a dot-dot detuning which is much larger than the linewidth of the corresponding photonic normal mode. An efficient experimental setup for tuning the quantum dot transition frequencies using the quantum confined Stark effect, and bring them into resonance, is implemented in Refs. [24, 90].

Since structural disorder breaks the symmetry of the photonic crystal, the eigenvalue problem of Eq. (14) becomes complex hermitian and computationally expensive. Therefore, the statistical analysis of $|G^{12}_{yy}|$ as a function of σ_S shown in Fig. 21, was carried out using rectangular smaller supercells of dimensions $21a \times 6\sqrt{3}a$ with 6951 plane waves, $20a \times 7\sqrt{3}a$ with 7727 plane waves, $17a \times /8\sqrt{3}a$ with 7489 plane waves and $14a \times 11\sqrt{3}a$ with 8497 plane waves, tested for convergence, the 0°, 30°, 60° and 90° dimers, respectively. Here, we also considered only one guided mode in the expansion because we are interested in the frequency region below the second-order mode of the homogeneous slab.

3.4 LONG-RANGE ENTANGLEMENT BETWEEN RADIATIVELY COUPLED QUANTUM DOTS

We have studied the resonant energy transfer between two distant quantum dots in photonic crystal dimers using a semiclassical approach based on the photonic Green's function, giving rise to an effective dot-dot long-distance radiative coupling which can be of the order of 1 meV. Here, using the fully quantum mechanical formalism presented in Sec. 2.3.2, we focus on the role of the normal modes as channels for entanglement between the quantum dots, as well as the necessary conditions for entanglement generation in photonic crystal dimers. In order to describe the two-level-dot photonic-dimer system we consider the second-quantized effective driven Hamiltonian of Eq. (77), written in the normal mode basis:

$$\begin{aligned}\hat{H}_{eff} = \sum_{n=1}^{2} \hbar\bar{\omega}_n \hat{a}_n^\dagger \hat{a}_n + \sum_{\alpha=1}^{2} \hbar\bar{\omega}^{(\alpha)} \hat{b}_\alpha^\dagger \hat{b}_\alpha \\ + \hbar \sum_{n,\alpha=1}^{2} \left(g_n^{*\alpha} \hat{a}_n^\dagger \hat{b}_\alpha + g_n^\alpha \hat{a}_n \hat{b}_\alpha^\dagger \right) \\ + \hbar \sum_{\alpha=1}^{2} \left(\Omega_\alpha e^{i\phi_\alpha} \hat{b}_\alpha^\dagger + \Omega_\alpha^* e^{-i\phi_\alpha} \hat{b}_\alpha \right),\end{aligned} \tag{102}$$

where $\bar{\omega}_n = \omega_n - \omega_p$ and $\bar{\omega}^{(\alpha)} = \omega^{(\alpha)} - \omega_p$. In Eq. (102), ω_n and $\omega^{(\alpha)}$ correspond to the frequency of the normal mode n (given by GME) and the excitonic transition frequency of the two-level quantum dot α, respectively; $\hat{a}_n^\dagger$ ($\hat{a}_n$) is the creation (destruction) operator of photons in the normal mode n; $\hat{b}_\alpha^\dagger$ ($\hat{b}_\alpha$) is the creation (destruction) operator of one electron-hole pair in the dot α; g_n^α are the coupling strengths between normal mode n and quantum dot α; and Ω_n is the pumping rate, with phase ϕ_α, at which are coherently created electron-hole pairs in the dot α by a continuous wave pump laser or electric potential with frequency ω_p. We assume the two quantum dots at the centers of the dimer cavities and optimal dipole orientation (parallel to the electric field); over these conditions the coupling strength of Eq. (72) is given by

$$g_n^\alpha = \sqrt{\frac{2\pi\omega_0 d^2}{\hbar}} E_{y,n}(\mathbf{r}_\alpha), \tag{103}$$

where ω_0 and d^2 are the average exciton transition frequency and the square dipole moment which are in the range of ~ 1.3 eV and ~ 0.51 eV nm^3, respectively, for typical self-organized InGaAs quantum dots, and $E_{y,n}(\mathbf{r}_\alpha)$ is the non-vanishing electric field component at the center of the dimer cavities, which is calculated with GME. The

master equation Eq. (78), for describing the losses of the system, reads

$$\frac{d\tilde{\rho}}{dt} = \frac{i}{\hbar}\left[\tilde{\rho}, \hat{H}_{eff}\right] + \sum_{n=1}^{2} \hat{\mathcal{L}}(\gamma_n) + \sum_{\alpha=1}^{2} \hat{\mathcal{L}}(\gamma^{(\alpha)}), \tag{104}$$

where

$$\begin{aligned}
\hat{\mathcal{L}}(\gamma_1) &= \gamma_1 \left(\hat{a}_1 \tilde{\rho} \hat{a}_1^\dagger - \hat{a}_1^\dagger \hat{a}_1 \tilde{\rho}/2 - \tilde{\rho} \hat{a}_1^\dagger \hat{a}_1/2\right) \\
\hat{\mathcal{L}}(\gamma_2) &= \gamma_2 \left(\hat{a}_2 \tilde{\rho} \hat{a}_2^\dagger - \hat{a}_2^\dagger \hat{a}_2 \tilde{\rho}/2 - \tilde{\rho} \hat{a}_2^\dagger \hat{a}_2/2\right) \\
\hat{\mathcal{L}}(\gamma^{(1)}) &= \gamma^{(1)} \left(\hat{b}_1 \tilde{\rho} \hat{b}_1^\dagger - \hat{b}_1^\dagger \hat{b}_1 \tilde{\rho}/2 - \tilde{\rho} \hat{b}_1^\dagger \hat{b}_1/2\right) \\
\hat{\mathcal{L}}(\gamma^{(2)}) &= \gamma^{(2)} \left(\hat{b}_2 \tilde{\rho} \hat{b}_2^\dagger - \hat{b}_2^\dagger \hat{b}_2 \tilde{\rho}/2 - \tilde{\rho} \hat{b}_2^\dagger \hat{b}_2/2\right)
\end{aligned} \tag{105}$$

The normal mode losses of Eq. (105) are given by the photonic Fermi's golden rule within the GME approximation, i.e., $\gamma_n = 2\mathrm{Im}\{\omega_n\}$, and the exciton decay rates $\gamma^{(\alpha)}$ are free parameters in our model. The master equation of Eq. (104) depends on the interdot distance via the g_n^α, ω_n and γ_n parameters, which are implicit functions of the cavity-cavity separation, and it is numerically implemented by expressing the operators on a occupation number Fock basis, truncated to the most suitable photon number prior checked for convergence.

After defining the key parameters of our quantum model, we begin by characterizing the photonic normal modes as channels for quantum entanglement in the steady state. For determining the state with maximum entanglement we define the phase difference between the pumpings $\phi = \phi_1 - \phi_2$ and we write the pumping frequency as $\omega_p = \omega_1 + \delta$ with $\Omega_\alpha = \Omega_0$ (same pumping rates for both dots). Considering the two quantum dots resonant with the lower frequency normal mode, i.e., $\omega^{(1)} = \omega^{(2)} = \omega_1$, and using the calculated GME parameters we compute the negativity by solving the master equation for the steady state density matrix as a function of ϕ and δ, with $\phi_2 = 0$. Figure 22 shows the results for the 30° dimer at $d_c = 2\sqrt{3}a = 901$ nm, where the vertical black and white dashed lines correspond to the dark state and polariton branches of the system, respectively. The largest entanglement, corresponding to a negativity of 0.103 or ~ 20% of the maximum (see Sec. 2.3.2.1), is seen at the dark state with a phase difference of π. Since the excitonic dark state does not couple effectively to the photonic mode due to their opposite symmetry, the former remains "protected" from the dissipative effects of the latter, allowing the non-zero steady state negativity seen in the figure. The phase difference between the pumpings is determined by the bonding (symmetric) or antibonding (antisymmetric) behavior of the normal mode; for bonding modes the optimal phase difference will be $(2m+1)\pi$ (antisymmetric excitonic dark state) while for antibonding modes will be $2m\pi$ (symmetric excitonic dark state), with m

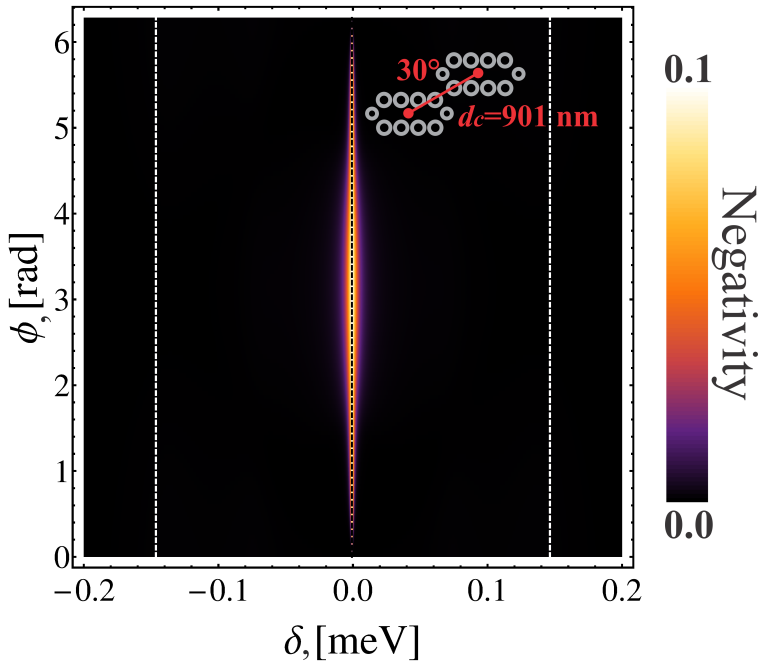

Figure 22: Steady state negativity for the 30° dimer at $d_c = 2\sqrt{3}a = 901$ nm as a function of the phase difference between the pumpings $\phi = \phi_1 - \phi_2$, with $\phi_2 = 0$, and the frequency shift δ, where $\omega_p = \omega_1 + \delta$. The maximum negativity is 0.103. The two quantum dots are in resonance with the lower frequency normal mode and we have considered $\gamma^{(\alpha)} = 0$ and $\hbar\Omega_0 = 1$ μeV.

integer. In the calculations of Fig. 22 we have considered $\gamma^{(\alpha)} = 0$ and $\hbar\Omega_0 = 1$ μeV; since $\hbar\gamma_n$ is between 10 and 60 μeV and $\hbar g_n^{\alpha} \sim 110$ μeV for all dimers, we are in the weak pumping regime and the basis used for solving the master equation $|\alpha_1\alpha_2 n_1 n_2>$, with α_i the excitation number (0 or 1) in the dot i and n_i the number of photons in the mode i, is safely truncated at $n_i = 1$. We have obtained equivalent results for all dimer configurations at all intercavity distances allowed by the corresponding supercell.

Taking into account that the largest steady state negativity corresponds to the dark state, at the phase difference determined by the photonic mode in resonance with the quantum dots, we now investigate how the entanglement depends on the dot-dot separation d_c. Figure 23 shows the negativity results as a function of the interdot distance, for the 0°, 30°, 60° and 90° dimers, considering $\hbar\gamma^{(\alpha)} = 0$ μeV, black circles, $\hbar\gamma^{(\alpha)} = 0.66$ μeV, red squares, $\hbar\gamma^{(\alpha)} = 3.3$ μeV, blue triangles, and $\hbar\gamma^{(\alpha)} = 6.6$ μeV, green diamonds. The quantum dots are in resonance with the lower frequency normal mode and $\hbar\Omega_0 = 1$ μeV as in Fig 22. We identify a negativity decreasing as a function of the interdot distance in the large d_c region for all dimers, which suggests a proportional dependence of the entanglement on the nor-

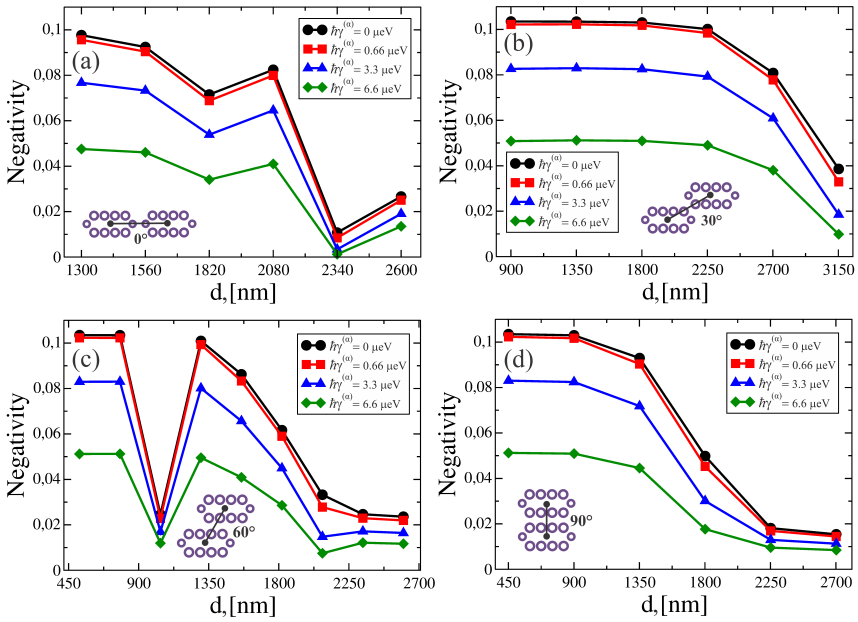

Figure 23: Steady state negativity for the dimers 0°, in (a), 30°, in (b), 60°, in (c), and 90°, in (d), as a function of the distance between the quantum dots d_c considering $\hbar\gamma^{(\alpha)} = 0$ μeV, black circles, $\hbar\gamma^{(\alpha)} = 0.66$ μeV, red squares, $\hbar\gamma^{(\alpha)} = 3.3$ μeV, blue triangles, and $\hbar\gamma^{(\alpha)} = 6.6$ μeV. The two quantum dots are in resonance with the lower frequency normal mode and $\hbar\Omega_0 = 1$ μeV. The lines connecting the individual points only serve as a guide for the eye.

mal mode splitting. The latter is a decreasing-monotone function for large intercavity distances and non-monotonic for intermediated values of d_c; in fact, the splitting can increase for increasing intercavity distance at specific dimer configurations (see Fig. 16). Such a phenomenon is clearly reflected in the negativity, i.e., the entanglement increases for increasing d_c, into the d_c intervals $[1820, 2080]$ nm and $[2340, 2600]$ nm for panel (a), and $[1040, 1300]$ nm for panel (c); in these cases, the normal mode splitting changes from a very small value to a large value, with respect to the linewidths of the photonic modes. At the other intermediated values of the interdot distances, the negativity is roughly of the order of ~ 0.1. Hence, the results of Fig 23 show that when the normal mode splitting is well defined (quite larger than the photonic linewidths), the negativity remains of the order of ~ 0.1. The 30° dimer, in panel (b), clearly evidences such a behavior; the negativity is a very flat function, around 0.1, up to $d_c = 2252$ nm, where the mode splitting is much greater than the normal mode linewidths. For larger values of d_c, the splitting becomes of the order of γ_n and the negativity decreases. The 90° dimer, in panel (d), is characterized by its rapidly splitting decreasing where d_c increases, consequently, significant values of negativity

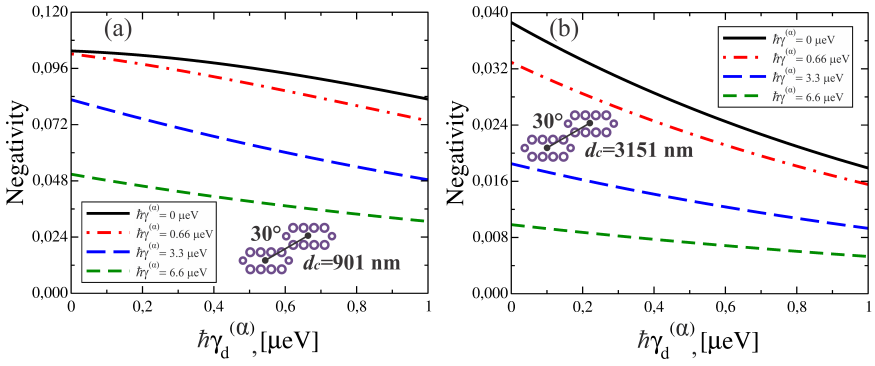

Figure 24: Steady state negativity for the 30° dimer at $d_c = 2\sqrt{3}a = 901$ nm, panel (a), and $d_c = 7\sqrt{3}a = 3151$ nm, panel (b), as a function of the pure dephasing rate $\gamma_d^{(\alpha)} = \gamma_d^{(1)} = \gamma_d^{(2)}$, for different exciton loss rates. The two quantum dots are in resonance with the lower frequency normal mode, i.e., $\omega^{(1)} = \omega^{(2)} = \omega_1$, and the pumping rate is $\hbar\Omega_0 = 1$ μeV.

are not supported at interdot distances which are larger than the characteristic wavelength of the system. Furthermore, it is very interesting that the entanglement is not strongly affected by the γ_n rates as long as the normal mode splitting is well defined; along the flat region of the 30° dimer, $\hbar\gamma_1$ and $\hbar\gamma_2$ change from 67 μeV and 37 μeV, to 17 μeV and 16 μeV, respectively, when d_c changes, correspondingly, from 901 nm to 2252 nm. In Sec. 3.2, we showed that the resonant energy transfer between radiatively-coupled quantum dots depends on the quality factor of the normal mode in resonance with the dots, i.e., Eq. (101), where the 0° configuration is the most convenient in terms of energy transfer, due to its very-high normal mode quality factors (see Fig. 17). Here, we show that when the figure of merit is long-range entanglement, the 30° dimer is the best choice due to its well defined normal mode splitting even for distances larger than the characteristic wavelength of the system. Results of Fig. 23 also evidence that the entanglement of the dark state is not strongly modified when losses of typical self-organized InGaAs quantum dots are taken into account; state-of-art InGaAs-dot excitonic lifetimes are between the triangle-blue and square-red curves [88, 91, 92], i.e., between 0.2 ns and 1 ns.

As a further loss channel, semiconductor quantum dots are known to be subject to pure dephasing [24, 93]. To complete the study on the dependence of entanglement on the main system losses, in Fig. 24 we investigate the dependence of the steady state negativity on their pure dephasing rates by adding the term of Eq. (81) to the Master equation of Eq. (104). Results are reported for the 30° dimer at two different interdot distances in panels (a) and (b), and considering the same values of $\gamma^{(m)}$ rates as in the previous Figure. The steady state

entanglement is not strongly affected by viable experimental pure dephasing rates [94]. In panel (a), where the normal mode splitting is much larger than the photonic linewidth, the negativity is decreased to 82% for $\hbar\gamma^{(m)} = 0$ μeV at $\hbar\gamma_d^{(m)} = 1$ μeV and to ~ 70% for state-of-art InGaAs quantum dot excitonic lifetimes. For very large intercavity distances, where the splitting is of the order of the normal mode linewidth, the entanglement is more sensible and it is decreased to ~ 50% at $\hbar\gamma_d^{(m)} = 1$ μeV for realistic InGaAs dots. Since we are interested in the strong cavity-cavity coupling regime, i.e., well defined normal mode splitting, and low-loss quantum dot excitonic states, we will safely consider $\gamma_d^{(m)} = 0$ from now on. Equivalent results were obtained for entanglement as a function of the pure dephasing rates in the 0°, 60° and 90° dimers.

Since quantum dots are very likely to be detuned due to their inhomogeneous distribution of sizes, we also studied the effect of detuning, between the excitonic transition frequencies, on the entanglement. Figure 25 shows the results of this study for the 30° dimer, at the minimum and maximum interdot distances, panel (a) and (b), respectively. The same exciton loss rates of Fig 23 were considered here, but neglecting pure dephasing. The entanglement is a very sensible function of the dot-dot energy detuning, in fact, for $\Delta = 10$ μeV the negativity drops from 20% ($\Delta = 0$) to 5%, in panel (a), and from 8% ($\Delta = 0$) to 3%, in panel (b). The presence of the second normal mode at large intercavity distances produces the softer decreasing in the curves of panel (b) in relation with the corresponding curves in panel (a). Radiative coupling between the quantum dots through a photonic mode is possible as long as the non-resonant condition determines a dot-dot detuning smaller than the linewidth of the mode; nevertheless, Fig. 25 evidences that the condition for entanglement between radiatively-coupled quantum dots is more stringent. In panel (a), the line width of the photonic normal mode is 67 μeV, however, the negativity is near to zero for detuning values larger than 40 μeV, where the radiative coupling is still present between the dots. In this way, the entanglement is more conditioned by the linewidth of the excitonic states of the dots than by the linewidth of the photonic mode, i.e., the entanglement is sizable when the dot-dot detuning is smaller than the exciton linewidth. We have obtained equivalent results for the 0°, 60° and 90° dimers.

We have shown that it is possible to obtain 20% of the maximum entanglement between two radiatively-coupled quantum dots, in the steady state regime, for interdot separations that can be larger than the characteristic wavelength of the system. However, practical applications for quantum information technologies require strongly entangled qubits. Larger values for negativity, proper for practical devices,

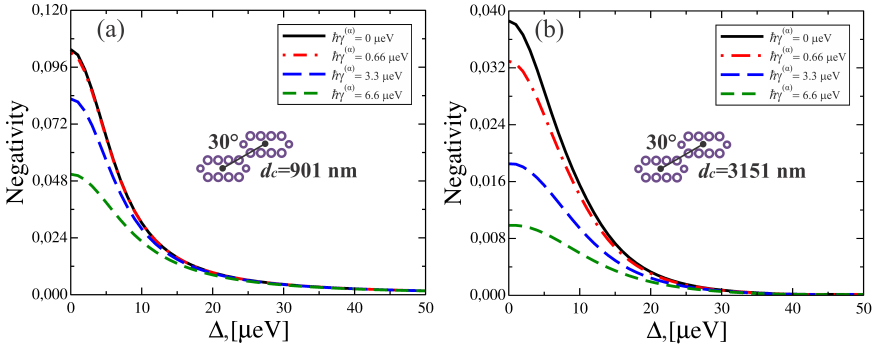

Figure 25: Steady state negativity for the 30° dimer at $d_c = 2\sqrt{3}a = 901$ nm, panel (a), and $d_c = 7\sqrt{3}a = 3151$ nm, panel (b), as a function of the detuning between the excitonic transition frequencies of the quantum dots, for different exciton loss rates. The dot 1 is in resonance with the lower frequency normal mode, i.e., $\omega^{(1)} = \omega_1$, and $\omega^{(2)} = \omega^{(1)} + \Delta$ with a pumping rate $\hbar\Omega_0 = 1$ μeV.

can be achieved in the transient dynamics of our system. We focus on the 30° dimer, which is the most convenient configuration for entanglement applications, and we consider the two quantum dots in resonance with the lower frequency normal mode, as well as $\hbar\Omega_0 = 1$ μeV at the optimal phase difference between the pumpings. The basis $|\alpha_1\alpha_2 m_1 m_2>$ for solving the dynamics of master equation Eq. (104), is safely truncated at $m_i = 1$. Figure 26 shows the negativity dynamics up to 6 ns at $d_c = 2\sqrt{3}a = 901$ nm and $\gamma^{(\alpha)} = 0$ for two different initial conditions: one excitation in dot 1, i.e., |1000>, and one photon in the lower frequency normal mode, i.e., |0010>. The negativity oscillates with a frequency determined by the pumping rate, $\sim \Omega_0/2$, and the amplitude of the oscillations approximates to the maximum negativity, i.e., 0.5, when the initial condition is at the photonic mode; which is the most favorable picture since the two quantum dots are equally populated in time by the field, giving rise to an optimal condition for maintaining the entanglement through the resonant-dot coherent pumping. When we consider an excited dot at $t = 0$, the two quantum dots are not equally populated in time leading to an unfavorable condition for increasing the entanglement between them. As it is physically expected, the amplitude of the oscillations decreases with increasing time, due to the normal mode dissipation, tending asymptotically to the steady state negativity.

Results of Fig. 26 show that the optimal initial condition is considering a populated photonic mode and unpopulated quantum dot at $t = 0$. Nevertheless, this is particularly challenging due to the delocalized nature of the normal mode; for achieving this initial condition it is necessary to prepare a collective state of both cavities at the same time. Here, we propose a different and less challenging

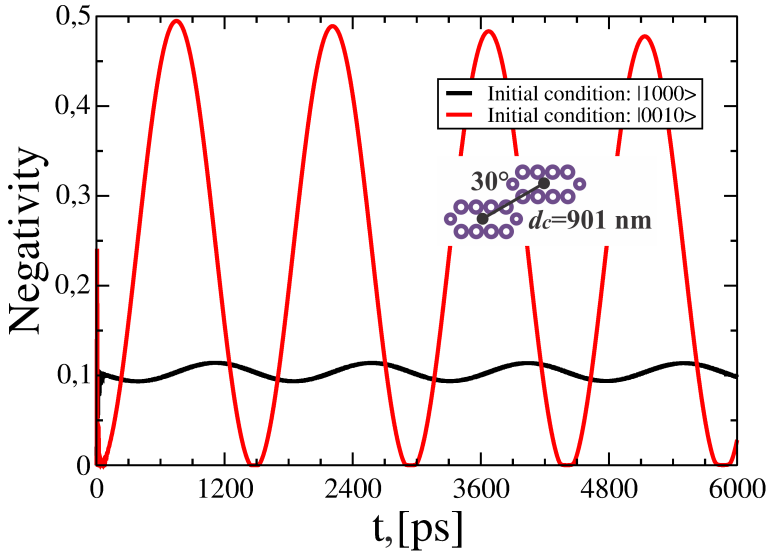

Figure 26: Negativity dynamics in the 30° dimer at $d_c = 2\sqrt{3}a = 901$ nm and $\gamma^{(\alpha)} = 0$, considering the initial conditions |1000>, in black, and |0010>, in red.

approach. Considering dot 2 out of resonance, and dot 1 in resonance with normal mode ω_1, we put the initial condition in dot 1, i.e., |1000>, and we wait for a time τ at which the normal mode 1 is maximally populated. At this time, we bring into the resonance dot 2 with dot 1, which can be accomplished, for example, using the quantum confined Stark effect [24, 90]. All the procedures are done pumping the dots with the frequency of the resonant dark state of the system. We show the results of this numerical experiment in Fig. 27 for the 30° dimer at $d_c = 2\sqrt{3}a = 901$ nm, panel (a), and $d_c = 5\sqrt{3}a = 2252$ nm, panel (b), where the same exciton loss rates of Figs. 23 and 25 were considered, and these intercavity distances delimit the flat region in Fig. 23(a). Panel (a) shows that our approach is totally equivalent to consider an initial excitation in the photonic mode, and the amount of entanglement is also near to the maximum in the transient dynamics for $\gamma^{(\alpha)} = 0$. As in Fig. 26, the amplitude of the oscillations decreases with increasing time due to the resonant normal mode dissipation. When exciton losses are taken into account, negativity values around ~ 0.2 are obtained for state-of-art quantum dots, however, the presence of this dissipation channel produces an amplitude decreasing which is faster than the corresponding decreasing for $\gamma^{(\alpha)} = 0$, and the steady state is achieved more rapidly. For $d_c = 2252$ nm, in panel (b), the presence of the second normal mode, with the same symmetry of the excitonic dark state, begins to be more relevant in the transient dynamics, providing an additional loss channel for the entangled dots; even for $\gamma^{(\alpha)} = 0$, the steady state regime is rapidly achieved, nevertheless, negativity

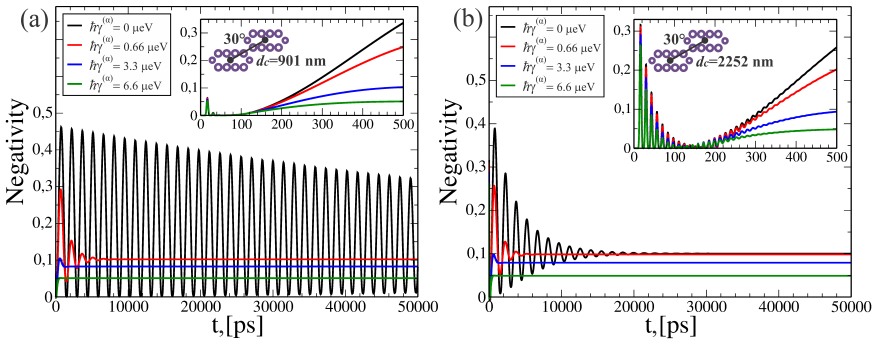

Figure 27: Numerical experiment for time dependent negativity in the transient dynamics using the 30° dimer at $d_c = 2\sqrt{3}a = 901$ nm, panel (a), and $d_c = 5\sqrt{3}a = 2252$ nm, panel (b). The initial condition is $|1000>$ in both cases with dot 1 and photonic mode ω_1 in resonance, and dot 2 far from resonance. We wait for a time $\tau = 9$ ps and $\tau = 9.3$ ps, at $d_c = 901$ nm and $d_c = 2252$ nm, respectively, with the aim of maximally populate the resonant photonic mode, and dot 2 is brought into resonance for $t > \tau$. The quantum dot pumping rate is $\hbar\Omega_0 = 1$ μeV at resonance with the excitonic dark state for all times. The insets show the early dynamics of the system.

values of about ~ 0.2 are still obtained for state-of-art quantum dots. In the early dynamics, show in insets of Fig. 27, the fast oscillation frequency is determined by the dot-field couplings g_m^n and the negativity amplitude by the loss rates; since the normal mode losses γ_m are smaller for $d_c = 2252$ nm than for $d_c = 901$ nm, the negativity amplitude is larger for $d_c = 2252$ nm than for $d_c = 901$ nm at this time regime. The transient slow-dynamics (after 200 ps), however, determines large-negativity time intervals which are much greater than the photonic mode and exciton lifetimes, allowing the possibility of practical entanglement applications.

4

CONCLUSIONS

We have studied the radiative coupling between two distant quantum dots embedded in two identical cavities of a photonic crystal molecule, or photonic crystal dimer, in a planar waveguide geometry by using a semiclassical formalism based on the Green's tensor. The photonic eigenmodes are found by guided mode expansion, which allows to estimate real and imaginary parts (losses) of the photonic eigenmodes, as well as the spatial mode profiles. Specifically, we have considered two L3 cavities made of three missing holes in a hexagonal lattice, in which field antinodes occur at each cavity center where the quantum dots can be placed. Moreover, we have addressed the possibility of entanglement between radiatively-coupled quantum dots using the normal modes of the photonic crystal dimer as quantum channels for long-range interaction. The amount of entanglement was quantified through the Peres-Horodecki negativity criterion of the dot-dot reduced density matrix, which is computed using the quantum-dissipative master equation. Parameters have been chosen to describe current systems typically fabricated with III-V semiconductors, such as InGaAs quantum dots in GaAs thin membranes.

Irrespective of the coupling angle between the two cavities (0°, 30°, 60°, 90°, respectively), we have shown that the effective interdot coupling is enhanced when the quantum dots are in resonance with either of the two normal modes of the photonic crystal dimer. Under such resonance conditions, and in the strong cavity-cavity coupling regime, the interdot coupling strength is actually proportional to the quality factors of the normal modes (bonding or antibonding), and it can be of the order of 1 meV for the cases considered in present study, which is at least an order of magnitude larger than typical values achieved in one-dimensional systems [26, 87]. Since these quality factors can also increase as a function of the inter-cavity distance, tending to the limiting value set by the isolated cavity mode (in the 10^5 range for the present case), then the radiative coupling can also increase with distance. Moreover, since the quality factors remain approximately constant at large distances, the radiative coupling can also remain constant at inter-dot separation that is significantly larger than their characteristic emission wavelength. Eventually, the mutual quantum dot coupling goes to zero when the normal mode splitting is blurred by their linewidth. We have also shown that our results on radiative coupling are robust against positioning disorder of the quantum dots considering the precision achieved by modern sample

fabrication techniques, and are also relatively robust against a structural disorder of the photonic crystal dimer of the same magnitude of the cavity-cavity coupling constant. Our calculations show that the effective energy transfer between the quantum dots is much more affected by the structural disorder than by the non-perfect positioning of the quantum dots. The degree of structural disorder which maintains almost unaltered the effective coupling strength between the dots is somewhat around five times smaller than what is presently achieved [95]. Nevertheless, for a structural disorder compatible with the state-of-art in GaAs or InGaAs structures the effective radiative dot-dot coupling is still an order of magnitude larger than previously studied disordered systems [29].

Into the quantum steady state regime and resonant condition, we have found that the largest entanglement between radiatively coupled quantum dots is obtained at the excitonic dark state of the system, pumping the dots with a phase difference of $(2n+1)\pi$, for bonding resonant normal modes, and of $2n\pi$ for antibonding resonant normal modes, where n is an integer number. The largest negativity value achieved in this regime is ~ 0.1, i.e., 20% of the maximum, and remains of the same order of magnitude as long as the normal mode splitting is well defined, i.e., much greater than the photonic linewidths. These results are shown to be robust against the main sources of quantum dot decoherence, such as spontaneous emission and pure dephasing. Furthermore, when the splitting is of the order of the photonic linewidths, the negativity is proportional to the normal mode splitting. On the other hand, where dot-dot detuning is considered in the system, the entanglement is sizable only for detunings which are smaller than the exciton linewidths; therefore, dot-dot radiative coupling, determined by the photonic linewidths, is a necessary but not a sufficient condition for entanglement between the quantum dots. We have also shown that when the figure of merit is long-range entanglement the 30° dimer is the most convenient configuration due to its very-well defined normal mode splitting, even at intercavity distances which are larger than the characteristic wavelength of the system. Our steady state results on entanglement showed to be robust for state-of-art InGaAs quantum dots. We have also studied the transient dynamics of the system with the aim of obtaining much more entangled qubits, with respect to the steady state regime, proper for applications in quantum information technologies. We found that an optimal condition for initializing the system is guaranteed by considering an initial excitation in the resonant normal mode, where long-time negativity oscillations with a frequency determined by the exciton pumping rate are seen with a period much larger than the photon and exciton lifetimes. Finally, based on these results, we proposed a different and totally equivalent approach for

generating the same long-time entanglement oscillations in practical devices, by initializing the system with an excitation in one of the quantum dots (less challenging task). Negativity values of the order of ~ 0.2, i.e. 40% of the maximum, were obtained for state-of-art InGaAs quantum dots in our proposed device.

We notice that the conclusions drawn in the present work can be extended to any type of photonic dimer, in principle. In fact, while the mentioned values of the radiative coupling strength and negativity are quantitatively valid for the specific systems considered here, it is still general the conclusion that the radiative coupling and entanglement between quantum dots in photonic dimers remains sizable even at significantly large inter-dot distances when two identical cavities are in the strong cavity-cavity coupling regime. Therefore, in view of the present conclusions, it is particularly relevant realizing photonic crystal dimers with normal mode splitting resolved even at very large distances for long-range quantum dot interactions.

Future developments of this work will be focused on the non-resonant energy transfer between the quantum dots in photonic crystal dimers. The present semiclassical formalism allows us to quantify the radiative coupling between the quantum dots at the same excitonic transition frequency; however, non-resonant radiative interactions through photonic modes whose linewidth is larger than the dot-dot detuning are not considered in the formulation. Since quantum dots are very likely to be detuned, the question of how the radiative coupling depends on the dot-dot detuning is quite relevant for practical applications. In the same direction, we have not quantified the effective photon-mediated interaction within the quantum mechanical formalism, in which energy detunings between the quantum dots can be naturally taken into account. Therefore, this will be also focus of future studies on photonic crystal chips with embedded quantum dots.

As a final remark, we believe that photonic molecules, as the ones studied in the present thesis, could be extremely promising in view of entangling distant qubits for applications in quantum information processing in integrated photonic circuits.

A

SUPERCELL METHOD

Defects on photonic crystals break the translation symmetry of the Bravais lattice, and the electromagnetic fields cannot adopt anymore the Bloch-Floquet form of Eq. (10). Nevertheless, it is possible to consider a cell with larger area containing the defect points with several periods of the defect-free Bravais lattice. Such a cell, which corresponds to a new Bravais lattice with larger period, is known as *supercell*, and allow us to write the electromagnetic fields in the Bloch-Floquet form. The supercell period must be chosen such that the coupling between defects from neighbor supercells be negligible. Figure 28 shows a schematic representation of a supercell in a square lattice of circular holes, where a missing hole at the center of the supercell represents the defect.

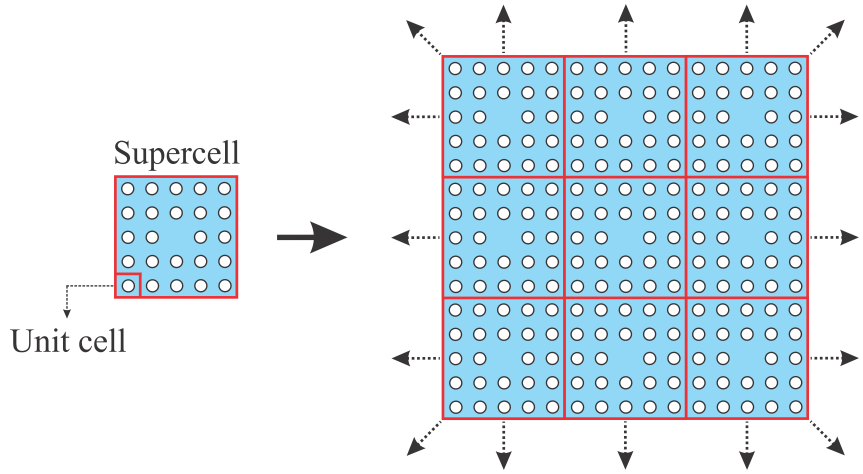

Figure 28: Schematic illustration of a supercell in a square lattice of circular holes. The defect is created by removing a hole in the center of the supercell.

The dielectric Fourier coefficients of a photonic crystal with defects can be calculated using Eq. (27) by considering the periodicity of the new Bravais lattice with the cell period given by the supercell. This Fourier integral is usually lengthy and tedious to calculate in a straightforward way, therefore, we present here two different approaches to easily compute such coefficients through simple superpositions.

Let us denote by $\epsilon_T(\mathbf{r}_{||})$, $\epsilon_b(\mathbf{r}_{||})$ and $\epsilon_{sh}^{(j)}(\mathbf{r}_{||} - \mathbf{r}_{||,j})$, the dielectric functions of the whole structure (with defect), regular structure (without

defect) and regular structure with the hole at position $\mathbf{r}_{||,j}$, respectively. Where $\mathbf{r}_{||}$ represents the in-plane coordinate vector of the periodic pattern. We then write

$$\epsilon_T(\mathbf{r}_{||}) = \epsilon_b(\mathbf{r}_{||}) + \sum_j \epsilon_{sh}^{(j)}(\mathbf{r}_{||} - \mathbf{r}_{||,j}), \tag{106}$$

where ϵ_b is equal to the dielectric constant of the slab outside the corresponding hole, i.e., ϵ_s, and is equal to the dielectric constant of the hole inside the corresponding hole, i.e., ϵ_h. Moreover, ϵ_{sh}, inside the corresponding hole, is equal to $\epsilon_s - \epsilon_h$ for removing holes and equal to $\epsilon_h - \epsilon_s$ for creating holes, and is always equal to 0 outside the corresponding hole. Notice that Eq. (106) gives the dielectric function of the crystal with defects as a superposition of the regular or background crystal (without defects) and separated defects, either to fill or to create holes. The following periodicity conditions must be fulfilled by the dielectric functions:

$$\begin{aligned}
\epsilon_T(\mathbf{r}_{||}) &= \epsilon_T(\mathbf{r}_{||} + \mathbf{R}_S) \\
\epsilon_b(\mathbf{r}_{||}) &= \epsilon_b(\mathbf{r}_{||} + \mathbf{R}_S) = \epsilon_b(\mathbf{r}_{||} + \mathbf{R}) \\
\epsilon_{sh}^{(j)}(\mathbf{r}_{||}) &= \epsilon_{sh}^{(j)}(\mathbf{r}_{||} + \mathbf{R}_S),
\end{aligned} \tag{107}$$

where $\mathbf{R}_S$ and $\mathbf{R}$ denote the lattice vector of the crystal with supercell and the regular crystal (without supercell), respectively. The dielectric functions are now expanded in a set of plane waves with the periodicity of the corresponding reciprocal lattice

$$\sum_{\mathbf{G}_S} \epsilon_T(\mathbf{G}_S) e^{-i\mathbf{G}_S\cdot\mathbf{r}_{||}} = \sum_{\mathbf{G}} \epsilon_b(\mathbf{G}) e^{-i\mathbf{G}\cdot\mathbf{r}_{||}} + \sum_{j,\mathbf{G}_S} \epsilon_d(\mathbf{G}_S) e^{-i\mathbf{G}_S\cdot\mathbf{r}_{||}} e^{i\mathbf{G}_S\cdot\mathbf{r}_{||,j}}, \tag{108}$$

where $\mathbf{G}_S$ and $\mathbf{G}$ denote the reciprocal lattice vectors of the crystal with supercell and the regular crystal (without supercell), respectively. By multiplying Eq. (108) by $e^{-i\mathbf{G}'_S\cdot\mathbf{r}_{||}}$ and integrating over the supercell area, we obtain the following expression for the Fourier coefficients of $\epsilon_T(\mathbf{r}_{||})$:

$$\epsilon_T(\mathbf{G}_S) = \delta_{\mathbf{G},\mathbf{G}_S}\epsilon_b(\mathbf{G}) + \sum_j \epsilon_d(\mathbf{G}_S) e^{i\mathbf{G}_S\cdot\mathbf{r}_{||,j}}. \tag{109}$$

The condition $\delta_{\mathbf{G},\mathbf{G}_S}$ in Eq. (109) means that only the coefficients $\epsilon_b(\mathbf{G})$ with $\mathbf{G} = \mathbf{G}_S$ contribute to $\epsilon_T(\mathbf{G}_S)$, which implies that the ratio between the area of the supercell and the area of the regular unit cell must be an integer number. Taking into account that $\epsilon_b(\mathbf{G})$ and $\epsilon_d(\mathbf{G}_S)$ functions have the same mathematical form, and the differences between them are the period and the values of the dielectric constants inside and outside the holes, the coefficient $\epsilon_T(\mathbf{G}_S)$ is totally determined by the Fourier coefficient of the regular unit cell.

Therefore, the calculation of the integral in Eq. (27) over the all holes in the supercell, is reduced in Eq. (109) to the calculation of the integral over a single hole.

Equation (109) is very useful where the defects are created by a small quantity of missing or modified holes in the photonic crystal. However, for disorder calculations in which all the holes are modified, such a method is not efficient because we would need to remove all the holes, and then, create them again with different radii. A better approach consists in directly creating the desired holes in a homogeneous background dielectric medium. Thus, we write the dielectric function of the whole structure in the form

$$\epsilon_T(\mathbf{r}_{||}) = \epsilon_s + \sum_j \epsilon_{hs}^{(j)}(\mathbf{r}_{||} - \mathbf{r}_{||,j}), \tag{110}$$

where ϵ_s denotes dielectric constant of the background slab dielectric medium, and ϵ_{hs} is equal to $\epsilon_h - \epsilon_s$ and 0, inside and outside the corresponding hole, respectively. By applying the same procedures to obtain Eq. (109) from Eq. (106), we get the following expression for the Fourier coefficients of $\epsilon_T(\mathbf{r}_{||})$:

$$\epsilon_T(\mathbf{G}_S) = \delta_{G_S,0}\epsilon_s + \sum_j \epsilon_d(\mathbf{G}_S)e^{iG_S\cdot\mathbf{r}_{||,j}}. \tag{111}$$

where j runs over the all holes inside the supercell. In the present work, we employed Eq. (109) for calculating the Fourier coefficients of the dimers without disorder, and Eq. (111) was employed for disorder calculations.

The supercell method is a good approximation for studying defects when the size of the supercell is large enough to consider as negligible the coupling between defects from neighbor supercells. However, this coupling is not zero and it is always present on the defect bands, originating numerical dispersions in the group velocity of the mode. For example, point defects, which should have zero group velocity, appears in the band diagram with small curvatures giving rise to a non-zero group velocity along the irreducible Brillouin zone. This numerical artifact becomes more problematic for small supercells in comparison with the characteristic exponential decay-length of the field outside the defect region. The criterion to choose the supercell dimensions is then given by the flatness of the defect bands whose group velocity should be null: the defect band must be flat in comparison to the band edges defining the band gap of the photonic crystal. In addition to this, for photonic crystal molecules, the normal mode bands must be also flat in comparison with themselves. Since the numerical dispersion is always present even for large supercells, we take the average of the band over the irreducible Brillouin zone,

and we consider such average as the quantity with physical meaning in the calculation. This averaging procedure has shown to be in good agreement with "exact" calculations in finite systems given by finite-difference time-domain (FDTD) methods [48].

BIBLIOGRAPHY

[1] E. Yablonovitch, "Inhibited Spontaneous Emission in Solid-State Physics and Electronics," *Physical Review Letters*, vol. 58, pp. 2059–2062, 1987.

[2] S. John, "Strong localization of photons in certain disordered dielectric superlattices," *Physical Review Letters*, no. 58, pp. 2486–2489, 1987.

[3] K. Sakoda, *Optical Properties of Photonic Crystals*. Springer, second ed., 2004.

[4] Y. Lai, S. Pirotta, G. Urbinati, D. Gerace, M. Minkov, V. Savona, A. Badolato, and M. Galli, "Genetically designed L3 photonic crystal nanocavities with measured quality factor exceeding one million," *Applied Physics Letters*, vol. 104, p. 241101, 2014.

[5] J. Y. Lee, X. Lu, and Q. Lin, "High-Q silicon carbide photonic-crystal cavities," *Applied Physics Letters*, vol. 106, p. 041106, 2015.

[6] D. Loss and D. P. DiVincenzo, "Quantum computation with quantum dots," *Physical Review A*, vol. 57, p. 120, 1998.

[7] Imamog¯lu, D. D. Awschalom, G. Burkard, D. P. DiVincenzo, D. Loss, M. Sherwin, and A. Small, "Quantum Information Processing Using Quantum Dot Spins and Cavity QED," *Physical Review Letters*, vol. 83, p. 4204, 1999.

[8] R. J. Warburton, "Self-assembled semiconductor quantum dots," *Contemporary Physics*, vol. 43, p. 351, 2002.

[9] R. J. Warburton, "Single spins in self-assembled quantum dots," *Nature Materials*, vol. 12, p. 483, 2013.

[10] J. Vuckovic and Y. Yamamoto, "Photonic crystal microcavities for cavity quantum electrodynamics with a single quantum dot," *Applied Physics Letters*, vol. 82, p. 2374, 2003.

[11] A. Badolato, K. Hennessy, M. Atatüre, J. Dreiser, E. Hu, P. M. Petroff, and A. Imamoglu, "Deterministic Coupling of Single Quantum Dots to Single Nanocavity Modes," *Science*, vol. 308, p. 1158, 2005.

[12] P. Lodahl, S. Mahmoodian, and S. Stobbe, "Interfacing single photons and single quantum dots with photonic nanostructures ," *Reviews of Modern Physics*, vol. 87, p. 347, 2015.

[13] L. Jeremy, O'Brien, A. Furusawa, and J. Vuckovic, "Photonic quantum technologies," *Nature Photonics*, vol. 31, p. 687, 2009.

[14] W.-H. Chang, W.-Y. Chen, H.-S. Chang, T.-P. Hsieh, J.-I. Chyi, and T.-M. Hsu, "Efficient Single-Photon Sources Based on Low-Density Quantum Dots in Photonic-Crystal Nanocavities," *Physical Review Letters*, vol. 96, p. 117401, 2006.

[15] B. Ellis, M. A. Mayer, G. Shambat, T. Sarmiento, J. Harris, E. E. Haller, and J. Vuckovic, "Ultralow-threshold electrically pumped quantum-dot photonic-crystal nanocavity laser," *Nature Photonics*, vol. 528, p. 297, 2011.

[16] T. Yoshie, A. Scherer, J. Hendrickson, G. Khitrova, H. M. Gibbs, G. Rupper, C. Ell, O. B. Shchekin, and D. G. Deppe, "Vacuum Rabi splitting with a single quantum dot in a photonic crystal nanocavity," *Nature*, vol. 432, p. 200, 2004.

[17] K. Hennessy, A. Badolato, M. Winger, D. Gerace, M. Atatüre, S. Gulde, S. Fält, E. L. Hu, and A. Imamoglu, "Quantum nature of a strongly coupled single quantum dot–cavity system," *Nature*, vol. 445, p. 896, 2007.

[18] P. Lodahl, A. F. van Driel, I. S. Nikolaev, A. Irman, K. Overgaag, D. Vanmaekelbergh, and W. L. Vos, "Controlling the dynamics of spontaneous emission from quantum dots by photonic crystals," *Nature*, vol. 430, p. 654, 2004.

[19] S. Noda, M. Fujita, and T. Asano, "Spontaneous-emission control by photonic crystals and nanocavities," *Nature Photonics*, vol. 1, p. 449, 2007.

[20] K. J. Vahala, "Optical microcavities," *Nature*, vol. 424, p. 839, 2003.

[21] J. D. Joannopoulos, S. G. Johnson, and J. N. Winn, *Photonic Crystals: Molding the Flow of Light*. Princeton University Press, second ed., 2008.

[22] Michael A. Nielsen and Isaac L. Chuang, *Quantum Computation and Quantum Information*. Cambridge Series on Information and the Natural Sciences, first ed., 2004.

[23] A. Nazir, B. W. Lovett, S. D. Barrett, J. H. Reina, and G. A. D. Briggs, "Anticrossings in Förster coupled quantum dots," *Physical Review B*, vol. 71, p. 045334, 2005.

[24] A. Laucht, J.M. Villas-Bôas, S. Stobbe, N. Hauke, F. Hofbauer, G. Böhm, P. Lodahl, M.-C. Amann, M. Kaniber, and J.J. Finley, "Mutual coupling of two semiconductor quantum dots via an optical nanocavity," *Physical Review B*, vol. 82, p. 075305, 2010.

[25] Philip Trost Kristensen, Jesper Mork, Peter Lodahl, and Stephen Hughes, "Decay dynamics of radiatively coupled quantum dots in photonic crystal slabs ," *Physical Review B*, vol. 83, p. 075305, 2011.

[26] Momchil Minkov and Vincenzo Savona, "Radiative coupling of quantum dots in photonic crystal structures ," *Physical Review B*, vol. 87, p. 125306, 2013.

[27] S. Hughes, "Coupled-Cavity QED Using Planar Photonic Crystals," *Physical Review Letters*, vol. 98, p. 083603, 2007.

[28] P. Yao and S. Hughes, "Macroscopic entanglement and violation of Bell's inequalities between two spatially separated quantum dots in a planar photonic crystal system," *Optics Express*, vol. 17, p. 11505, 2009.

[29] Momchil Minkov and Vincenzo Savona, "Long-distance radiative excitation transfer between quantum dots in disordered photonic crystal waveguides," *Physical Review B*, vol. 88, p. 081303(R), 2013.

[30] A. Imamoglu, S. Falt, J. Dreiser, G. Fernandez, M. Atature, K. Hennessy, A. Badolato, and D. Gerace, "Coupling quantum dot spins to a photonic crystal nanocavity," *Journal of Applied Physics*, vol. 101, p. 081602, 2007.

[31] E. Gallardo, L. Martinez, A. Nowak, D. Sarkar, H. van de Meulen, J. Calleja, C. Tejedor, I. Prieto, D. Granados, A. Taboada, J. Garcia, and P. Postigo, "Optical coupling of two distant InAs/GaAs quantum dots by a photonic-crystal microcavity," *Physical Review B*, vol. 81, p. 193301, 2010.

[32] M. Benyoucef, S. Kiravittaya, Y. F. Mei, A. Rastelli, and O. G. Schmidt, "Strongly coupled semiconductor microcavities: A route to couple artificial atoms over micrometric distances," *Physical Review B*, vol. 77, p. 035108, 2008.

[33] J. P. Vasco, P. S. S. Guimarães, and D. Gerace, "Long-distance radiative coupling between quantum dots in photonic crystal dimers," *Physical Review B*, vol. 90, p. 155436, 2014.

[34] A.R.A. Chalcraft, S. Lam, B.D. Jones, D. Szymanski, R. Oulton, A.C.T. Thijssen, M.S. Skolnick, D.M. Whittaker, T.F. Krauss, and A.M. Fox, "Mode structure of coupled L3 photonic crystal cavities," *Optics Express*, vol. 19, p. 5670, 2011.

[35] Y. Sato, Y. Tanaka, J. Upham, Y. Takahashi, T. Asano, and S. Noda, "Strong coupling between distant photonic nanocavities and its dynamic control," *Nature Photonics*, vol. 6, p. 5670, 2012.

[36] J. D. Jackson, *Classical Electrodynamics*. Wiley, third ed., 1998.

[37] J. Sakurai, *Modern Quantum Mechanics*. Addison Wesley, revised ed., 1993.

[38] N. W. Ashcroft and N. D. Mermin, *Solid State Physics*. Brooks Cole, first ed., 1976.

[39] T. Baba, "Slow light in photonic crystals," *Nature Photonics*, vol. 2, p. 465, 2008.

[40] "Proceedings of the American Physical Society," *Physical Review*, vol. 69, p. 674, 1946.

[41] N. Caselli, F. Intonti, F. Riboli, A. Vinattieri, D. Gerace, L. Balet, L. Li, M. Francardi, A. Gerardino, A. Fiore, and M. Gurioli, "Antibonding ground state in photonic crystal molecules," *Physical Review B*, vol. 86, p. 035133, 2012.

[42] K. M. Ho, C. T. Chan, and C. M. Soukoulis, "Existence of a Photonic Gap in Periodic Dielectric Structures," *Physical Review Letters*, vol. 65, p. 3152, 1990.

[43] E. Yablonovitch, "Photonic band-gap structures," *Journal of the Optical Society of America B*, vol. 10, p. 283, 1993.

[44] S. Takahashi, K. Suzuki, M. Okano, M. Imada, T. Nakamori, Y. Ota, K. Ishizaki, and S. Noda, "Direct creation of three-dimensional photonic crystals by a top-down approach," *Nature Materials*, vol. 8, p. 721, 2009.

[45] E. C. Nelson, N. L. Dias, K. P. Bassett, S. N. Dunham, V. Verma, M. Miyake, P. Wiltzius, J. A. Rogers, J. J. Coleman, X. Li, and P. V. Braun, "Epitaxial growth of three-dimensionally architectured optoelectronic devices," *Nature Materials*, vol. 10, p. 676, 2011.

[46] K. Ishizaki, M. Koumura, K. Suzuki, K. Gondaira, and S. Noda, "Realization of three-dimensional guiding of photons in photonic crystals," *Nature Photonics*, vol. 7, p. 133, 2013.

[47] E. Chow, S. Lin, S. Johnson, P. Villeneuve, J. Joannopoulos, J. Wendt, G. Vawter, W. Zubrzycki, H. Hou, and A. Alleman, "Three-dimensional control of light in a two-dimensional photonic crystal slab," *Nature Materials*, vol. 407, p. 983, 2000.

[48] L. C. Andreani and D. Gerace, "Photonic-crystal slabs with a triangular lattice of triangular holes investigated using a guided-mode expansion method," *Physical Review B*, vol. 73, p. 235114, 2006.

[49] J. Caro, E. M. Roeling, B. Rong, H. M. Nguyen, E. W. J. M. van der Drift, S. Rogge, F. Karouta, R. W. van der Heijden, and H. W. M. Salemink, "Transmission measurement of the photonic band gap of GaN photonic crystal slabs ," *Applied Physics Letters*, vol. 93, p. 051117, 2008.

[50] B. K. Ofori-Okai, P. Sivarajah, C. A. Werley, S. M. Teo, and K. A. Nelson, "Direct experimental visualization of waves and band structure in 2D photonic crystal slabs ," *New Journal of Physics*, vol. 16, p. 053003, 2014.

[51] P. T. Valentim, J. P. Vasco, I. J. Luxmoore, D. Szymanski, H. Vinck-Posada, A. M. Fox, D. M. Whittaker, M. S. Skolnick, and P. S. S. Guimarães, "Asymmetry tuning of Fano resonances in GaAs photonic crystal cavities," *Applied Physics Letters*, vol. 102, p. 111112, 2013.

[52] J. P. Vasco, H. Vinck-Posada, P. T. Valentim, and P. S. S. Guimãraes, "Modeling of Fano resonances in the reflectivity of photonic crystal cavities with finite spot size excitation ," *Optics Express*, vol. 21, p. 31336, 2013.

[53] S. Shi, C. Chen, and D. W. Prather, "Plane-wave expansion method for calculating band structure of photonic crystal slabs with perfectly matched layers ," *Journal of the Optical Society of America A*, vol. 21, p. 1769, 2004.

[54] D. M. Whittaker and I. S. Culshaw, "Scattering-matrix treatment of patterned multilayer photonic structures," *Physical Review B*, vol. 60, p. 2610, 1999.

[55] S. Fan and J. D. Joannopoulos, "Analysis of guided resonances in photonic crystal slabs," *Physical Review B*, vol. 65, p. 235112, 2002.

[56] A. Taflove and S. C. Hagness, *Computational Electrodynamics: The Finite-Difference Time-Domain Method*. Artech House Antennas and Propagation Library, Artech House, third ed., 2005.

[57] D. Gerace, *Photonic modes and radiation-matter interaction in photonic crystal slabs*. PhD thesis, 2005.

[58] L. Li, "Use of Fourier series in the analysis of discontinuous periodic structures ," *Journal of the Optical Society of America A*, vol. 13, p. 1870, 1996.

[59] T. Ochiai and K. Sakoda, "Nearly free-photon approximation for two-dimensional photonic crystal slabs," *Physical Review B*, vol. 64, p. 045108, 2001.

[60] J. P. Reithmaier, "Nanostructured Semiconductor Materials For Optoelectronic Applications," in *Nanostructured Materials for Advanced Technological Applications*, ch. 6.3, pp. 447–476, Springer Netherlands, 2009.

[61] P. Harrison, *Quantum Wells, Wires and Dots*. John Wiley & Sons, 2 ed., 2005.

[62] F. Albert, K. Sivalertporn, J. Kasprzak, M. Strauß, C. Schneider, S. Höfling, M. Kamp, A. Forchel, S. Reitzenstein, E. Muljarov, and W. Langbein, "Microcavity controlled coupling of excitonic qubits," *Nature Communications*, vol. 4, p. 1747, 2013.

[63] F. Tassone, F. Bassani, and L. C. Andreani, "Quantum-well reflectivity and exciton-polariton dispersion," *Physical Review B*, vol. 45, no. 11, p. 6023, 1992.

[64] M. Kira and S. W. Koch, *Semiconductor Quantum Optics*. Cambridge University Press, first ed., 2012.

[65] J. Hopfield, "Theory of the contribution of excitons to the complex dielectric constant of crystals," *Physical Review*, vol. 112, p. 1555, 1958.

[66] A. Kavokin, J. J. Baumberg, G. Malpuech, and F. P. Laussy, *Microcavities*. Series on Semiconductor Science and Technology, Oxford University Press, 2006.

[67] G. Parascandolo and V. Savona, "Long-range radiative interaction between semiconductor quantum dots," *Physical Review B*, vol. 71, p. 045335, 2005.

[68] D. Walls and G. J. Milburn, *Quantum Optics*. Springer-Verlag Berlin Heidelberg, second ed., 2008.

[69] P. Meystre and M. Sargent, *Elements of Quantum Optics*. Springer-Verlag Berlin Heidelberg, fourth ed., 2007.

[70] B. J. Dalton, E. S. Guerra, and P. L. Knight, "Field quantization in dielectric media and the generalized multipolar Hamiltonian," *Physical Review A*, vol. 54, p. 2292, 1996.

[71] M. Wubs, L. G. Suttorp, and A. Lagendijk, "Multipole interaction between atoms and their photonic environment," *Physical Review A*, vol. 68, p. 013822, 2003.

[72] L. Amico, R. Fazio, A. Osterloh, and V. Vedral, "Entanglement in many-body systems," *Reviews of Modern Physics*, vol. 80, p. 517, 2008.

[73] R. Islam, R. Ma, P. M. Preiss, M. E. Tai, A. Lukin, M. Rispoli, and M. Greiner, "Measuring entanglement entropy in a quantum many-body system," *Nature*, vol. 528, p. 77, 2015.

[74] P. Hauke, M. Heyl, L. Tagliacozzo, and P. Zoller, "Measuring multipartite entanglement through dynamic susceptibilities," *Nature Physics*, vol. advance online publication, 2016.

[75] G.-x. Li, H.-t. Tan, S.-p. Wu, and Y.-p. Yang, "Entanglement for excitons in two quantum dots placed in two separate single-mode cavities," *Physical Review A*, vol. 70, p. 034307, 2004.

[76] E. del Valle, F. P. Laussy, F. Troiani, and C. Tejedor, "Entanglement and lasing with two quantum dots in a microcavity," *Physical Review B*, vol. 76, p. 235317, 2007.

[77] J. Liu, Z.-T. Jiang, and B. Shao, "Local measurement of the entanglement between two quantum-dot qubits," *Physical Review B*, vol. 79, p. 115323, 2009.

[78] D. Kim, S. G. Carter, A. Greilich, A. S. Bracker, and D. Gammon, "Ultrafast optical control of entanglement between two quantum-dot spins," *Nature Physics*, vol. 7, p. 223, 2011.

[79] M. Horodecki, P. Horodecki, and R. Horodecki, "Separability of mixed states: necessary and sufficient conditions," *Physics Letters A*, vol. 223, p. 111112, 1996.

[80] A. Peres, "Separability Criterion for Density Matrices," *Physical Review Letters*, vol. 77, p. 1413, 1996.

[81] S. J. Akhtarshenas and M. Farsi, "Negativity as entanglement degree of the Jaynes–Cummings model," *Physica Scripta*, vol. 75, p. 608, 2007.

[82] M. Benyoucef, S. Kiravittaya, Y. Mei, A. Rastelli, and O. Schmidt, "Strongly coupled semiconductor microcavities: A route to couple artificial atoms over micrometric distances," *Physical Review B*, vol. 77, p. 035108, 2008.

[83] Yoshihiro Akahane, Takashi Asano, Bong-Shik Song, and Susumu Noda, "High-Q photonic nanocavity in a two-dimensional photonic crystal," *Nature*, vol. 425, pp. 944–947, 2003.

[84] A. Chalcraft, S. Lam, D. O'Brien, T. Krauss, M. Sahin, D. Szymanski, D. Sanvitto, R. Oulton, M. Skolnick, A. Fox, D. Whittaker, H. Liu, and M. Hopkinson, "Mode structure of the L3 photonic crystal cavity," *Applied Physics Letters*, vol. 90, no. 241117, 2007.

[85] Lucio Claudio Andreani, Dario Gerace, and Mario Agio, "Gap maps, diffraction losses, and exciton–polaritons in photonic crystal slabs," *Photonics and Nanostructures - Fundamentals and Applications*, vol. 2, p. 103, 2004.

[86] Svetlana V. Boriskina, "Theoretical prediction of a dramatic Q-factor enhancement and degeneracy removal of whispering gallery modes in symmetrical photonic molecules," *Optics Letters*, vol. 31, p. 338, 2006.

[87] G. Tarel, G. Parascandolo, and V. Savona, "Ultralong-range radiative excitation transfer between quantum dots in a planar microcavity," *Physica Status Solidi b*, vol. 245, p. 1085, 2008.

[88] A. Reinhard, T. Volz, M. Winger, A. Badolato, K. J. Hennessy, E. L. Hu, and A. Imamoglu, "Strongly correlated photons on a chip," *Nature Photonics*, vol. 6, p. 93, 2012.

[89] A. Majumdar, A. Rundquist, M. Bajcsy, V. D. Dasika, S. R. Bank, and J. Vuckovic, "Design and analysis of photonic crystal coupled cavity arrays for quantum simulation," *Physical Review B*, vol. 86, no. 195312, 2012.

[90] A. Faraon, A. Majumdar, H. Kim, P. Petroff, and J. Vuckovic, "Fast Electrical Control of a Quantum Dot Strongly Coupled to a Photonic-Crystal Cavity," *Physical Review Letters*, vol. 104, p. 047402, 2010.

[91] A. Majumdar, M. Bajcsy, A. Rundquist, E. Kim, and J. Vuckovic, "Phonon-mediated coupling between quantum dots through an off-resonant microcavity," *Physical Review B*, vol. 85, p. 195301, 2012.

[92] SomaschiN., GieszV., D. SantisL., L. C., A. P., HorneckerG., P. L., GrangeT., AntónC., DemoryJ., GómezC., SagnesI., L.-K. D., LemaítreA., AuffevesA., W. G., LancoL., and SenellartP., "Near-optimal single-photon sources in the solid state," *Nature Photonics*, vol. advance online publication, 2016.

[93] S. Weiler, A. Ulhaq, S. M. Ulrich, D. Richter, M. Jetter, P. Michler, C. Roy, and S. Hughes, "Phonon-assisted incoherent excitation of a quantum dot and its emission properties," *Physical Review B*, vol. 86, p. 241304(R), 2012.

[94] G. Angelatos and S. Hughes, "Entanglement dynamics and Mollow nonuplets between two coupled quantum dots in a nanowire photonic-crystal system," *Physical Review A*, vol. 91, p. 051803(R), 2015.

[95] P. Garcia, A. Javadi, H. Thyrrestrup, and P. Lodahl, "Quantifying the intrinsic amount of fabrication disorder in photonic-crystal

waveguides from optical far-field intensity measurements," *Applied Physics Letters*, vol. 102, p. 031101, 2013.

COLOPHON

This document was typeset using the typographical look-and-feel `classicthesis` developed by André Miede. The style was inspired by Robert Bringhurst's seminal book on typography "*The Elements of Typographic Style*". `classicthesis` is available for both LaTeX and LyX:

http://code.google.com/p/classicthesis/